technische universität
dortmund

Dissertation
zur Erlangung des akademischen Grades
Doktor der Naturwissenschaften

Beam Test Studies of ATLAS ITk Pixel Detector Modules

Christopher Krause
geboren in Mainz

2025

AG Kröninger
Fakultät Physik
Technische Universität Dortmund

Erstgutachter: Prof. Dr. Kevin Kröninger
Zweitgutachter: Dr. Dominik Mitzel
Vorsitz der Prüfungskommission: Prof. Dr. Mirko Cinchetti
Kommissionsmitglied: Apl. Prof. Dr. Doris Reiter

Datum des Einreichens der Arbeit: 22.04.2025
Datum der mündlichen Prüfung: 17.07.2025

Dissertation zur Erlangung des akademischen Grades Doktor der Naturwissenschaften (Doctor rerum naturalium), angenommen von der Fakultät Physik der Technischen Universität Dortmund.

Abstract

The ATLAS ITk will replace the Inner Detector of the ATLAS experiment for the High-Luminosity phase of the LHC. To ensure an excellent tracking performance of the silicon pixel sensors of the ITk under the harsher environment, their performance has to be thoroughly tested and validated in laboratories and beam test facilities before installation. Electrical properties of several HPK and Micron Test structures from pre-production sensors were investigated in the scope of this thesis. Bonded pre-production modules from HPK and Micron using the ITkPixV1.1 and ITkPixV2 were investigated in CERN SPS beam tests. The performance of unirradiated and irradiated planar quad modules in beam tests from 2022 to 2024 has been analysed. All investigated test structures and pre-production modules satisfy the ITk requirements.

A beam test measurement was conducted for the investigation of the in-time efficiency of an ITkPixV1.1 readout chip. The front-end clock was probed with a time resolution of 780 ps, although the sub-optimal time resolution of the utilised scintillators only allowed for a timing precision of 2-3 ns. While no front-end clock effects were detected at this time resolution, the measurement principle proved to be successful and paves the way for an investigation of the final design readout chip with an improved time resolution and charge information.

Additionally, beam test simulations using high-intensity beams are investigated regarding the feasible track reconstruction using one-dimensional feature cuts and a machine learning approach. Due to the high energies of the particles, proper track reconstruction was achieved with all approaches, with the implemented classifier only performing slightly better.

Kurzfassung

Der ATLAS ITk wird den Inneren Detektor des ATLAS-Experiments für die Hochluminositätsphase des LHC ersetzen. Um eine exzellente Spurrekonstruktion der Siliziumpixelsensoren des ITk unter den verschärften Strahlungsbedingungen sicherzustellen, muss ihre Leistung vor der Installation in Laboren und Teststrahlanlagen umfassend geprüft und validiert werden. Im Rahmen dieser Arbeit wurden die elektrischen Eigenschaften mehrerer Teststrukturen von HPK und Micron aus der Vorproduktion untersucht. Zudem wurden gebondete Vorproduktionsmodule von HPK und Micron mit den ITkPixV1.1 und ITkPixV2 Auslesechips in Strahltests am CERN SPS vermessen. Die Leistung unbestrahlter und bestrahlter planarer Quad-Module in Strahltests der Jahre 2022 bis 2024 wurde analysiert. Alle untersuchten Teststrukturen und Vorproduktionsmodule erfüllen die Anforderungen für den ITk.

Eine Strahltestmessung wurde zur Untersuchung der In-Time-Effizienz eines ITkPixV1.1 Auslesechips durchgeführt. Die Taktrate des Auslesechips wurde mit einer Zeitauflösung von 780 ps untersucht, wobei die suboptimale Zeitauflösung der verwendeten Szintillatoren lediglich eine Zeitpräzision von 2–3 ns zuließ. Für diese Zeitauflösung wurden keine Takteffekte des Auslesechips nachgewiesen, jedoch erwies sich das Messprinzip als erfolgreich und ermöglicht eine Untersuchung des finalen Auslesechips mit verbesserter Zeitauflösung und Ladungsinformation.

Zusätzlich wurden Strahltestsimulationen mit hochintensiven Teilchenstrahlen hinsichtlich der realisierbaren Spurrekonstruktion unter Verwendung eindimensionaler Merkmalsselektionen und maschineller Lernverfahren untersucht. Aufgrund der hohen Teilchenenergien konnte in allen Ansätzen eine zuverlässige Spurrekonstruktion erreicht werden, wobei die Merkmalsselektion des Klassifizierers nur geringfügig besser ist.

Contents

List of Abbreviations

AUC Area Under The Curve

BDT Boosted Decision Tree

CART Classification And Regression Tree

CERN European Organization for Nuclear Research

CV Capacitance-Voltage

DAQ Data Acquisition

DUT Device Under Test

EHN1 Experimental Hall North 1

F Score Feature Importance Score

FBK Fondazione Bruno Kessler

FE Front-End

FPR False Positive Rate

FWHM Full Width Half Maximum

GBL General Broken Lines

HL-LHC High Luminosity Large Hadron Collider

HPK Hamamatsu Photonics

IBL Insertable B-Layer

ID Inner Detector

It Current-Time

ITk Inner Tracker

IV Current-Voltage

LHC Large Hadron Collider

LS Long Strip

MIP Minimum Ionising Particle

ndof Number Of Degrees Of Freedom

PD Pixel Detector

PDF Probability Density Functions

PS Proton Synchrotron

QA Quality Assurance

ROC Receiver Operating Characteristic

SCC Single Chip Card

SCT Semiconductor Tracker

SPS Super Proton Synchrotron

SS Short Strip

TID Trigger Identifier

TLU Trigger Logic Unit

TOT Time Over Threshold

TPR True Positive Rate

TRT Transition Radiation Tracker

TS Test Structure(s)

1 Introduction

Understanding the fundamental nature of the universe requires the continuous development and refinement of particle physics theories. These theories are rigorously tested using experimental data to improve their explanatory power. To achieve this, numerous particle physics experiments have been designed and built to collect the necessary data. Among the most crucial of these experiments are particle accelerators, such as the Large Hadron Collider at CERN. By colliding particles at extremely high energies, accelerators facilitate the study of fundamental interactions and enable the production of various particles, including the heaviest known ones, such as the top quark and the Higgs boson. Since these particles are often short-lived, their properties must be inferred from their decay products. To achieve this, highly specialised detectors measure key quantities of the high-energy particles produced in collisions. Given the vast range of particle interactions, multiple sub-detectors must be incorporated into a single large-scale detector experiment to ensure the comprehensive measurement of essential particle properties such as energy, momentum, charge and trajectory.

One of the major detectors at the Large Hadron Collider is the ATLAS experiment, located at one of the four interaction points of the collider. As a general-purpose detector, it is designed to explore a wide range of particle physics phenomena. A critical component of the ATLAS experiment is its tracking system, which reconstructs the trajectories of charged particles with high precision. To achieve this, silicon pixel detectors are employed in the innermost layers of the detector, positioned close to the interaction point. These detectors are designed to measure particle signals with high precision while enduring significant radiation exposure over many years of operation. To enhance the study of rare processes at the Large Hadron Collider, a High-Luminosity phase is planned to commence after the Long Shutdown 3 in 2030. Over 12 years, the High-Luminosity Large Hadron Collider is expected to deliver a total integrated luminosity of approximately $4000\,\mathrm{fb}^{-1}$ with an instantaneous luminosity of up to $7.5 \cdot 10^{34}\,\mathrm{cm}^{-2}\mathrm{s}^{-1}$. Consequently, the expected particle fluxes increase with the instantaneous luminosity, posing new challenges for silicon pixel detectors. This necessitates extensive research and development to enhance their radiation hardness and tracking performance while maintaining a low leakage current and minimised material budget.

Hybrid planar and 3D silicon pixel detectors have demonstrated a promising balance between these critical properties. Before their installation in the Inner Tracker, these detectors undergo rigorous testing at various research facilities and institutions worldwide.

Prior to full-scale production, pre-production batches of detector modules and test structures must be thoroughly evaluated to ensure they meet the stringent requirements for the upgrade. Beam tests play a vital role in assessing the performance of these modules by benchmarking their detection efficiency with high-energy particles, using minimum ionising particles. Beam tests for the ATLAS Inner Tracker have been conducted at CERN using particle beams extracted from the Super Proton Synchrotron. A sophisticated tracking setup, incorporating multiple high-precision tracking layers with spatial resolutions on the order of $\approx 5\,\mu\text{m}$, is employed to reconstruct particle trajectories with high accuracy.

This thesis presents investigations into test structures at TU Dortmund and pre-production module performance at CERN beam tests. Chapter 2 provides an in-depth discussion of the CERN accelerator complex, the ATLAS experiment, and the Inner Tracker upgrade. Chapters 3 and 4 explore the principles of silicon sensors and hybrid detectors, respectively. Performance studies on pre-production test structures and hybrid quad modules are presented in Chapters 5 and 7. The beam test results of the hybrid quad modules are currently being prepared for publication. Furthermore, the effect of front-end clocking on Inner Tracker pixel module performance is analysed in Chapter 8. Beam test simulations employing high-density beams are also conducted to benchmark the current tracking setup, as detailed in Chapter 6. Finally, a summary of the results and their implications for the upcoming Inner Tracker upgrade is provided in Chapter 9.

2 The ATLAS Experiment at the Large Hadron Collider

The investigation of subatomic particles in the high-energy regime is crucial for advancing our understanding of particle physics. Particle accelerators are essential tools in this endeavour, enabling the study of fundamental particle properties and their interactions. By accelerating particles to high energies and facilitating their collisions, we can observe processes under conditions akin to those of the early universe.
The largest particle accelerator in the world, the Large Hadron Collider (LHC) [1], is located at the European Organization for Nuclear Research (CERN) near Geneva. Among its most notable achievements is the discovery of the Higgs boson [2], an elementary particle predicted by the Standard Model of particle physics. Despite such milestones, many questions remain unanswered within our current theoretical framework. For instance, the nature of dark matter [3] is still unknown, driving the search for new particles and phenomena beyond the Standard Model. As such, collider physics continues to be of paramount importance in deepening our understanding of fundamental physical processes. The following sections go into further detail about the LHC and specifically the ATLAS Experiment [4] at the LHC.

2.1 The Large Hadron Collider

The Large Hadron Collider (LHC) began operations in 2009 and is currently the most powerful particle accelerator in the world. It allows scientists to accelerate protons to a centre-of-mass energy of $\sqrt{s} = 14\,\mathrm{TeV}$ since the start of Run 3 in 2022 [5]. Previously, the maximum centre-of-mass energy was $\sqrt{s} = 7\,\mathrm{TeV}$ during Run 1 (2009) and $\sqrt{s} = 13\,\mathrm{TeV}$ during Run 2 (2015). In addition to protons, the LHC also accelerates and collides lead ions to study quark-gluon plasma [6].

Before particles are injected into the LHC, they pass through a series of four pre-accelerators, each increasing their energy incrementally. Initially, protons are extracted from hydrogen gas using a duoplasmatron [7]. These protons are then accelerated to 160 MeV by the LINear ACcelerator, LINAC4 [8]. Subsequent accelerations occur in the Proton Synchrotron Booster, the Proton Synchrotron (PS), and the Super Proton

Synchrotron (SPS), bringing the total energy to 450 GeV [9]. In addition to preparing particles for the LHC, these pre-accelerators also supply particles for fixed target experiments. Figure 2.1 provides a schematic depiction of the CERN acceleration complex.

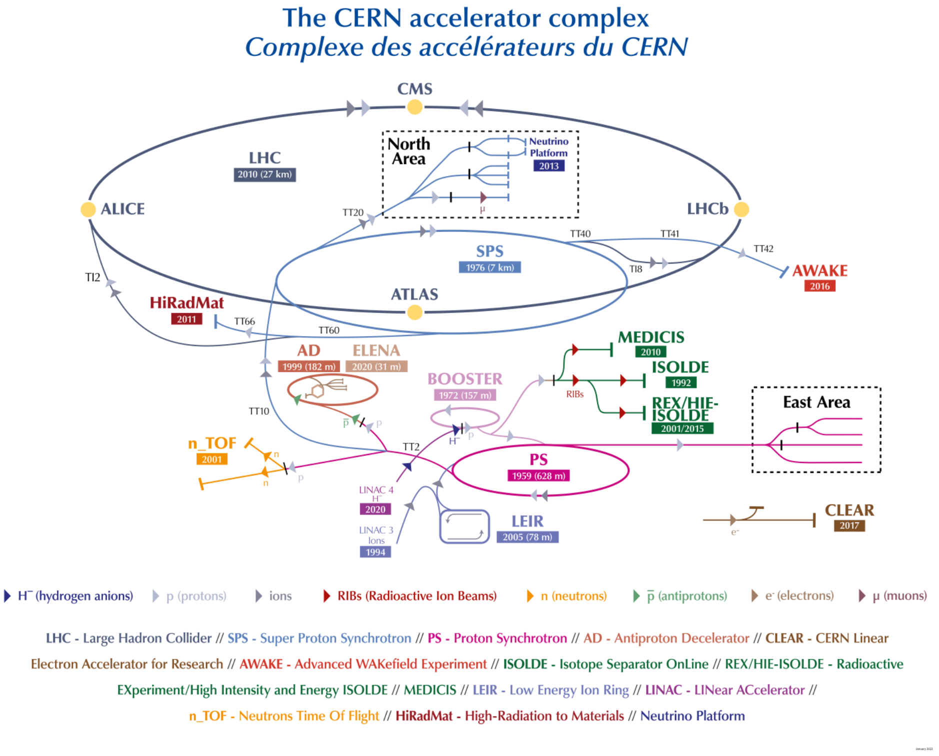

Figure 2.1: Schematic representation of the CERN accelerator complex [10].

The accelerated protons enter the LHC in one of two beam pipes, circulating either clockwise or anticlockwise. Superconducting magnets stabilise and focus the proton beams during circulation, while accelerating structures increase the energy of the protons to 7 TeV [11].

There are four interaction points where the particles collide, corresponding to the locations of the four major LHC experiments: ALICE (A Large Ion Collider Experiment) [12], LHCb (Large Hadron Collider beauty) [13], CMS (Compact Muon Solenoid) [14], and ATLAS [4]. Each of these detectors has a distinct design and purpose.

ALICE is a general-purpose detector with a focus on lead-lead and lead-proton collisions, enabling the study of quark-gluon plasma. LHCb is dedicated to b-physics and the study of CP-violating processes. Both ATLAS and CMS are general-purpose detectors designed to search for a wide range of phenomena beyond the Standard Model.

2.2 The ATLAS Experiment

The ATLAS experiment is a cylindrical general-purpose detector with a length of 46 meters, a diameter of 25 metres, and a weight of 7000 tonnes [15]. The detector is depicted in Figure 2.2.

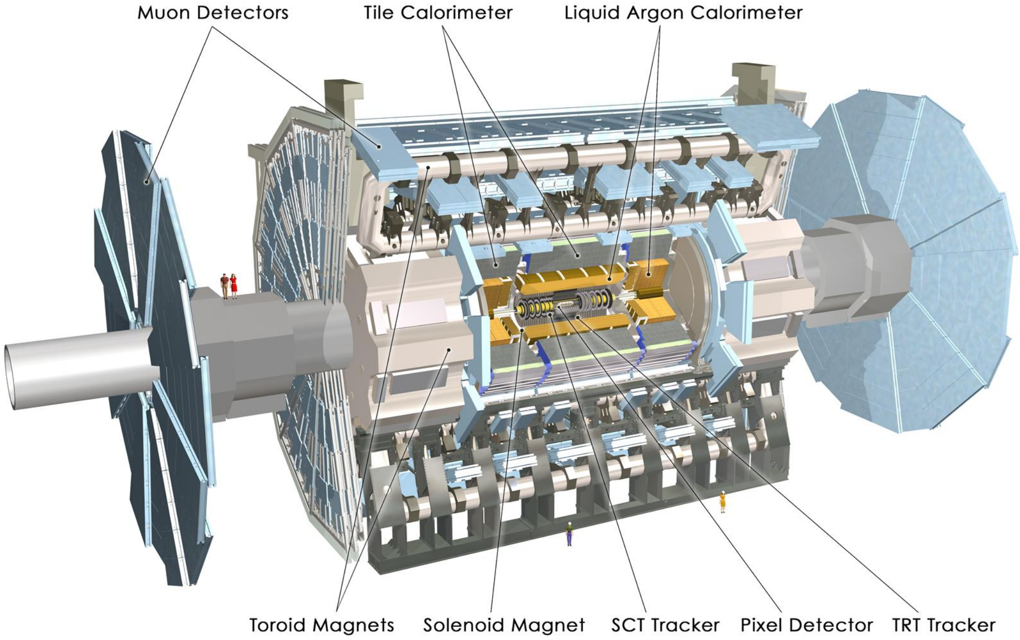

Figure 2.2: Schematic representation of the ATLAS detector and its components [16].

The proton-proton collisions within the ATLAS detector produce a variety of particles, each passing through different detector systems designed to measure specific properties. The primary properties of interest are the mass, momentum, energy, and trajectory of these particles, which help identify their types.

The Inner Detector [17] tracks charged particles and determines their momentum. The electromagnetic and hadronic calorimeters measure the energy of photons, electrons, and hadrons. These detector systems are arranged in layers around the interaction point in a cylindrical structure known as the barrel. The detector systems are also used in several end-cap disks that are positioned orthogonally to the beam direction to cover most of the solid angle. Figure 2.3 illustrates the interactions of various particles with the corresponding detector systems. The following subsections provide a detailed description of the different detector systems of the ATLAS experiment.

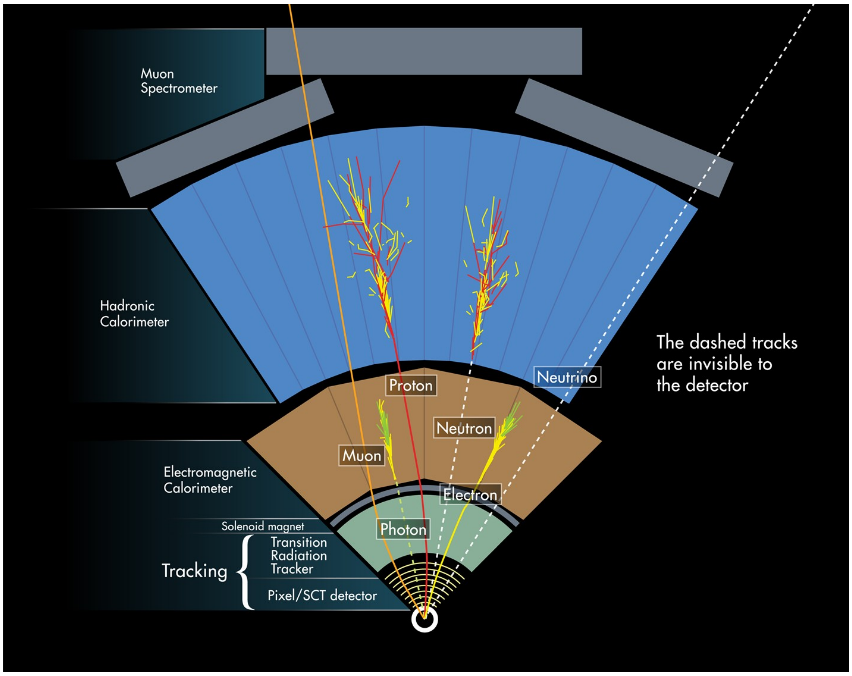

Figure 2.3: Schematic representation of various particles interacting with the detector systems of the ATLAS experiment [18].

2.2.1 The Muon Spectrometer

Since muons have a significantly higher mass than electrons, they produce less bremsstrahlung when traversing the detector at high energies. Additionally, muons rarely interact with the Inner Detector and calorimeter systems. Therefore, identifying muons and determining their trajectories is primarily accomplished by the outermost detector system, the Muon Spectrometer [19].

To maximise detection, the Muon Spectrometer spans a large area, extending radially from the end of the hadronic calorimeter at 4.25 m to the outer edge of the detector at 11 m. This design allows the spectrometer to cover a pseudorapidity range up to $|\eta| = 1$, while the end-caps cover a pseudorapidity of $1 \leq |\eta| \leq 2.7$. The spectrometer comprises resistive plate chambers and monitored drift tubes in the barrel region, while the end-caps make use of cathode strip chambers, thin gap chambers and monitored drift tubes.

The superconducting barrel toroid and the end-cap toroid magnets generate a 4 T magnetic field, causing the muons to curve due to the Lorentz force. By analysing this curvature, both the charge sign and the momentum of the muons are determined. The stand-alone relative momentum resolution of the Muon Spectrometer is approximately 4 %, increasing to 11 % for transverse momenta of 1 TeV.

2.2.2 The Electromagnetic and the Hadronic Calorimeter

Different sampling calorimeters [4] are installed in the ATLAS detector between the muon spectrometer and the solenoid to measure the energy of a multitude of particle types. The hadronic calorimeter in the outer region covers a radius of 2.28 m to 4.23 m in the barrel and 0.475 m to 2.03 m in the end-caps with two wheels in each end-cap. It is used to measure the energy of hadron particle showers to infer the energy of the initial hadronising particle. This is achieved by using alternate layers of absorber and scintillating materials. The active material produces scintillation light, which is transmitted by a wavelength shifter to photomultiplier tubes. In the barrel region, steel is used as an absorber to contain the particle shower within the calorimeter, and plastic scintillator tiles are used to sample the energy of the hadronic shower. In the end-cap region, the absorber and sampling materials are changed to copper and liquid argon, respectively, due to the higher radiation exposure.

The electromagnetic calorimeter [20] is located in the inner region of the calorimeter system, spanning over a radius from 1.15 m to 2.25 m in the barrel and 0.33 m to 2.098 m in the end-caps with one wheel in each end-cap. The energy of electrons, positrons, photons and partially hadrons is measured in the electromagnetic calorimeter. It features an accordion structure of lead as the absorber and liquid argon as the sampling material for optimal energy measurements in the radial direction without gaps. The end-cap region uses the same absorber and sampling materials. A cryostat surrounds the electromagnetic calorimeter to keep the argon in liquid form. A total pseudorapidity of up to $|\eta| = 1.7$ is covered by the hadronic and electromagnetic calorimeters of the central region and up to $|\eta| = 3.2$ by the calorimeters in the end-cap region. The forward calorimeter uses liquid argon for sampling and copper and tungsten as absorbers for the electromagnetic and hadronic showers, respectively. It covers a region of up to $|\eta| = 4.9$.

2.2.3 The Inner Detector

Being positioned closest to the interaction point at a distance of 1.2 cm, the Inner Detector (ID) [21] is used to track charged particles with high spatial resolution. It has a highly sensitive area, covering a pseudorapidity of up to $|\eta| = 2.7$ and is designed to be sufficiently radiation hard to maintain a high detection efficiency for many years. Furthermore, as the innermost detector system, the material budget of the ID is minimised to reduce energy loss and deflection of charged particles due to multiple Coulomb scattering.

A 2 T inhomogeneous magnetic field parallel to the beam axis is generated by a superconducting solenoid [22], which curves the trajectories of charged particles. The ATLAS solenoid is 5.8 m long, 2.56 m in diameter, and surrounds the entire ID. The ID comprises three sub-detector systems: the Pixel Detector (PD), the Semiconductor Tracker (SCT) and the Transition Radiation Tracker (TRT), which are depicted in Figure 2.4.

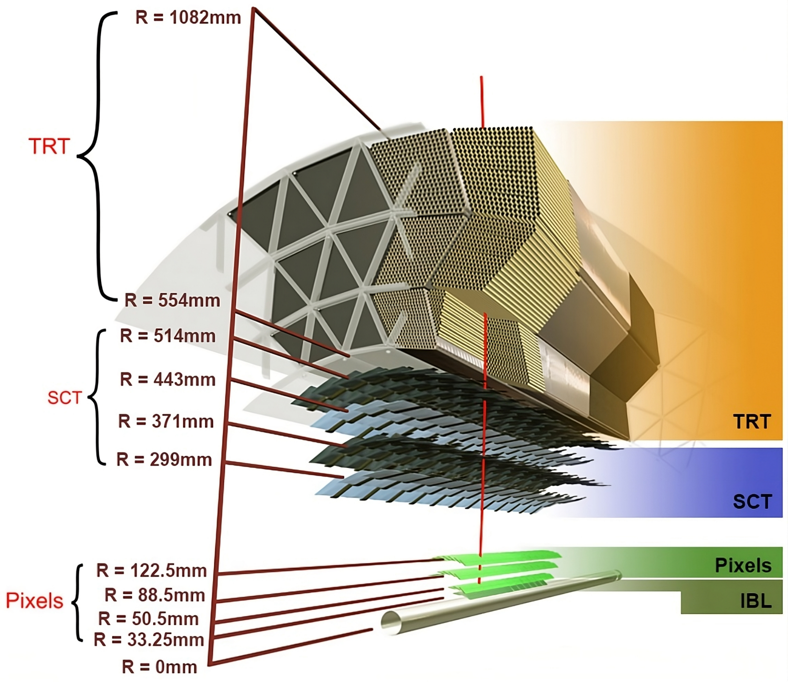

Figure 2.4: Schematic representation of the different sub-detector systems of the Inner Detector [23].

The Transition Radiation Tracker

The outermost layer of the ID is the Transition Radiation Tracker (TRT) [24, 25], which consists of 300,000 thin-walled drift tubes distributed across the barrel region and both end-caps. It is used to track particles that ionise the $Xe/CO_2/O_2$ gas mixture in the drift tubes, commonly referred to as straws. Due to the applied electric field, the generated electron-ion pairs are separated, inducing a measurable charge.
The straws are made of Kapton with a gold-plated tungsten wire at the centre, and have a diameter of 4 mm. In the barrel region, the straws are 144 cm long and are arranged parallel to the beam axis in a total of 73 layers. The straws in the end-caps are 39 cm long and are arranged radially in wheels. Additionally, polypropylene fibers are placed between the straws to generate transition radiation, which is useful for particle identification. This is particularly effective for determining the mass m of electrons and pions with a known energy E, as the transition radiation effect depends linearly on the Lorentz factor $\gamma = E/(mc^2)$.
The TRT is designed to cover a large volume of $12\,\mathrm{m}^3$ at the expense of spatial resolution, which is approximately 130 µm in the direction perpendicular to the straws. On average, 30 hits are registered from an ionising particle traversing the TRT.

The Semiconductor Tracker

The middle subsystem of the ID is the Semiconductor Tracker (SCT) [26, 27], which surrounds the Pixel Detector and spans from 29.9 cm to 51.4 cm in the radial direction. It consists of 4,088 two-sided silicon detector modules, arranged in four cylindrical barrel layers and nine planar end-cap disks on each side.

In the barrel region, each module is composed of four rectangular silicon microstrip sensors with a strip pitch of 80 µm and a length of 12 cm. Two modules are glued together at a 40 mrad angle relative to each other, with one module on the front side and another on the back side. By combining the information from the front and back sensors, a spatial resolution of 17 µm in the $R\phi$ direction and 580 µm in the Rz direction is achieved.

The sensors used in the end-caps have a trapezoidal shape and are oriented perpendicular to the beamline. The strip modules are designed to withstand a fluence of $2 \times 10^{14}\ \mathrm{n_{eq}/cm^2}$, which is estimated to be reached during the lifetime of the SCT.

The Pixel Detector

The innermost subsystem of the ID is the Pixel Detector (PD) [28], which is positioned at a distance of 5 cm from the beam line and extends to a radius of 12.25 cm. It consists of 1,744 silicon pixel modules distributed across three barrel layers and three end-cap disks on each side. The majority of pixel modules have a pixel size of $50 \times 400\ \mu\mathrm{m}^2$, with 47,232 pixels per module, which are read out by an integrated readout ASIC, called the FE-I3.

The PD can precisely measure three hit positions of ionising particles close to the beam pipe. This information significantly contributes to the identification of short-lived particles and to the reconstruction of particle tracks. Furthermore, the deposited charge in the sensor can be determined using time-over-threshold information. The modules are designed to operate up to a bias voltage of -600 V to maintain their efficiency under increasing radiation exposure over time. To minimise leakage current, the modules are cooled to $-10\,^{\circ}\mathrm{C}$.

The detector is designed to withstand a fluence of $1 \times 10^{15}\ \mathrm{n_{eq}/cm^2}$, although the fluence after ten years was expected to reach $5 \times 10^{15}\ \mathrm{n_{eq}/cm^2}$ for the innermost layer, called the B-Layer. Consequently, the B-Layer was initially designed to be replaceable, although the final design did not include this feature. Instead, an additional layer was installed during Long Shutdown 1 in 2013, called the Insertable B-Layer (IBL) [29]. The IBL surrounds the beam pipe at a distance of 3.3 cm and consists of 280 silicon pixel modules using the newer FE-I4 readout ASIC. This module features an even smaller pixel size of $50 \times 250\ \mu\mathrm{m}^2$, further improving the tracking capabilities of the PD. Due to its close proximity to the beam pipe, the IBL is designed to minimise the material budget and withstand a fluence of $5 \times 10^{15}\ \mathrm{n_{eq}/cm^2}$.

At the end of 2024, the B-layer and the IBL had to withstand a fluence of 1.4 and $1.9 \times 10^{15}\,\mathrm{n_{eq}/cm^2}$, respectively. Thus, the pixel detector is operated well beyond its life expectancy during Run 3, while still reaching efficiencies of approximately 94 % [30].

2.3 The High Luminosity LHC

To increase the potential for discovering new physics, the CERN project of the High Luminosity LHC (HL-LHC) [31] was approved in 2016. With the HL-LHC, the peak instantaneous luminosity for proton-proton collisions is expected to reach up to $7.5 \times 10^{34}\,\mathrm{cm^{-2}s^{-1}}$, which will lead to an average pile-up of 200 interactions per bunch crossing at the same rate of 40 MHz. Thus, a total integrated luminosity of $4000\,\mathrm{fb^{-1}}$ will be collected over the period of twelve years. This allows physicists to study rarely occurring processes in greater detail, as particles like the Higgs boson will be produced approximately five times more often in the same amount of time.
The HL-LHC upgrade will be installed during the Long Shutdown 3 period from 2026 to 2028, with operations starting in 2029. Upgrades for all four large experiments at the LHC are planned to be installed during this period, as the increasing instantaneous luminosity demands improved radiation hardness, precision, and data acquisition. Figure 2.5 depicts the overall timeline of the different LHC phases, including the installation of detector upgrades for the primary LHC experiments.

The focus of this thesis lies on the upgrade of the ID of the ATLAS experiment for the HL-LHC, called ATLAS Inner Tracker. Thus, the following section further elucidates this project.

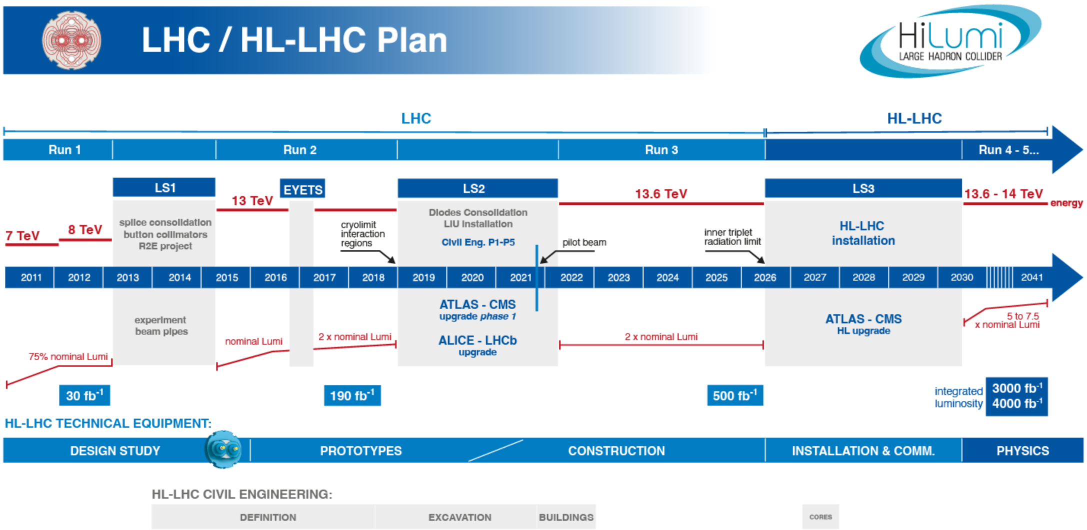

Figure 2.5: Depiction of the timeline of the HL-LHC plan from the design studies to installation and operation [32].

2.4 The ATLAS Inner Tracker

The ATLAS Inner Tracker (ITk) [33] will replace the Inner Detector for the HL-LHC phase starting in 2030. It is designed to cope with the harsh environment of the HL-LHC, such as the increased pile-up requiring improved readout rates. To keep the occupancy of the detector below 1 %, the granularity of the detector will be increased. Furthermore, it has to withstand the higher radiation damage for many years while the performance is aimed to be equal to or better in comparison to the ID. The ITk will be built as an all-silicon detector to fulfil these requirements while minimising the material budget, thereby ensuring accurate energy measurements in the calorimeter system. It will consist of several inner layers of pixel sensor modules and outer layers of strip modules covering pseudorapidities of up to $|\eta| = 4$. Figure 2.6a depicts the layout of the detector and 2.6b shows a distribution of the number of hits of the silicon sensors as a function of the pseudorapidity. A 3D visualisation of the ATLAS ITk including its layers and support structure is shown in Figure 2.6c.

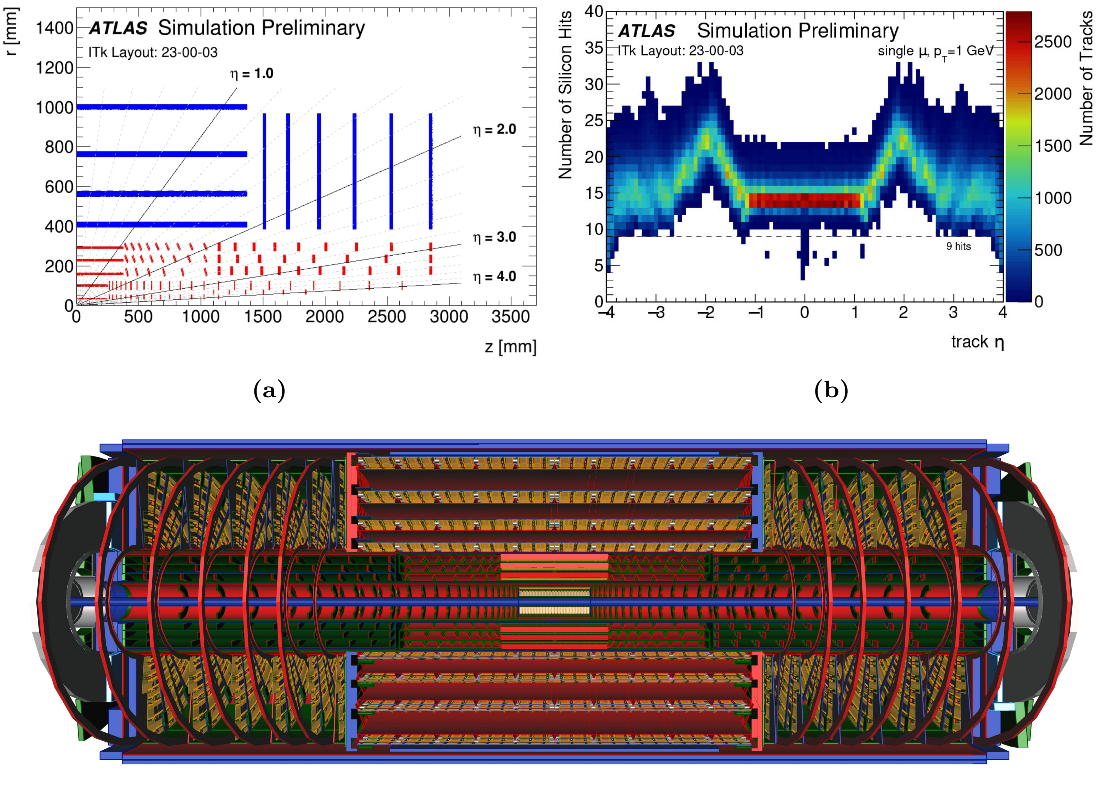

(a) **(b)**

(c)

Figure 2.6: a) Layout of the layers of pixel modules in red and strip modules in blue of one quadrant of the ITk. b) Simulation of the number of registered hits as a function of the pseudorapidity. A sample of 1 MeV muons is used, which were generated with a flat distribution in transverse direction for the different values of $z = -15\,\mathrm{cm}$, $0\,\mathrm{cm}$ and $15\,\mathrm{cm}$ in equal amounts. c) Visualisation of the detector modules and the support structure layout of the ITk [33].

The entire ITk will be permeated by a 2 T magnetic field produced by the solenoid for momentum measurements of charged particles. Occupying the same volume as the ID, the ITk will span the radius from 3.3 cm to 100.8 cm. The following sections will describe the ITk layout and the detector modules in more detail, while even further detailed descriptions of the ATLAS ITk can be found in the technical design reports of the ITk pixel [34] and strip detectors [35].

2.4.1 The Strip Tracker and the ITk Strip Modules

At a distance of 40 cm to a 100 cm from the beamline, silicon strip modules are used for particle tracking. The strip tracker consists of four layers of strip modules in the barrel region and six disks on each side in the forward region, referred to as the end-caps. With the Strip tracker, an area with a pseudorapidity of $|\eta| = 2.7$ will be covered. In the barrel region, rectangular short (SS) and long (LS) strips with a length of 2.5 cm and 5 cm will be utilised in the inner two and outer two layers, respectively. Figure 2.7 shows an SS module on a test frame.

Each stave holds 28 modules and is arranged cylindrically to form the barrel, which will contain approximately 11,000 strip modules. The disks consist of 32 trapezoidal petals that are arranged in a circular shape. Each petal holds twelve strip modules of six different sizes, R0 to R5. In total, approximately 7000 strip modules will be mounted on the petals in the end-caps. Figure 2.8 shows a schematic of a loaded stave and a petal. The modules are operated at −35 °C, which is achieved by a flowing bi-phase CO_2 that is transported via titanium pipes to the modules.

Both the SS and the LS modules have a similar size of $10 \times 10\,\text{cm}^2$, with the SS using four rows of strips and the LS using two rows. Each row consists of 1280 signal strips and two edge strips.

The barrel strips are supported by a flexible circuit board, called a hybrid. One hybrid is required for two strip segments. A short strip sensor uses two hybrids and a long strip sensor uses one. Two ASICs are mounted on a hybrid. The binary readout chip of the strip, called ABCStar (ATLAS Binary Chip), processes the hit information, while the HCCStar (Hybrid Control Chip) controls the readout of the ABCStar. Additionally, a flex circuit board, called the power board, distributes the power to the different parts of the module and holds a monitoring chip, the AMACStar (Autonomous Monitor and Control Chip). All the electrical components were designed to be compatible with the strip design of the barrel and the end-caps.

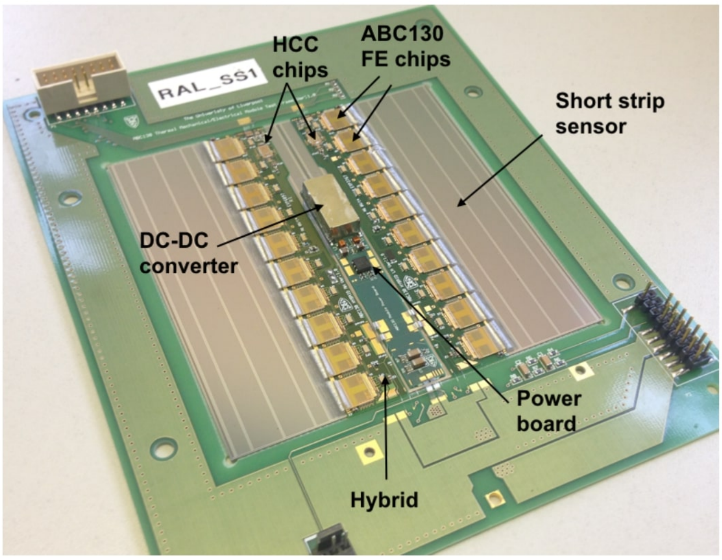

Figure 2.7: A short strip module mounted on a short strip test frame. Two hybrids are mounted between two strip segments with one powerboard in the centre. The prototype of the ABCStar, called the ABC130 was utilised [35].

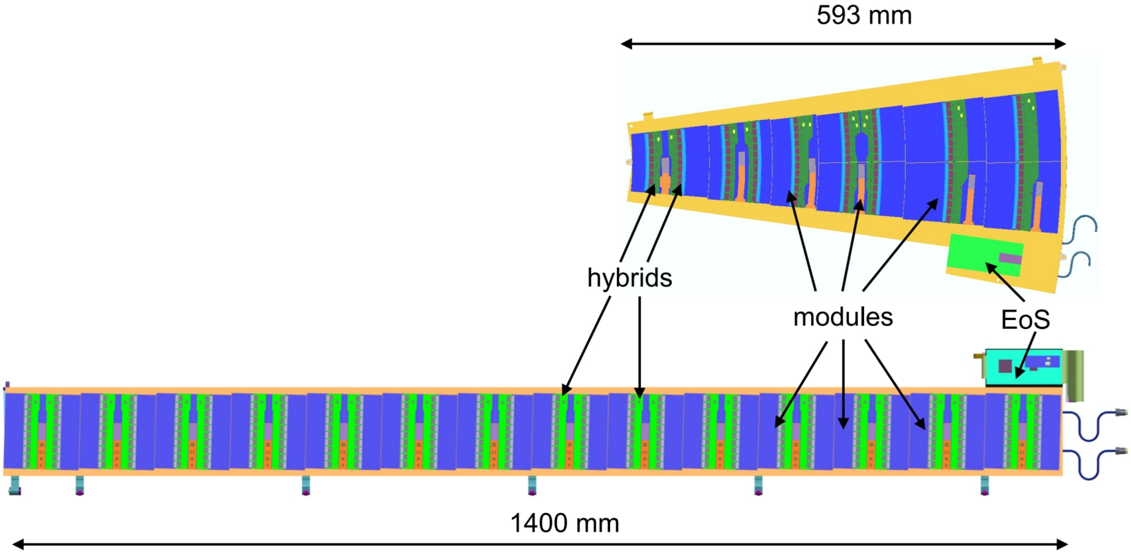

Figure 2.8: Schematic of a petal and a stave that hold various strip modules and the End of substructure cards [35].

2.4.2 The Pixel Tracker and the ITk Pixel Modules

This section describes in detail the ITk pixel detector and ITk hybrid pixel modules that were investigated in the scope of this thesis. A more general introduction to hybrid pixel detectors is given in Chapter 4.
The ITk Pixel Tracker is the detector system closest to the beam pipe and therefore crucial for particle tracking and vertex reconstruction.
It consists of five layers of pixel modules, loaded on staves, in the cylindrical barrel region, called L0 to L4, and several concentric rings in the respective layers, called R0 to R4. The Inner System consists of the two innermost layers of staves and rings. Three different designs for the Inner System rings exist. Coupled rings cover the layers L0 and L1 and are utilised closer to the barrel. The intermediate rings and the L1 rings cover the layers L0.5 and L1, respectively.
The 2 m long staves in the outer barrel, so-called longerons, are loaded with modules parallel to the beam line. Inclined half rings are used in between the longerons and the outer end-caps to keep the orientation of the modules normal to the particle tracks. Approximately 8400 modules will be loaded into the Pixel Tracker.
Electrical and cooling services run along the staves and the ring support cylinder. Similar to the ITk Strip Tracker, a biphase CO_2 cooling system is used to cool the modules via thin-walled titanium pipes. Figure 2.9 shows the support structures of the inner system, the outer barrel and the outer end-cap.

At a distance of 3.4 cm from the beamline, the innermost layer has to withstand fluences of up to $2 \times 10^{16}\,\mathrm{n_{eq}/cm^2}$ over a period of six years, which is expected to be half the operation time. Afterwards, the inner two layers and rings will be replaced by an identical second inner system.
Silicon hybrid 3D modules will be installed on the first layer only, due to their high radiation hardness in comparison to planar sensors. A single 3D module has a pixel matrix of 384×400 pixels that span over an area of $2 \times 2\,\mathrm{cm^2}$ and an active thickness of 150 µm. It was determined that 3D sensors with a pixel size of $25 \times 100\,\mathrm{\mu m^2}$ in the barrel and $50 \times 50\,\mathrm{\mu m^2}$ in the end-caps improve the tracking performance of the detector. Most 3D modules will be loaded as triplets, which means that three front-ends (FEs) will be bonded on a single silicon tile each and connected to one flexible PCB. The Layers L1 to L4 and their corresponding rings will be loaded with 150 µm thick n^+-in-p planar hybrid quad modules. A quad module consists of four FEs bonded on a single silicon tile. Thus, the pixel matrix of a quad module spans 768×800 pixels in a $4 \times 4\,\mathrm{cm^2}$ area. A gap between the four readout chips is inevitable. Therefore, four rows and columns of large $100 \times 50\,\mathrm{\mu m^2}$ and $50 \times 100\,\mathrm{\mu m^2}$ pixels are incorporated in the design as an interchip region to avoid an inactive area between the readout chips. The 16 pixels in the centre have a dimension of $100 \times 100\,\mathrm{\mu m^2}$.

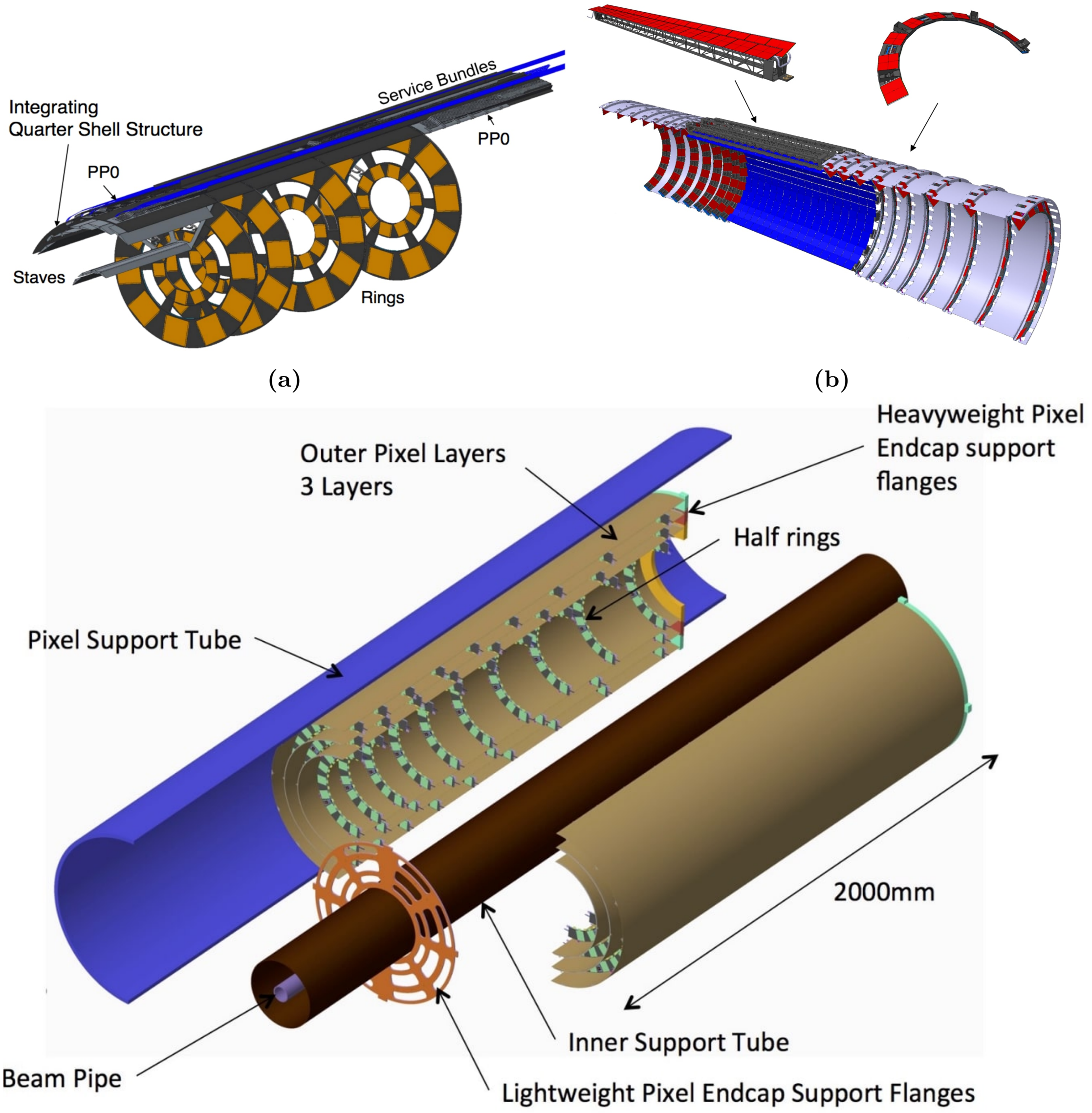

(a) **(b)**

(c)

Figure 2.9: a) Quarter shell structure of the inner system, including the layer L0 and L1 staves and coupled rings. Only four rings are shown for better visualisation. b) Longerons and inclined rings in the outer barrel and layer [36]. c) One of the outer end-caps of the Pixel Tracker [34].

Figure 2.10a and 2.10b show a quad module and a magnified view of the quad sensor pixel structure, including interchip pixels.
An ITk pixel module is manufactured in two major steps. First, the FE is bump-bonded to the silicon tile. Afterwards, the bare module is glued to the flex PCB, which manages and distributes the necessary power to the electrical components. Planar and 3D sensors are described in more detail in Section 4.2. Optimising the sensor technology incorporated in the Pixel Tracker was achieved with extensive studies and is described in more detail in [37].

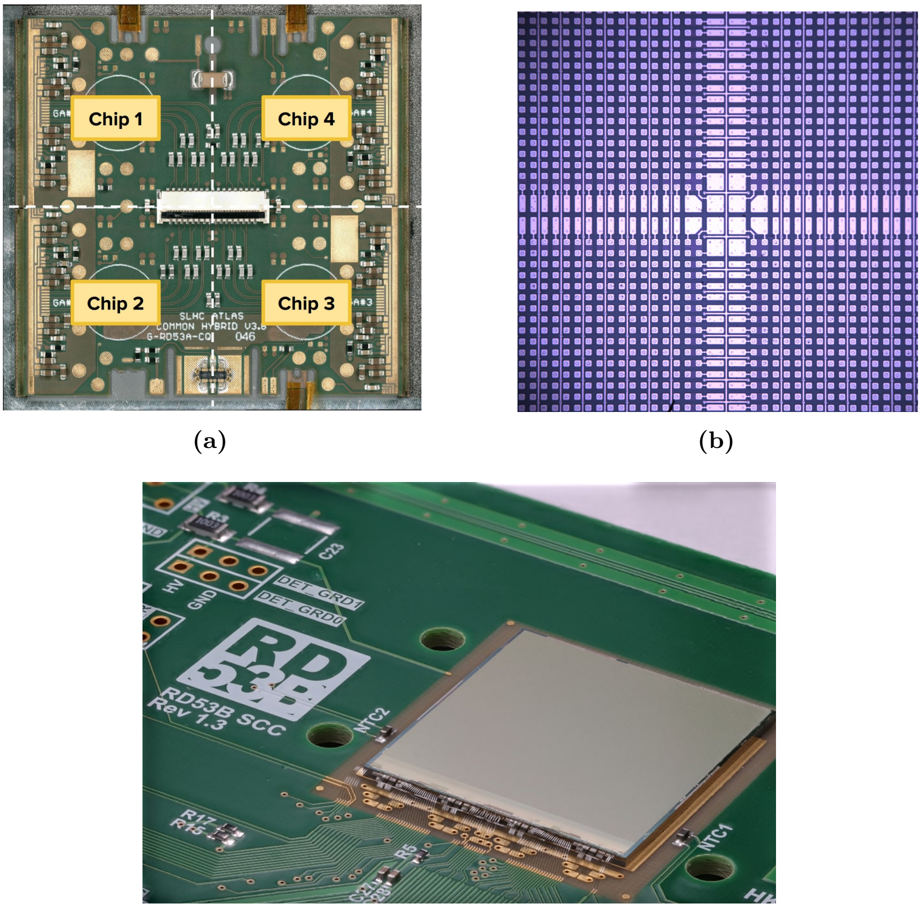

(a)

(b)

(c)

Figure 2.10: a) Example of an assembled RD53a quad module. The PCB that is glued to the sensor tile is visible [38]. b) Close-up photo of the pixel matrix of a quad sensor tile, including the bias structure and the interchip region. Four rows and columns of large pixel implants are utilised (purple areas). c) Close-up of an ITkPixV1 FE on a single chip card [39].

All hybrid modules in the Pixel Tracker will use the ITkPixV2 readout chip based on 65 nm technology and developed by the RD53 Collaboration [40]. The FE chip prototype, called RD53a, contained three different design architectures for both the ATLAS and the CMS collaborations to investigate their needs. With the prototype, it was demonstrated that the FE met the expected requirements of ATLAS and CMS regarding radiation tolerance, low threshold operation and trigger rate.

Eventually, the ATLAS collaboration chose to pursue the differential FE architecture, which stems from its differential precomparator design. Using differential signals allows for improved signal integrity, reducing the signal-to-noise ratio and the effect of signal distortions.

The FE chip was further refined to the needs of the ATLAS collaboration until the newer ITkPixV1 pre-production chip was submitted in 2020, which is shown in Figure 2.10c. A few bugs, most notably the high power-up current of the chip that made system tests impossible, led to an updated version of the chip, called ITkPixV1.1. Most of the ITk pixel modules that were investigated within the scope of this thesis had the ITkPixV1.1 incorporated. The final design FE ITkPixV2 was equipped to modules starting from 2024 and fixed several issues found during extensive testing of ITkPixV1.1 modules. Figure 2.11 depicts the differential analog FE and the main components for the signal processing schematically.

In the following, the fundamental processing of an incoming signal in the differential FE is briefly explained. A charge signal is induced into the analog FE by a detector diode, when ionising particles traverse the bonded sensor, or by an injection input for testing purposes. The signal charges the feedback capacitance C_f of the charge-sensitive amplifier. Afterwards, the discharging effect of the constant current source I_ff creates a triangular voltage signal for the precomparator inputs proportional to the initial charge signal. The detection threshold of the precomparator is defined by the crossing points of the two input voltages and can be adjusted with the supply voltages of the precomparator globally and per pixel with the TDAC register. Both signals get amplified by the precomparator before being fed in to the comparator, which converts the inputs into a binary signal. The output is digitised and further processed.

The FE of the ITk pixel modules is designed to support the serial powering of up to 14 modules, so material for the serving cables is saved, which improves the tracking performance. The readout chip assumes a constant current instead of a constant voltage power supply and generates a constant internal voltage with a shunt low-dropout voltage regulator. These regulators are based on the successful regulators of IBL modules, although no serial powering was used in the IBL.

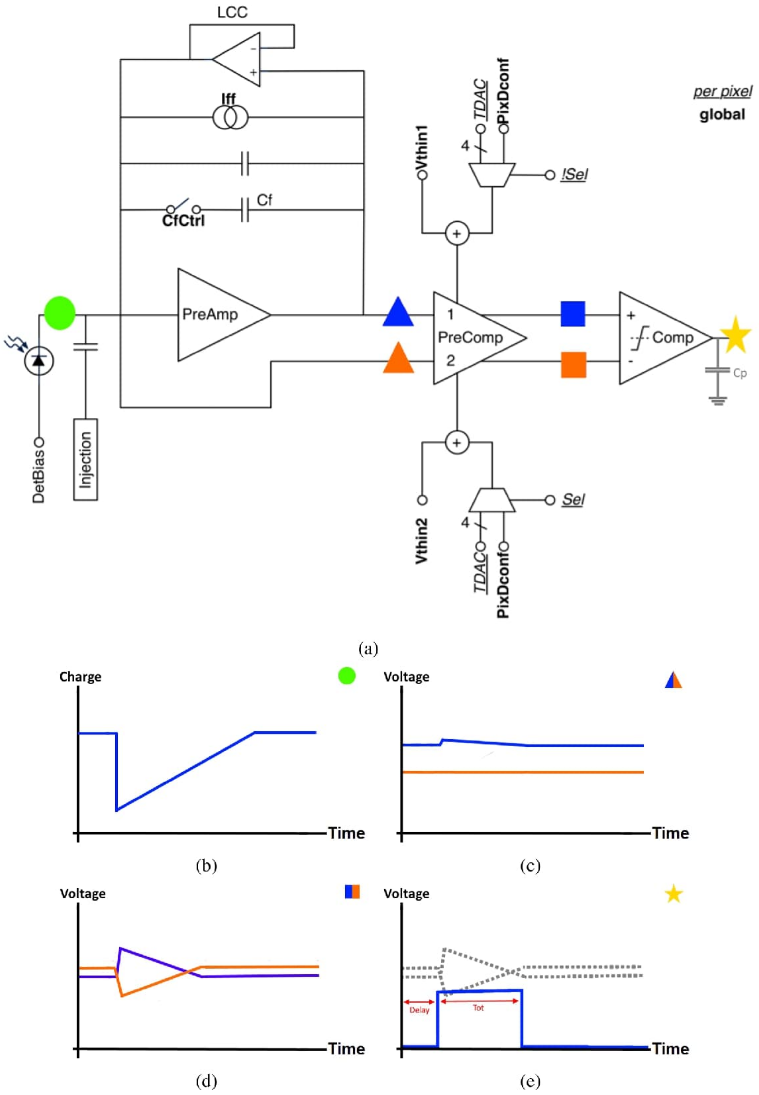

(a)

(b)

(c)

(d)

(e)

Figure 2.11: a) Schematic of the differential analog FE. Its main components from left to right are the current input, the preamplifier, the precomparator and the comparator. The boldfaced signals are controlled globally, while the underlined italic signals are controlled per pixel. b) A current flows from the sensor diode. c) A signal after being processed by the preamplifier. d) The two output signals of the precomparator. e) The digital signal after the comparator [41].

3 Silicon Detectors

Detectors play a fundamental role in particle physics research, enabling the study of particle properties. Since different types of particles interact with their surroundings in distinct ways depending on their type and properties, detectors must be optimised for specific experimental requirements. At the LHC, particle detectors are specialised to identify and analyse high-energy particles produced in proton-proton collisions, measuring key properties such as energy, momentum, and trajectory.

A broad range of detector technologies is employed both in particle physics and other fields. Among these, semiconductor-based detectors are particularly prominent. In addition to their widespread use in scientific research, they find extensive applications in industry, particularly in general-purpose electronic devices.

This chapter provides a brief introduction to semiconductor physics and hybrid pixel detectors.

3.1 Semiconductors

Semiconductors are a class of materials with unique electronic properties that lie between those of conductors, such as metals, and insulators, such as ceramics. These properties arise from the behaviour of charge carriers, electrons (e^-) and holes (h), within the crystal lattice.

In isolated atoms, electrons occupy discrete energy levels. However, in a lattice, each atom is influenced by its neighbouring atoms through electromagnetic interactions. Considering the entire lattice, these discrete energy levels split many times, forming energy bands [42]. The highest energy band in which electrons remain bound to atoms is called the valence band, while the lowest energy band available for electron conduction is the conduction band.

In conductors, the valence and conduction bands partially overlap, allowing electrons to move freely within the lattice. Conversely, insulators have a wide energy gap between these bands, referred to as the band gap, preventing significant electron movement from the valence to the conduction band. Semiconductors have a smaller band gap, in the range of approximately 0.1 to 4 eV, compared to insulators, enabling electrons to transition from the valence to the conduction band if sufficient energy is provided. This energy can be supplied through thermal excitation or ionising particles. The band gap

of semiconductors at room temperature is typically on the order of 1 eV. Figure 3.1a illustrates the energy bands for conductors, semiconductors, and insulators.
When electrons move into the conduction band, they leave behind holes in the valence band. These holes can be filled by other electrons, allowing the holes to act as positive charge carriers that can move through the lattice.

One of the most widely used semiconductor materials is silicon, due to its abundance in the Earth's crust in the form of silica and silicates. This abundance makes silicon relatively inexpensive and easily accessible for both industrial and academic applications. Silicon has a stable diamond cubic crystal structure, as shown in Figure 3.1b, and can be produced with high purity.
Silicon exhibits a band gap of 1.12 eV at room temperature (300 K). However, the minimum energy states of the conduction band and the maximum energy states of the valence band are offset in momentum space. As a result, a momentum transfer from electrons to the crystal lattice is required for a transition into the conduction band. Semiconductors with this characteristic, such as silicon and germanium, are classified as indirect semiconductors.
In contrast, materials like gallium arsenide are examples of direct semiconductors, commonly used in light-emitting diodes due to their efficient electron-hole recombination. Consequently, the average energy needed to create an electron-hole (e/h) pair in silicon, 3.65 eV, is significantly larger than its band gap.

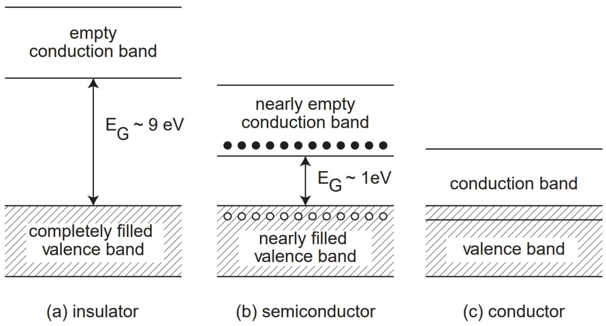

(a)

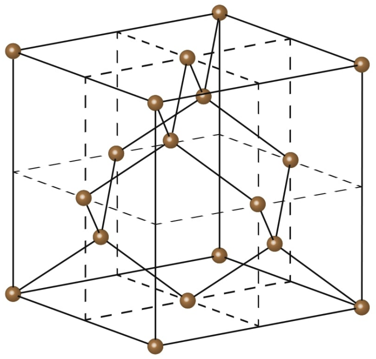

(b)

Figure 3.1: a) Band structures of insulators, semiconductors and conductors. Here, E_G denotes the energy gap. b) Cubic face-centred lattice structure of semiconductors such as silicon and germanium [43].

3.2 Doping of Semiconductors

The conduction properties of semiconductors can be modified by introducing impurities into the crystalline structure, a process known as doping. A doped semiconductor is referred to as extrinsic, while an intrinsic semiconductor is one that is essentially pure, with no significant amount of impurities present.

Silicon and germanium atoms are tetravalent, meaning they form bonds with four neighbouring atoms. Impurities introduced by doping are typically pentavalent or trivalent, possessing one valence electron more or less, respectively, than the semiconductor atoms. A pentavalent atom, known as a donor, contributes an additional valence electron, while a trivalent atom, called an acceptor, introduces a hole. The extra electrons from donor atoms are only weakly bound and can be easily ionised because their ground state lies just below the conduction band.

Phosphorus and boron are commonly used as donor and acceptor atoms, respectively, due to their high diffusion rates. Semiconductors with a high concentration of donor atoms are classified as n-type materials, characterised by an excess of free electrons. Conversely, semiconductors with a significant number of acceptor atoms are p-type materials. Figure 3.2 illustrates a silicon lattice with both a donor and an acceptor impurity.

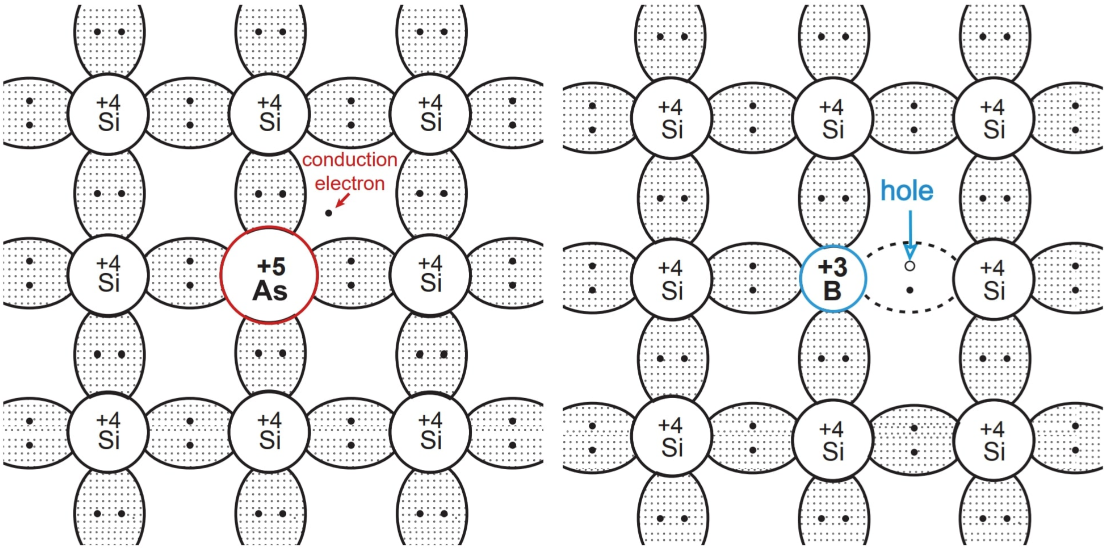

Figure 3.2: Schematic representation of a silicon lattice and the introduction of a donor (a) and an acceptor (b) [43].

3.3 The p-n Junction

A p-n junction is the interface between an n-type and a p-type semiconductor. When these two types of semiconductors come into contact, the excess holes from the p-type region and the excess electrons from the n-type region diffuse across the junction due to the concentration gradient, creating a diffusion current I_{diff}. As electrons recombine with holes near the boundary, a region depleted of free charge carriers forms, known as the depletion zone.
An electrostatic field develops due to the space charge of the dopant ions, generating a drift current I_{drift} that opposes the diffusion current. The drift current increases as more electrons and holes recombine, until an equilibrium is reached where the diffusion and drift currents balance, stabilising the depletion zone. Depletion zones can also form within semiconductors of the same type if the doping concentrations differ. In this case, regions with higher and lower doping levels are denoted as n^+ and n^-, respectively.

The electric field within the depletion zone creates a built-in voltage V_{bi}, which is approximately 0.6 V for silicon. Applying an external voltage V_{ext} across the p-n junction alters the size of the depletion zone by shifting the balance between diffusion and drift currents. When a positive voltage is applied to the p-side, the depletion zone narrows, and the junction is forward-biased, allowing current to flow. Conversely, a negative voltage applied to the p-side widens the depletion zone, creating a reverse bias that inhibits current flow. This mechanism underlies the basic operation of a diode, where current flows predominantly in the forward-bias direction. Figure 3.3 schematically illustrates the behaviour of the depletion zone in forward and reverse bias conditions.
The width d_{dep} of the depletion zone depends on the built-in voltage V_{bi}, the external voltage V_{ext}, the doping concentration $N_{\mathrm{D/A}}$, the elementary charge e, and the permittivities of vacuum ϵ_0 and the material ϵ_{r}:

$$d_{\mathrm{dep}} = \sqrt{\frac{2\epsilon_0\epsilon_{\mathrm{r}}}{e}\frac{1}{N_{\mathrm{D/A}}}(V_{\mathrm{bi}} + V_{\mathrm{ext}})} \tag{3.1}$$

Electron-hole pairs generated within the depletion zone do not recombine, as they are driven toward the opposite electrodes by the electric field created by both the electrodes and the space charge. Consequently, ionising particles passing through the depletion region can be detected by measuring the current induced by the movement of electrons and holes. This property makes p-n junctions highly suitable for use in sensors designed to detect charged particles. During operation, a sufficiently high external voltage is applied to fully deplete the p-n junction, maximizing the sensitive volume for particle detection.

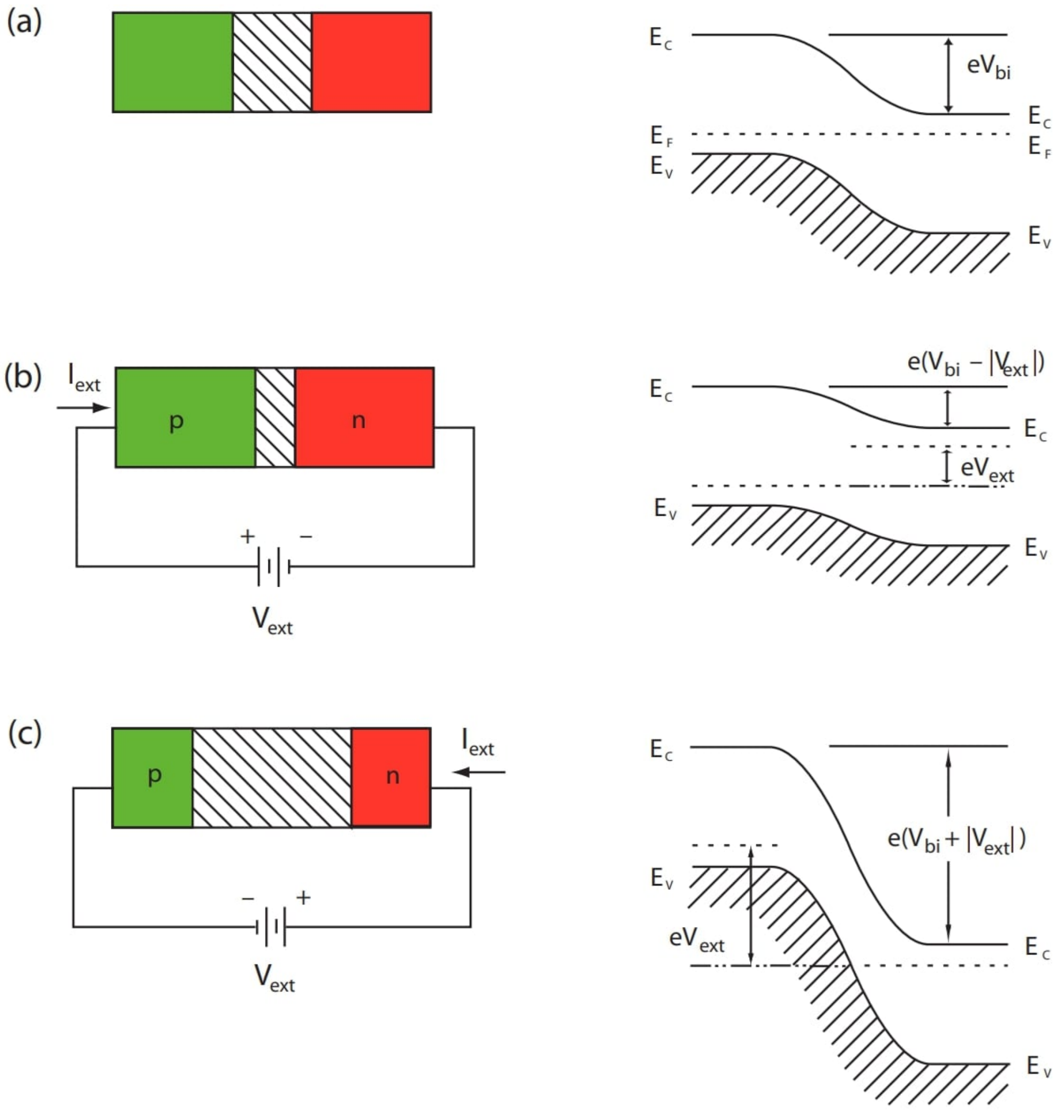

Figure 3.3: Schematic representation of the width of the depletion zone for different applied bias voltages and the corresponding shift of the energy states. Here, E_{C} denotes the conduction band, E_{V} the valence band and E_{F} the Fermi energy [43].

3.4 Leakage Current of a p-n Junction

A current flowing through a material that is typically insulating is known as leakage current. In an ideal p-n diode, it is assumed that charge carrier generation and recombination within the depletion region are negligible. However, a measurable leakage current I_{ideal} originates from the diffusion of minority charge carriers outside the depletion region and depends exponentially on the applied external voltage. This behaviour is described by the Shockley diode equation:

$$I_{\mathrm{ideal}} = I_{\mathrm{S}} \left(\exp \frac{eV_{\mathrm{ext}}}{k_{\mathrm{B}}T} - 1 \right), \tag{3.2}$$

where I_{S} is the reverse bias saturation current. The current-voltage (IV) characteristic of a p-n junction is shown in Figure 3.4. In forward bias, the leakage current increases exponentially with rising voltage. In reverse bias, the leakage current remains nearly constant until the breakdown voltage V_{Break} is reached. Beyond this point, the current rises rapidly due to the acceleration of charge carriers in the electric field. These carriers gain sufficient energy to ionise additional atoms, initiating an avalanche process that can cause large currents and potentially damage the diode.

In real p-n diodes, leakage current is also generated within the bulk and on the surface of the material. Bulk leakage current arises from the thermal excitation of electrons, known as the generation current I_{gen}. This generation current depends on the depleted volume V_{dep} and the concentration of impurities that serve as generation and recombination centres, often introduced through radiation exposure.

Chapter 3.7 provides a more detailed discussion of radiation-induced damage in silicon sensors. The generation current is given by:

$$I_{\mathrm{gen}} = eV_{\mathrm{dep}} \frac{n_{\mathrm{i}}}{\tau_{\mathrm{g}}} = eAd \frac{n_{\mathrm{i}}}{\tau_{\mathrm{g}}} \approx eA \frac{n_{\mathrm{i}}}{\tau_{\mathrm{g}}} \sqrt{V_{\mathrm{ext}}}\,, \tag{3.3}$$

where A is the area under the electrode, d is the depth of the depletion region, n_{i} is the intrinsic carrier density, and τ_{g} is the carrier generation lifetime, defined as the average time it takes for thermally generated electron-hole pairs to recombine. The generation current can also be expressed as a function of temperature T:

$$I_{\mathrm{gen}} = T^2 \exp - \frac{E_{\mathrm{a}}}{2k_{\mathrm{B}}T}, \tag{3.4}$$

where k_{B} is the Boltzmann constant, and $E_{\mathrm{a}} \approx 1.21\,\mathrm{eV}$ represents the activation energy required to move a charge carrier from the valence band to the conduction band.

Surface leakage current is primarily caused by damage to the surface, often introduced during fabrication or handling. This current is strongly dependent on the geometry of the device and scales linearly with the applied external voltage. However, bulk leakage current typically dominates the overall leakage behaviour [43].
In semiconductor detectors, minimising leakage current is crucial, as it constitutes one of the major sources of noise in the measurement process and contributes to heat generation in the sensor.

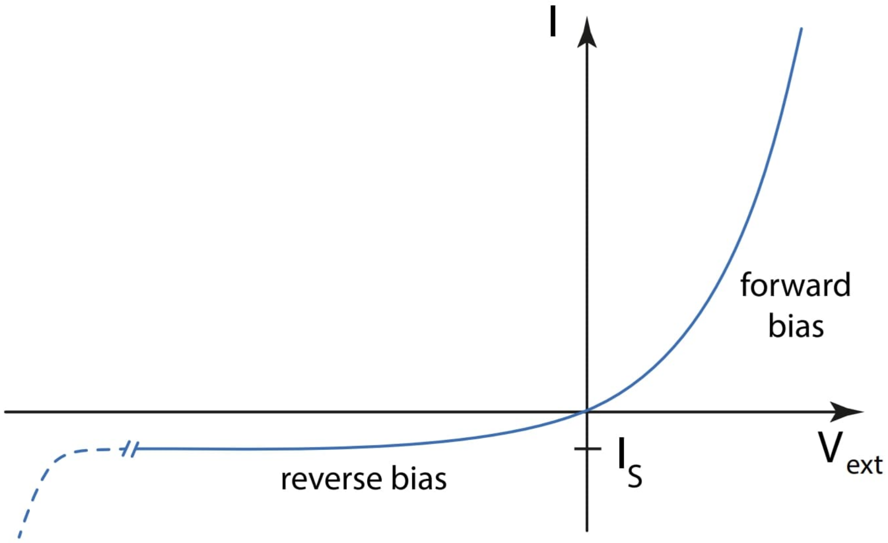

Figure 3.4: Current-voltage characteristic of an ideal diode for forward and reverse bias operation. The dashed line describes the breakdown of the diode and I_S the saturation current [43].

3.5 Capacitance of a p-n Junction

The depletion region of a p-n junction exhibits a capacitance C, which can be approximated by modelling the junction as a parallel plate capacitor with a dielectric material:

$$C = \epsilon_0 \epsilon_\mathrm{r} \frac{A}{d_\mathrm{dep}} \,, \tag{3.5}$$

where ϵ_0 is the permittivity of free space, ϵ_r is the relative permittivity of the dielectric, A is the area of the plates, and d_dep is the depth of the depletion zone [43].
The capacitance of a p-n junction decreases as the depletion volume increases. Therefore, the depletion voltage of a sensor can be determined by measuring the capacitance as

a function of the applied external voltage, where $V_{\text{ext}} \propto 1/C^2$. When full depletion is reached, the capacitance of the depletion region stabilises, as the depletion depth no longer increases with further bias voltage.

3.6 Energy Deposition of Ionising Particles in Silicon Sensors

Silicon detectors used in high-energy particle physics measure signals created by the ionisation of atoms by charged particles. This is accomplished by operating a p-n junction in reverse bias, which creates a sufficiently large depletion region. Charged particles that enter the depletion region ionise atoms via electromagnetic interactions. The electron-hole pairs generated by this process do not recombine due to the presence of the electric field and instead drift towards the electrodes.

The number of electron-hole pairs generated depends on the energy deposited by the particle in the sensor material. The energy deposited by an ionising particle in the sensor depends on several factors, including the particle's properties and the material of the sensor. Low-energy particles predominantly deposit energy through ionisation and excitation of atoms via inelastic collisions, while bremsstrahlung becomes the dominant energy loss mechanism at higher energies. For relativistic heavy charged particles, the mean energy loss per unit distance travelled in the material is described by the Bethe-Bloch formula [44]:

$$-\left\langle \frac{dE}{dx} \right\rangle = \frac{4\pi}{m_e c^2} \left(\frac{e^2}{4\pi\epsilon_0} \right)^2 \frac{nz^2}{\beta^2} \left[\frac{1}{2} \ln \left(\frac{2m_e c^2 \beta^2}{I(1-\beta^2)} \right) - \beta^2 - \frac{\delta(\gamma\beta)}{2} - \frac{C(\beta\gamma, I)}{Z} \right], \quad (3.6)$$

where m_e is the electron mass, Z is the atomic number, γ is the Lorentz factor, n is the electron density, z is the charge of the particle, I is the mean excitation potential, and $\beta = v/c$ is the ratio of the relativistic velocity v to the speed of light c. Deviations from the energy loss predicted by the Bethe-Bloch formula become significant at both high and low energies. These deviations are accounted for by the density correction $\delta(\gamma\beta)$ and the shell correction $C(\beta\gamma, I)/Z$, respectively. Figure 3.5a illustrates the mean energy loss of pions in silicon over a wide energy range, as an example.

Equation 3.6 is valid only for particles that are much heavier than the electron and positron, for which additional corrections must be considered. Due to their low mass, energy losses from bremsstrahlung are significantly larger for electrons and positrons, and deflection effects become more pronounced. Moreover, annihilation effects of traversing positrons with shell electrons, as well as the indistinguishability of a traversing electron from shell electrons, must also be accounted for.

Particles with an energy of approximately $\gamma\beta \approx 3$ deposit the least amount of energy and are thus referred to as minimum ionising particles (MIPs). Since high-energy silicon detectors are typically designed to detect a broad range of charged particles, MIPs are often used to test sensor performance due to their relatively low signal generation.
With the Bethe-Bloch formula, only the mean deposited energy and, consequently, the mean number of generated electron-hole pairs are determined. The fluctuations in the number of electron-hole pairs generated by a single ionising particle differ between thick and thin sensors and are described by the Gaussian [45] and Landau [46] distributions, respectively:

$$f(x) = \frac{1}{\sigma\sqrt{2\pi}} e^{-\frac{(x-\mu)^2}{2\sigma^2}} \tag{3.7}$$

$$g(x) = \frac{1}{\pi} \int_0^\infty e^{-t\log(t)-xt} \sin(\pi t)\,\mathrm{d}t\,, \tag{3.8}$$

where $f(x)$ and $g(x)$ are the probability density functions (PDFs) of the two distributions, μ is the mean value, and σ is the standard deviation. The peak of the Landau distribution represents the most probable value, which differs from its undefined mean due to the distribution's asymmetric shape. Both distributions are shown in Figure 3.5b. The long tail of the Landau distribution, characteristic of energy deposition by ionising particles, arises from so-called δ-electrons, which are ejected with enough energy to ionise additional atoms. For instance, approximately 32,000 electron-hole pairs are produced by a MIP traversing 300 µm of silicon at 300 K [43].

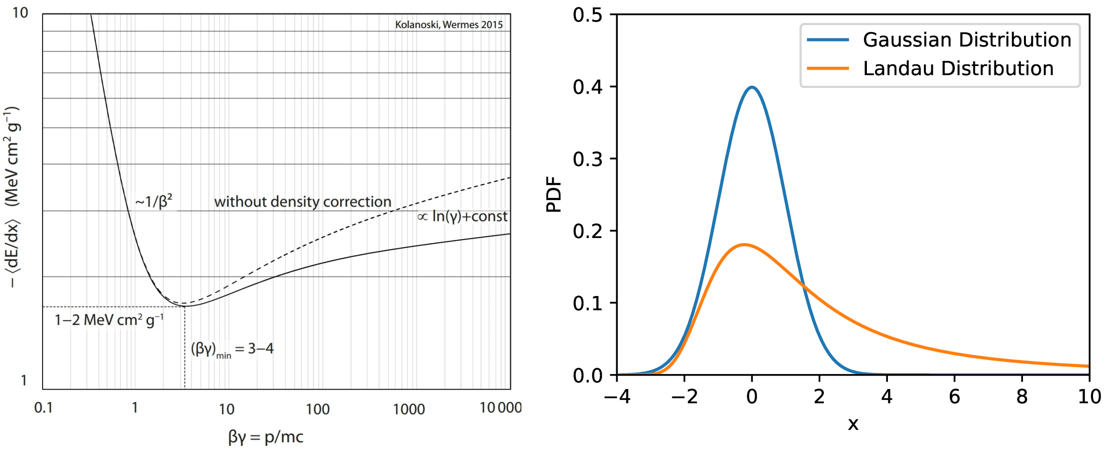

(a) **(b)**

Figure 3.5: a) Mean energy loss of charged pions in silicon according to the Bethe-Bloch formula with and without the density correction [43]. b) Computed Gaussian and Landau distributions using the equations 3.7 and 3.8 with $\mu = 0$ and $\sigma = 1$

3.7 Radiation Damage in Silicon Sensors

The operation of silicon sensors in environments with high particle fluxes, such as the LHC, leads to degradation of the sensor material due to radiation-induced damage. The extent of this damage depends on both the number of particles traversing the sensor and the type of particles, as different particles interact with the sensor material in distinct ways. Ionising energy loss processes are largely reversible and primarily contribute to surface damage. The surface damage is mostly relevant for the readout electronics of detector modules, due to the degradation of transistor performance in the CMOS circuits. The dominant damage to the sensor bulk from non-ionising particle interactions, such as the displacement of lattice atoms, can be approximated using the non-ionising energy loss scaling hypothesis, which aligns well with experimental irradiation data [47]. This hypothesis posits that the extent of radiation damage caused by a particle is proportional to the non-ionising energy it deposits, independent of the particle's properties. This allows radiation damage from different particles to be scaled for comparison. The standard convention scales damage to the equivalent damage caused by 1 MeV neutrons ($1\,\mathrm{n_{eq}}$). The total radiation exposure is quantified by the fluence, defined as the number of neutron equivalents per unit area, typically expressed in $1\,\mathrm{n_{eq}/cm^2}$.

Various types of defects are introduced into the silicon lattice upon irradiation, such as displaced lattice atoms creating vacancies and interstitial atoms. Figure 3.6 illustrates some of the defects introduced by particle radiation. Defects are often unstable and may either recombine and dissolve or migrate through the lattice, where they can form stable complexes with impurities. The process of annealing, which occurs when the material is heated to a specific temperature, can help repair some of these radiation-induced defects. During annealing, the migration of atoms can lead to the recombination of vacancies and interstitials, reducing the overall defect density and restoring the material's electrical properties. However, excessive annealing can cause further sensor damage, such as the formation of new defect complexes, which negatively affect sensor performance. For this reason, it is essential to cool sensors during and after irradiation to prevent uncontrolled annealing and minimise long-term damage.

Similar to introduced dopants, defects affect the band structure of the semiconductor and alter its electrical properties. This leads to several unwanted effects caused by the newly introduced energy levels. The leakage current increases due to a higher probability of electron-hole pair generation. Defects can also act as recombination centres for electron-hole pairs or as traps and scattering centres for charge carriers, thereby impairing charge collection efficiency. Additionally, dopants may be displaced from the crystal lattice or become bound in defect complexes, resulting in changes to the effective doping concentration. This effect predominantly affects n-type dopants, such as phosphorus, causing a shift in n-type material toward p-type doping. The shift is further enhanced by defects that capture electrons from the conduction band, effectively acting as

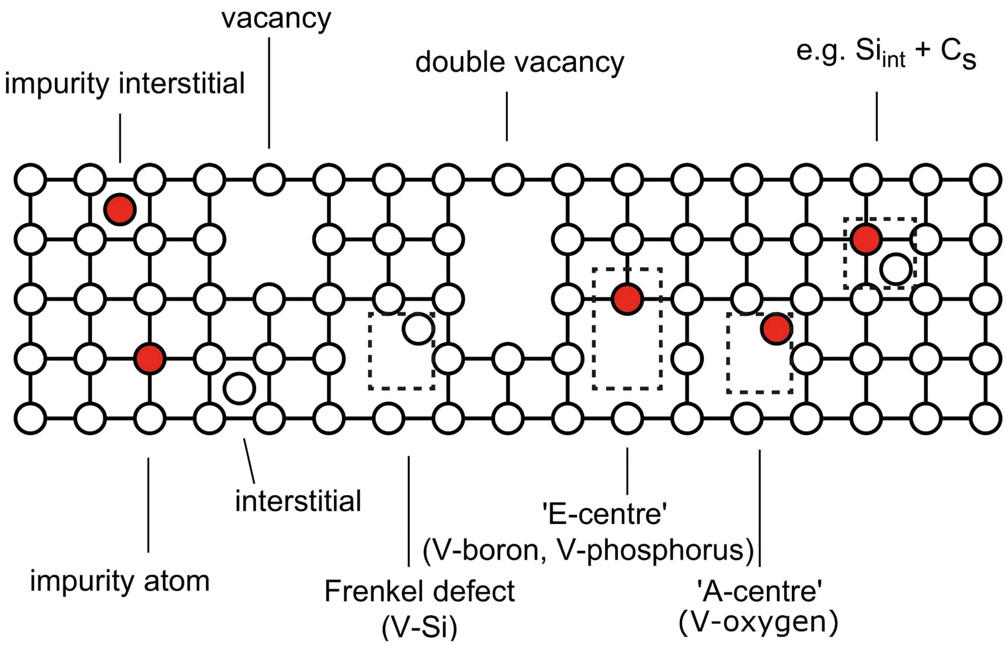

Figure 3.6: Illustration of various types of defects in a doped silicon lattice. The red circles indicate impurities, the V denotes vacancies and C_S denotes a carbon atom impurity [43] (modified).

acceptors. As a result, at high fluences, type inversion can occur, where n-type material transforms into p-type material. This type inversion alters the required depletion voltage, as it is directly proportional to the effective doping concentration. Figure 3.7 illustrates this phenomenon, which can occur at fluences as low as $10^{13}\,\mathrm{n_{eq}/cm^2}$.

In experiments at the LHC, such as ATLAS or CMS, sensors near the beamline are expected to be exposed to fluences on the order of $10^{15}\,\mathrm{n_{eq}/cm^2}$. Since type inversion at these fluences is unavoidable, most silicon sensors for the high-luminosity phase of the LHC are designed as n^+-in-p sensors. The p-type bulk generally does not undergo type inversion, making these sensors more resistant to radiation damage.

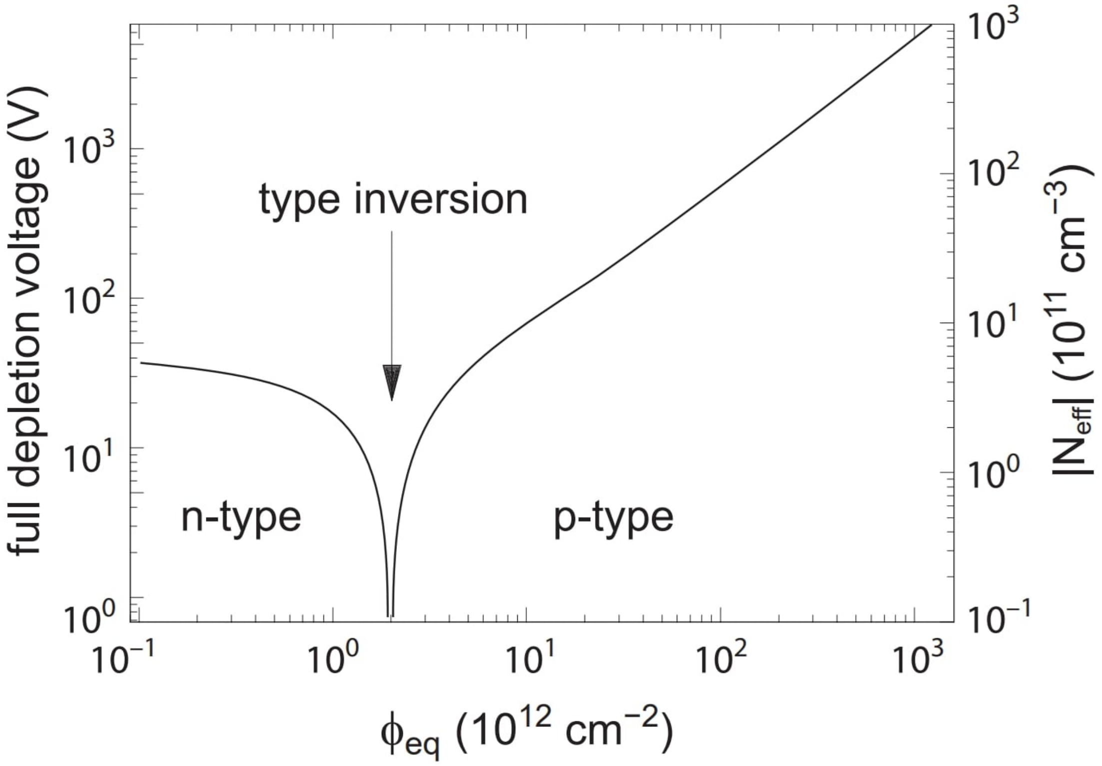

Figure 3.7: Type inversion from p-type to n-type material. The effective doping concentration and the depletion voltage are shown as a function of the fluence [43].

4 Hybrid Pixel Modules

There are several designs for detecting particles with silicon detectors, each offering distinct advantages and trade-offs. Pixel detectors provide superior radiation hardness and spatial resolution for hit position measurements compared to strip detectors, but at higher manufacturing costs. This advantage is attributed to the smaller segmented areas on the silicon sensor.

Additionally, there are two fundamentally different designs for the readout electronics of pixel detectors: monolithic and hybrid. Monolithic detectors integrate the sensitive sensor volume and either part or all of the readout electronics into a single piece of silicon. They offer high granularity, approximately ($20\,\mu\text{m} \times 20\,\mu\text{m}$), and small thicknesses of around $50\,\mu\text{m}$. However, the large LHC experiments ATLAS and CMS have relied exclusively on hybrid detectors for the first three operational phases as well as for the HL-LHC phase [48, 49]. This preference is due to the significantly better performance of hybrid pixel detectors in environments with high particle fluxes and intense radiation [50].

This chapter provides an introduction to hybrid pixel modules, as all devices tested in this thesis belong to this category.

4.1 Architecture of Hybrid Modules

Hybrid detectors are composed of a separately manufactured sensor and readout chip. The pixel cells on the sensor are connected to corresponding channels on one or more readout chips using small conducting solder balls, referred to as bump bonds, through a process known as bump bonding. This design allows for separate optimisation of the active (readout) and passive (sensor) components, ensuring superior performance tailored to specific requirements. However, the material budget is significantly higher compared to monolithic detectors because particles experience multiple scattering in the readout chip and the support structure. Additionally, manufacturing costs are expected to be generally greater due to the complex assembly process, particularly the bump bonding step. Figures 4.1a and 4.1b illustrate a single pixel cell, including the readout chip of a hybrid detector and a complete hybrid pixel matrix, respectively.

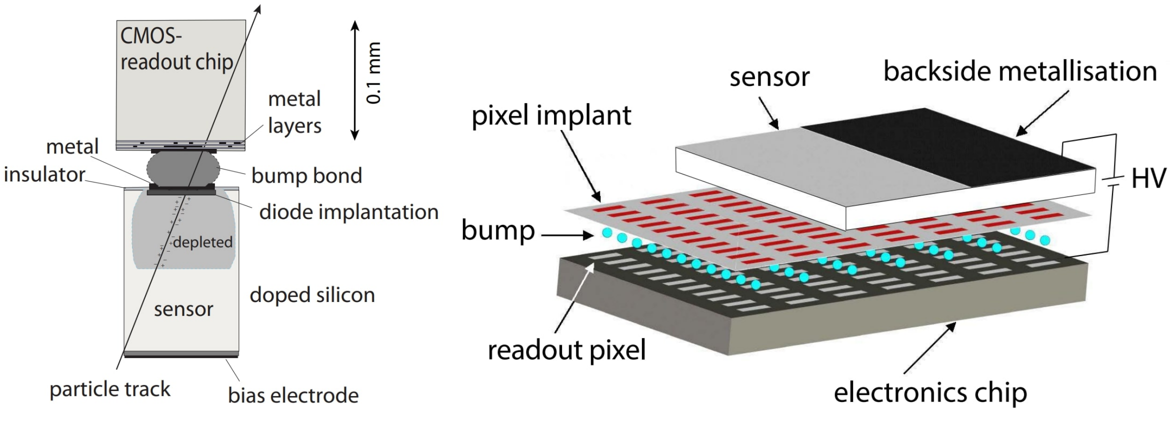

(a) **(b)**

Figure 4.1: a) Illustration of a hybrid pixel cell and a traversing ionising particle. b) Layout of a hybrid pixel matrix with the pixel implants shown separately from the sensor for better visualisation [43].

4.2 The Sensor of Hybrid Modules

The silicon bulk is typically a weakly doped region where charge carriers are generated by ionising particles traversing the material. It contains multiple highly doped electrodes that create the depletion zone under an applied external voltage and collect the generated charge carriers. N-type implants are preferred for charge collection because electrons, having higher mobility than holes, lead to faster signal generation compared to p-type implants. The higher mobility also decreases the trapping probability of the electrons, which makes the sensor more radiation hard.

In the first three phases of the ATLAS and CMS experiments, most silicon sensors were of the planar n^+-in-n type due to their solid radiation hardness and easier manufacturing at the time. However, extensive research on n^+-in-p sensors has demonstrated significant advantages for the High-Luminosity phase of the LHC. Unlike n^+-in-n sensors, n^+-in-p sensors do not undergo type inversion in the p-type bulk, allowing for simpler one-sided processing and reduced production costs. This is particularly beneficial for experiments like the ATLAS ITk, which require large-area hybrid pixel detectors. Additionally, n^+-in-p sensors have shown adequate radiation hardness for the HL-LHC environment [51].
In n^+-in-n sensors, double-sided wafer processing is required because the depletion zone can expand either from the n^+ implants on the front side or the single p^+ implant on the back side. Guard rings are implemented on one side of the sensor to manage the voltage drop at the edges.

To supply external voltage to the pixel cells before the bump bonding process, several different methods are used. A bias rail consisting of metal traces connects the bias grid ring and the pixels through a bias dot. All pixels are brought to the same potential using the punch-through effect. When the applied voltage reaches the punch-through voltage V_{PT}, the depletion zone around the bias dot expands laterally until it merges with the depletion zone of the pixel implant, establishing conductive contact. This way, complex metal routing on top of the pixels can be prevented

Two other bias structures are also used, depending on the module vendor: A thin polysilicon layer is deposited right above the silicon substrate and provides a continuous resistive path connecting the pixel electrodes to a bias voltage.

Alternatively, a temporary metal layer is applied to the wafers during fabrication, covering the pixel array to provide an electrical path for biasing during testing and initial measurements. After bump bonding, the pixels are biased through the readout channel of the FE.

There are two major sensor designs, differentiated by the structure of their electrodes: planar and 3D sensors, which are illustrated in Figures 4.2a and 4.2b, respectively. The previously described doping structures apply to planar sensors, which consist of highly doped silicon layers on both the top and bottom sides of the silicon bulk. In these sensors, generated electron-hole pairs drift toward opposite electrodes, with the sensor thickness being the maximum distance the charge carriers must travel before collection. Planar silicon sensors are well understood and are widely used in modern particle detectors.

The newer 3D silicon sensor design utilises n^+ and p^+ doped electrodes in the form of pillars etched directly into the silicon. This design enables much shorter distances between the bias and charge collection electrodes, resulting in a lower depletion voltage, reduced leakage current, and faster charge carrier drift times. These advantages make 3D sensors more radiation-hard compared to planar sensors, making them especially suitable for high radiation environments. However, due to the complex processing required, 3D sensors are more expensive to produce, which limits their application to smaller areas. As a result, 3D sensors are used in the ATLAS experiment only in the innermost layer, the Insertable B-Layer (IBL), where the required area is relatively small and the sensors must withstand high radiation fluences. The 3D sensor technology will also be implemented in the innermost layer of the ATLAS ITk detector.

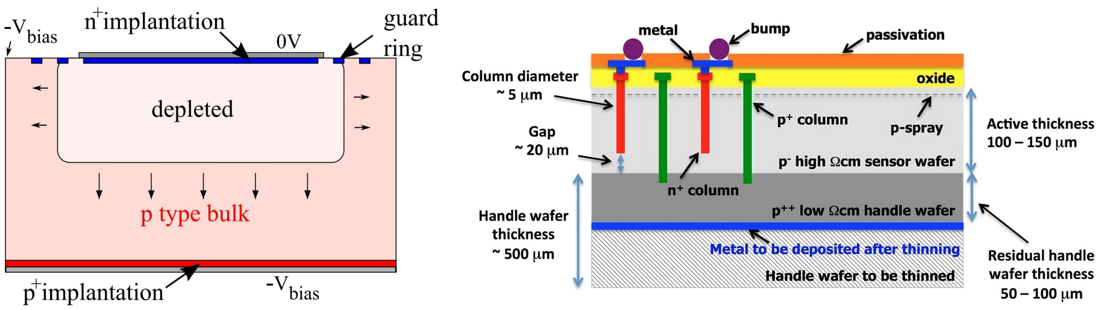

(a) **(b)**

Figure 4.2: Illustration of a planar (a) and a 3D (b) sensor cross section [52, 53].

4.3 The Readout Chip of Hybrid Modules

The signal generated at the electrodes of a hybrid module undergoes additional processing by a readout chip, where it is amplified, discriminated, and digitised. Signal amplification is essential to enhance the signal-to-noise ratio. To further reduce noise, readout chips employ comparators to set a charge threshold, ensuring that only signals above this threshold are measured.

The time over threshold (TOT) of a signal can be measured by the chip to estimate the amount of energy deposited by ionising particles. To ensure accurate operation of the readout electronics for each pixel, the FE must undergo a tuning procedure. The details of this tuning process are described in Section 4.4.

After the measured data is processed by the analogue part of the readout, it is digitised using an analogue-to-digital converter (ADC), which facilitates easier processing, transmission, and analysis of data.

Currently, the hybrid modules of the Inner Detector use the FE-I3 readout chip [54], with its successor, the FE-I4 [55], used for the IBL. For the ITk upgrade, the ITkPixV2 [34] will be employed, which is optimised to handle the more challenging conditions near the beamline of the HL-LHC. All the hybrid pixel modules investigated in this thesis are equipped with the ATLAS ITkPixV1.1 FE, which serves as the pre-production version of the final design readout chip. The ITkPixV1.1 chip is described in more detail in Chapter 2.4.2.

4.4 Tuning of Hybrid Pixel Detectors

Ideally, all pixel readout channels of a hybrid pixel module should respond identically to an incoming signal in terms of amplification, discrimination, and TOT response. However, small differences between the individual channels of the readout chip are inevitable due to its inherent complexity and sensitivity. These differences are further amplified when the readout chip is exposed to radiation.

To ensure proper calibration of the pixels during operation, the individual channels of the readout chip are tuned. This tuning is achieved by adjusting both global and local parameters, which affect all pixels and individual pixels, respectively. The most significant of these parameters are the global and local thresholds, which determine the charge threshold at which the sensor registers a signal. The global threshold is controlled by the GDAC register and influences the mean threshold across all pixels. Additionally, the local threshold is fine-tuned via the comparators in each readout channel, with the adjustment managed by the TDAC register. Ideally, the threshold for all pixels is set to the expected value. However, the limited number of available register entries restricts local tuning, resulting in a threshold distribution that typically follows a Gaussian shape, with a preference for a small standard deviation. A notable effect of an induced charge signal is the rising flank that reaches its peak after a time that is independent of the magnitude of the charge signal. As a result, larger charge signals rise faster and cross the threshold earlier, increasing the time over threshold, which is called timewalk.

Similarly, global and local parameters are used to tune the TOT response. This is done by adjusting the slope of the falling edge of the signal. Local tuning is implemented through a feedback current for the amplifiers, which is controlled by the FDAC register. As with the threshold, the TOT distribution also exhibits a Gaussian shape after successful tuning, due to the constraints of local tuning.

To ensure accurate calibration, a well-defined amount of charge must be injected into the pixels. This is achieved by directly injecting charge into the readout system through an injection capacitance. The influence of tuning on both the threshold and TOT is schematically shown for two charge injections in Figure 4.3.

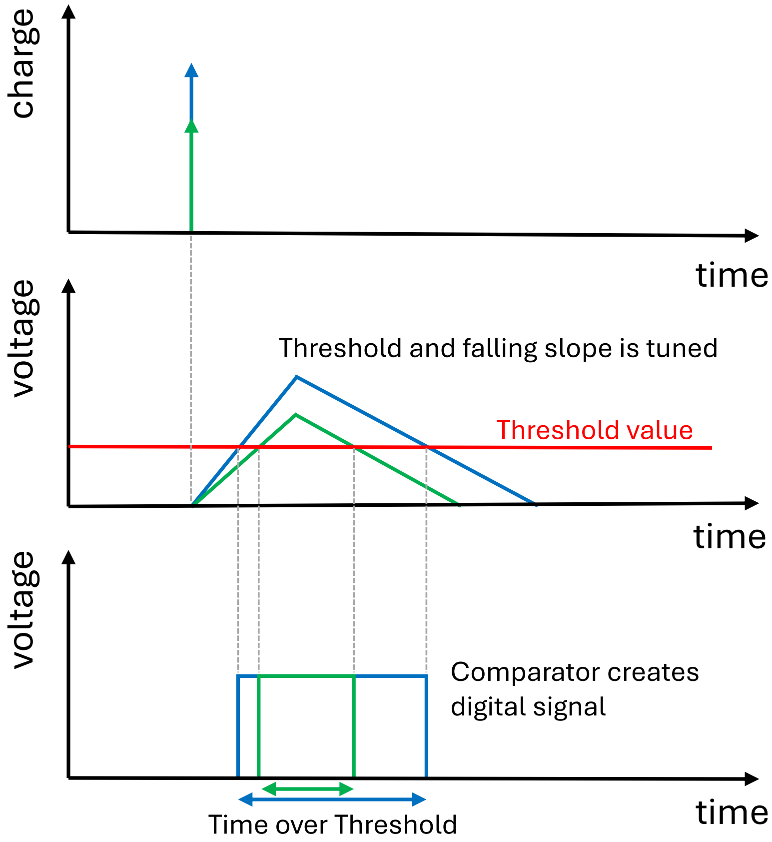

Figure 4.3: Depiction of initial charge signals and the corresponding processed signals which depend on the tuning configuration.

Several scans can be performed to evaluate the tuning results and, more generally, the entire charge collection and readout process. The tuning and scan options are highly dependent on the software used, as hybrid pixel sensors have different readout system designs, and most software is developed to support only a limited number of designs. Notably, the STControl framework for the USBpix readout system [56] is commonly used to tune the FE-I4. For the RD53A and ATLAS ITkPix readout chips, the BDAQ [57] and YARR [58] frameworks are commonly employed in testing setups. The FELIX [59] framework is the readout system for the final design FE and it will be used in the data acquisition pipeline of the ATLAS experiment.

5 Investigation of ITk Pixel Pre-Production Test Structures

The planar pixel sensors for the ITk upgrade are manufactured by the vendors Hamamatsu Photonics (HPK) [60], Fondazione Bruno Kessler (FBK) [61], and Micron [62], selected through a market survey campaign [63]. During the pre-production phase, these vendors produce a limited number of test structures (TS), allowing the ITk collaboration to investigate their performance. This early evaluation helps identify potential sensor issues before large-scale production begins.

The vendors conduct an initial investigation of the TS by measuring key electrical characteristics, including current-voltage (IV), current-time (It), and capacitance-voltage (CV) responses of sensor tiles and diodes. This process is referred to as quality control. In parallel, ITk testing sites perform similar measurements, along with additional optional tests such as inter-pixel resistance and charge collection efficiency studies. These extended investigations fall under the category of quality assurance (QA). QA measurements were carried out at several institutes, including IJCLab, KEK, MPP, TU Dortmund, the University of Göttingen, and Lancaster University.

As part of this thesis, the IV, It, and CV characteristics of several ITk TS were measured at TU Dortmund and the corresponding results are presented in this chapter.

5.1 ITk Pre-Production Test Structures

At TU Dortmund, several diodes and sensor tiles from unirradiated HPK and irradiated Micron test structures were investigated. In this context, a test structure refers to a diced segment of the full wafer. The different test structures, designated TS1, TS2, and TS3 from an HPK wafer, are shown in Figure 5.1a, while a close-up image of TS1 is presented in Figure 5.1b. The larger diode has an area of $10 \times 5\,\mathrm{mm}^2$, whereas the two smaller diodes measure $5 \times 5\,\mathrm{mm}^2$ each. Throughout this thesis, the HPK TS and diodes are referred to by their respective numbers, as depicted in the Figures 5.1a and 5.1b.

The diodes on the TS serve as representations of the pixel implants within the sensor, enabling the characterisation of the bare sensor. Additionally, the TS contain other elements designed for further investigations, such as inter-pixel capacitance structures, mini-sensors, and strips. However, these structures were not examined within the scope of this thesis.

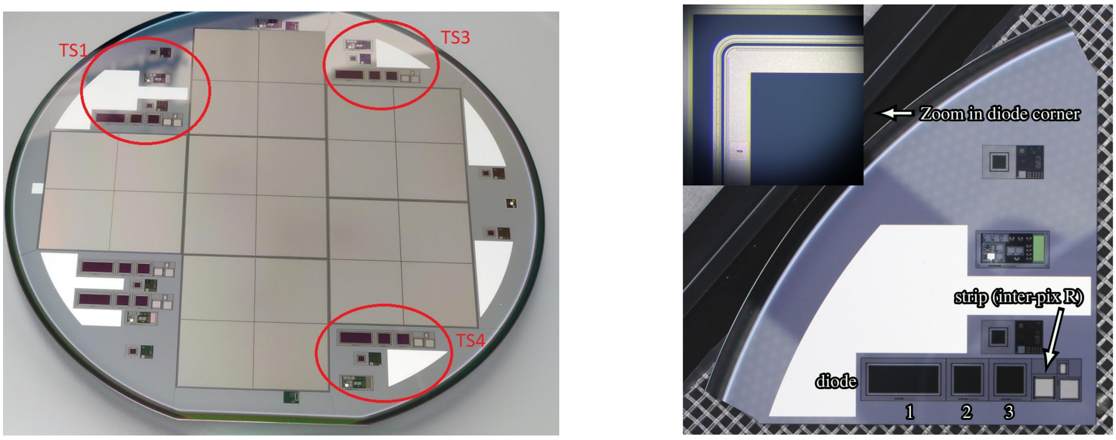

(a) (b)

Figure 5.1: a) Unirradiated HPK pre-production wafer. The circled areas indicate the different parts of the wafer with the TS that were investigated [64]. b) Close-up image of an HPK TS, including several diodes and structures for various measurements. In the upper left corner is an image of the diodes' bias and guard rings under a microscope [65].

Figure 5.2a illustrates the layout of the 150 µm Micron TS, highlighting its named substructures, while Figure 5.2b shows a close-up picture of a quad sensor tile. The naming convention used in the Micron wafer schematic is retained throughout this chapter to describe these substructures. The investigated structures, the quad TS and the MSLTSF, have areas of 16 cm^2 and 4.25 cm^2, respectively. The Micron TS, investigated in this thesis, were irradiated to fluences of $2 \times 10^{15}\ \mathrm{n_{eq}/cm^2}$ and $5 \times 10^{15}\ \mathrm{n_{eq}/cm^2}$ and annealed likely until the saturation of the long-term annealing effects.

Unlike fully processed pixel modules, the TS utilise bias pads, which are accessible by probe needles to supply the sensor with a bias voltage. The various bias structures are described in more detail in Section 4.2. A summary of the different TS, including their active thicknesses and biasing mechanisms, is presented in Table 5.1. In this thesis, TS from HPK and Micron were analysed.

Table 5.1: List of the different ITk pre-production TS including the vendor, the bias structure and the active thickness.

Vendor	Active Thickness	Bias Structure
HPK	150 µm	Poly-Silicon
FBK	150 µm	Temporary Metal
Micron	150 µm, 100 µm	Punch-Through

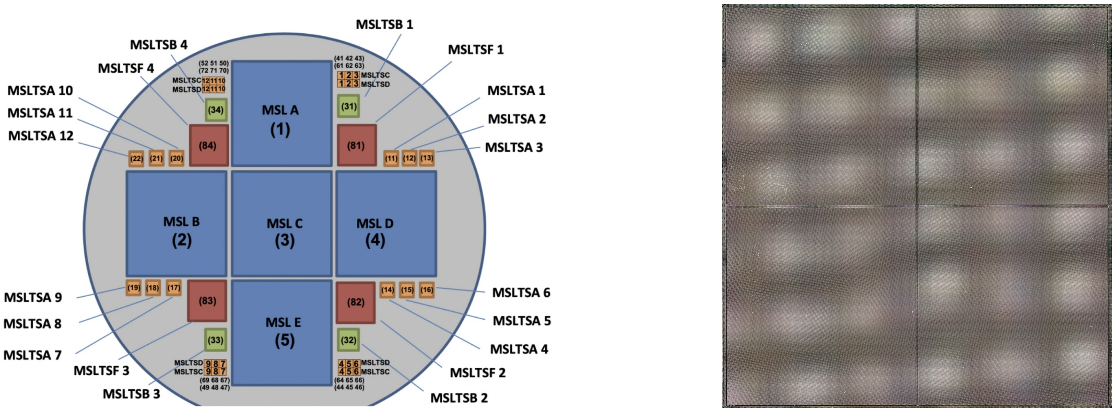

(a) **(b)**

Figure 5.2: a): Schematic of the Micron TS layout. The large blue tiles in the centre are the quad sensors and the small tiles are primarily diodes [66]. b) Close-up image of a Micron quad sensor tile.

5.2 QA Measurements

A brief introduction to the current-voltage and capacitance-voltage characteristics of a diode is provided in Sections 3.4 and 3.5. Measurements for unirradiated and irradiated TS were conducted at $(20 \pm 2)\,°\mathrm{C}$ (room temperature) and $(-25 \pm 1)\,°\mathrm{C}$, respectively. The QA measurements performed in this thesis include IV, CV, and It measurements, which are described in the following sections.

IV Measurement

During the operation of the ATLAS ITk, sensors degrade due to radiation exposure. To ensure full depletion, the applied bias voltage V_b is increased over time. For planar sensors, the pixel electrode structure is comparable to a diode, meaning that at a sufficiently high voltage V_bd, breakdown occurs, rendering the sensor unusable. Breakdown is defined here as an increase in the leakage current I_leak of more than $20\,\%$ for a $5\,\mathrm{V}$ increase in bias voltage. The purpose of IV measurements on diode TS is to confirm that the sensor operates reliably within a sufficiently high voltage range. Therefore, the leakage current must remain low across the applied voltages. The investigated voltage range, along with the acceptable leakage current and breakdown voltage thresholds, depends on the received fluence of the TS. Since the leakage current scales with the diode area, all leakage current values are normalised to the diode area.

Table 5.2 outlines the requirements a sensor must meet to pass the QA measurements. Additionally, unirradiated sensors must not undergo breakdown within $70\,\mathrm{V}$ above the full depletion voltage V_fd.

Table 5.2: Summary of the IV measurement requirements. The voltage range and the maximum allowable leakage current for a sensor to pass the test depend on the irradiation and the active thickness of the sensor.

Irradiation	**Active Thickness**	Voltage range	Maximum I_{leak}
0	100 µm	200 V	$0.75\,\mu\text{A/cm}^2$ ($V_{\text{fd}} + 50\,\text{V}$)
$2 \times 10^{15}\ \text{n}_{\text{eq}}/\text{cm}^2$	100 µm	300 V	$20\,\mu\text{A/cm}^2$
$2 \times 10^{15}\ \text{n}_{\text{eq}}/\text{cm}^2$	150 µm	400 V	$25\,\mu\text{A/cm}^2$
$5 \times 10^{15}\ \text{n}_{\text{eq}}/\text{cm}^2$	100 µm	400 V	$35\,\mu\text{A/cm}^2$
$5 \times 10^{15}\ \text{n}_{\text{eq}}/\text{cm}^2$	150 µm	600 V	$45\,\mu\text{A/cm}^2$

It Measurement

For sensors, it is essential that the leakage current remains stable over extended periods of time. To assess this, the sensors are operated at their typical bias voltage for 48 hours at low temperatures. Leakage current measurements are taken every 10 minutes, excluding the first 10 minutes during the voltage ramp-up, since the changing voltage may induce unwanted effects in the sensor, potentially causing increased instability in the leakage current. Throughout the measurement period, the leakage current must remain within ±25 % of its mean value for the diode TS to pass the test. The maximum fluctuation, I_{mf}, is defined as:

$$I_{\text{mf}} = \frac{I_{\text{max}} - I_{\text{min}}}{I_{\text{mean}}}. \tag{5.1}$$

CV Measurement

To optimally operate the ITk modules, it is crucial to measure their depletion voltage accurately. The depletion voltage can be determined from the saturation of $1/C^2$ using Equation 3.5. This value is measured in 5 V steps to precisely identify the crossing point between the linear and constant regions of the curve.

An unirradiated sensor is considered acceptable if the depletion voltage, V_{d}, is below 60 V for sensor thicknesses of 100 µm and below 100 V for sensor thicknesses of 150 µm. No specific depletion voltage is defined for irradiated sensors. Therefore, the results are evaluated based on the probed voltage range during IV measurements of the irradiated sensors.

5.3 QA Measurement Setup

To ensure the proper measurement conditions described in Section 5.2, a wafer prober is utilised, specifically designed for the precise probing of small wafer structures in a controlled environment. The wafers are placed on a gold chuck, which creates a vacuum through small holes, securely holding them in place. During measurement, the wafer is shielded from light. Inside the wafer prober, temperatures can be controlled within a range of $-60\,^{\circ}\mathrm{C}$ to $300\,^{\circ}\mathrm{C}$ using a chiller with water as a coolant. Small tungsten needles are used to probe the TS and can be positioned with high precision using an integrated microscope. These needles are connected to external electronic devices that supply the required voltages and currents for the QA measurements. Figure 5.3a shows the wafer prober used for all QA measurements presented in this thesis.

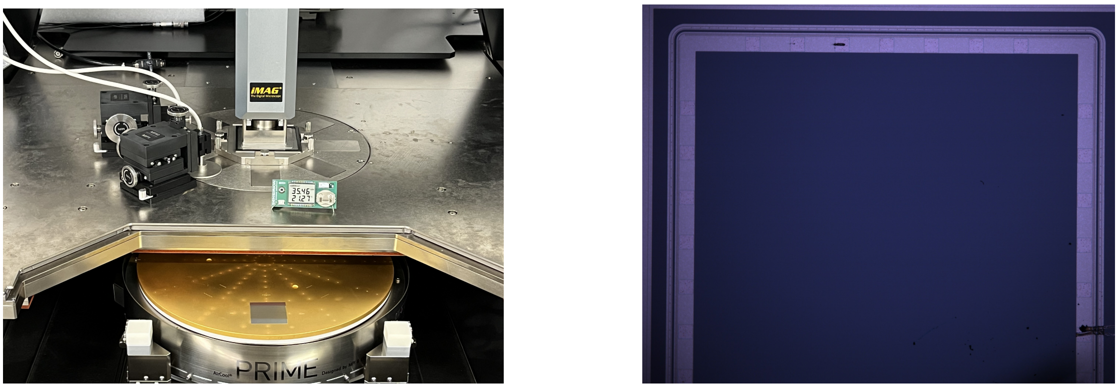

(a) **(b)**

Figure 5.3: a) Photo of a quad TS placed on the chuck of the wafer prober used for the QA measurements. b) Close-up photo of the 10 mm diode under the microscope of the wafer prober.

To perform the IV measurements, a Keithley 2410 [67] power supply was connected to the needle prober. The device is connected to the network via GPIB and is controlled remotely using the E4control software [68]. This software allows for the operation and configuration of the measurement setup, including the specification of the voltage range V_{range}, voltage steps V_{step}, the number of measurements per voltage point n_{meas}, and the delay time t_{delay} between the voltage change and the current measurement. A larger bias voltage step size of 10 V was taken for the irradiated modules due to the broader range of applied bias voltages.

The It measurement was performed in a similar manner, with adjusted configuration parameters. Table 5.3 summarises the configuration parameters used for the IV, CV, and It measurements presented in this thesis. The individual measurement parameters for each investigated TS are detailed in Section 5.4.

Table 5.3: Configuration parameters of the Keithley 2410 and the wafer prober for the IV, CV and It measurements. Different parameter values were chosen for the different TS based on their properties.

Configuration	IV Measurement	CV Measurement	It Measurement
V_{range}	$200 - 600\,\text{V}$	$100 - 300\,\text{V}$	$100\,\text{V}/260\,\text{V}$
V_{step}	$5 - 10\,\text{V}$	$5\,\text{V}$	-
n_{meas}	10	10	1
t_{delay}	$3\,\text{s}$	$3\,\text{s}$	$30\,\text{s} - 600\,\text{s}$

For the CV measurement, the Keithley 2410 is used to apply a bias voltage to the bias pad of the diode, similar to the IV and It measurements. To calculate the capacitance of the depletion region, an Agilent 4284A LCR meter [69] is employed. This device determines the capacitance of electronic components by sending an AC signal and measuring the resulting changes in voltage and current. The AC signal is superimposed with the constant bias voltage using a bias box, allowing capacitance measurements at each voltage step. The amplitude and frequency of the AC voltage pulse can be adjusted. For the presented measurements, an amplitude of $1\,\text{V}$ and a frequency of $10\,\text{kHz}$ were chosen. Larger amplitudes would introduce greater disturbances to the bias voltage, while smaller values could reduce measurement precision due to a lower signal-to-noise ratio. Frequencies in the range of approximately $1 - 10\,\text{kHz}$ were found to be viable, avoiding unwanted leakage current effects and ensuring the signal stability of the LCR meter. Open corrections were applied to the measurements to account for parasitic capacitances in the measurement setup.

Figure 5.4 schematically depicts the configuration of the devices used for the CV measurement.

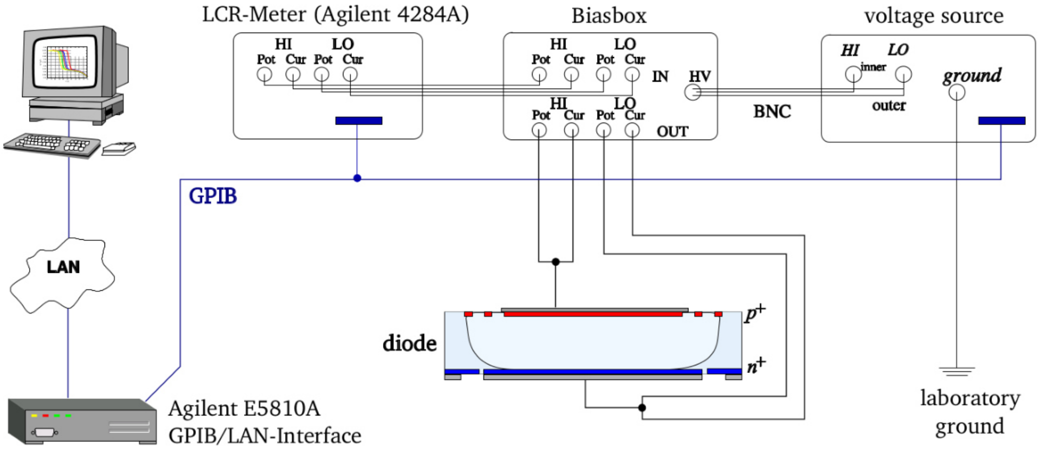

Figure 5.4: Schematic of a CV measurement setup including the devices used to generate the constant bias voltage, the AC voltage pulse and the bias box to superimpose the two voltages [52].

5.4 QA Measurement Results

The IV, CV, and It measurements were conducted on multiple diodes and quad TS from HPK and Micron. A comprehensive list of all tested components within the scope of this thesis is provided in Table 5.4. For the Micron TS, the primary focus was on the quad structures MSL A and MSL C. The smaller diodes on the MSL wafer were examined for their IV characteristics, with partial investigations of their CV properties.

The following subsection presents and discusses the results of the IV, CV, and It measurements separately.

Table 5.4: Summary of investigated TS, diodes and corresponding received fluences.

Vendor	Test structure	Substructure	Fluence
HPK	W1 TS1	$10 \times 5\,\mathrm{mm}^2$ (1. diode)	0
HPK	W1 TS1	$5 \times 5\,\mathrm{mm}^2$ (2. diode)	0
HPK	W1 TS1	$5 \times 5\,\mathrm{mm}^2$ (3. diode)	0
HPK	W1 TS3	$10 \times 5\,\mathrm{mm}^2$ (1. diode)	0
HPK	W1 TS3	$5 \times 5\,\mathrm{mm}^2$ (2. diode)	0
HPK	W1 TS3	$5 \times 5\,\mathrm{mm}^2$ (3. diode)	0
HPK	W1 TS4	$10 \times 5\,\mathrm{mm}^2$ (1. diode)	0
HPK	W1 TS4	$5 \times 5\,\mathrm{mm}^2$ (2. diode)	0
HPK	W1 TS4	$5 \times 5\,\mathrm{mm}^2$ (3. diode)	0
Micron	W0006	MSL A	$5 \times 10^{15}\,\mathrm{n_{eq}/cm^2}$
Micron	W0006	MSLTSF 1	$5 \times 10^{15}\,\mathrm{n_{eq}/cm^2}$
Micron	W0006	MSLTSF 2	$5 \times 10^{15}\,\mathrm{n_{eq}/cm^2}$
Micron	W0022	MSL C	$2 \times 10^{15}\,\mathrm{n_{eq}/cm^2}$
Micron	W0022	MSLTSF 1	$2 \times 10^{15}\,\mathrm{n_{eq}/cm^2}$
Micron	W0022	MSLTSF 2	$2 \times 10^{15}\,\mathrm{n_{eq}/cm^2}$

5.4.1 CV Measurements

The CV characteristics of the tested HPK TS are shown in Figure 5.5. All structures show the expected linear and constant part of a CV curve for diodes. The 10 mm diodes have a noticeably smaller $1/C^2$ proportionality due to their larger area in comparison to the 5 mm diodes.

Another increase of $1/C^2$ after the plateau for high bias voltages is not typically expected. This effect is attributed to further depletion of silicon in the TS. The slight discrepancy in the CV behaviour of the $5 \times 5\,\mathrm{mm}^2$ diodes of TS4 likely stems from minor production differences in those regions of the wafer as similar deviations were observed at the University of Göttingen for other HPK pre-production wafers [65].

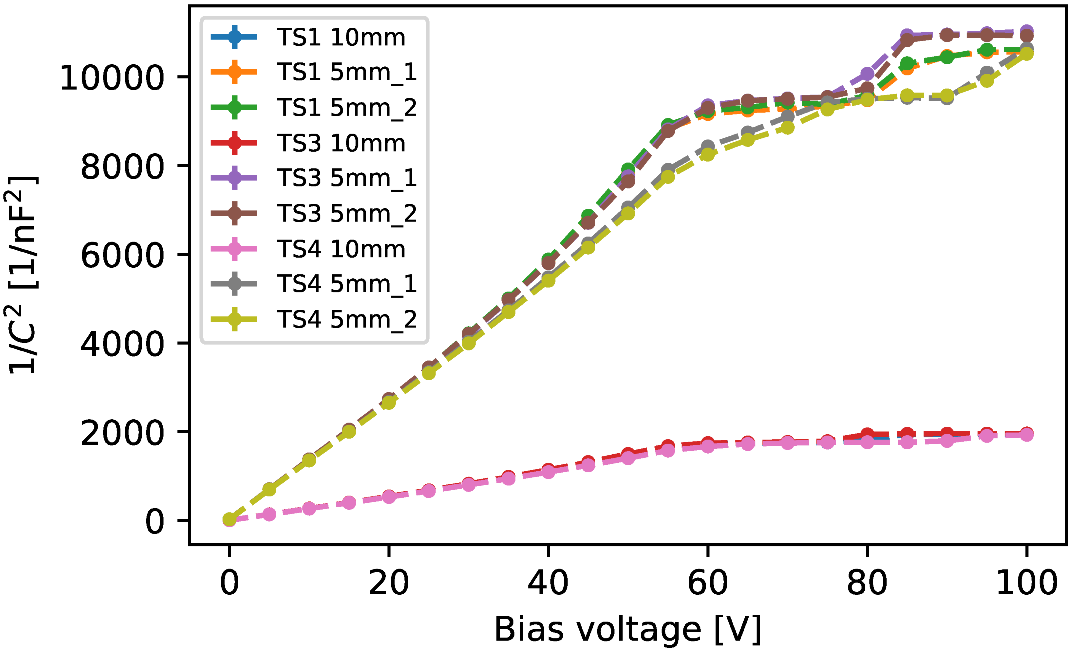

Figure 5.5: Capacitance of HPK TS as a function of the applied bias voltage.

To determine the depletion voltage of the sensors from their CV characteristics, a fit function is used to describe the transition from the linear to the constant proportionality of the $1/C^2$ term before and after full depletion. Rather than fitting separate lines to each section, a single fit function is utilised, incorporating a parameter x_0 that defines the optimal voltage at which the linear proportionality ends and the constant behaviour begins. For the irradiated structures, a second linear fit provides a more accurate representation of the sensor capacitance than a constant fit. The fit functions $f(x, x_0, a, b)$ and $g(x, x_0, a, b, c)$ for the CV data of the unirradiated and irradiated TS are then defined as:

$$f(x, x_0, a, b) = -a|x - x_0| + ax + b \tag{5.2}$$

$$g(x, x_0, a, b, c) = a|x - x_0| + (a + c)x + b - cx_0 \tag{5.3}$$

Here, x represents the bias voltage, while a, c and b correspond to the slopes and offset of the fit functions, respectively. For the fits of the HPK TS, data from the second slope onwards is omitted, as these data points do not accurately represent the capacitance of the depleted structures. Figure 5.6 illustrates the fit function applied to the MSLTSF A structure of the Micron TS. All uncertainties in the fit parameters are assumed to be Gaussian. A summary of the parameter values obtained from the fits of the HPK and Micron CV curves is presented in Table 5.5.

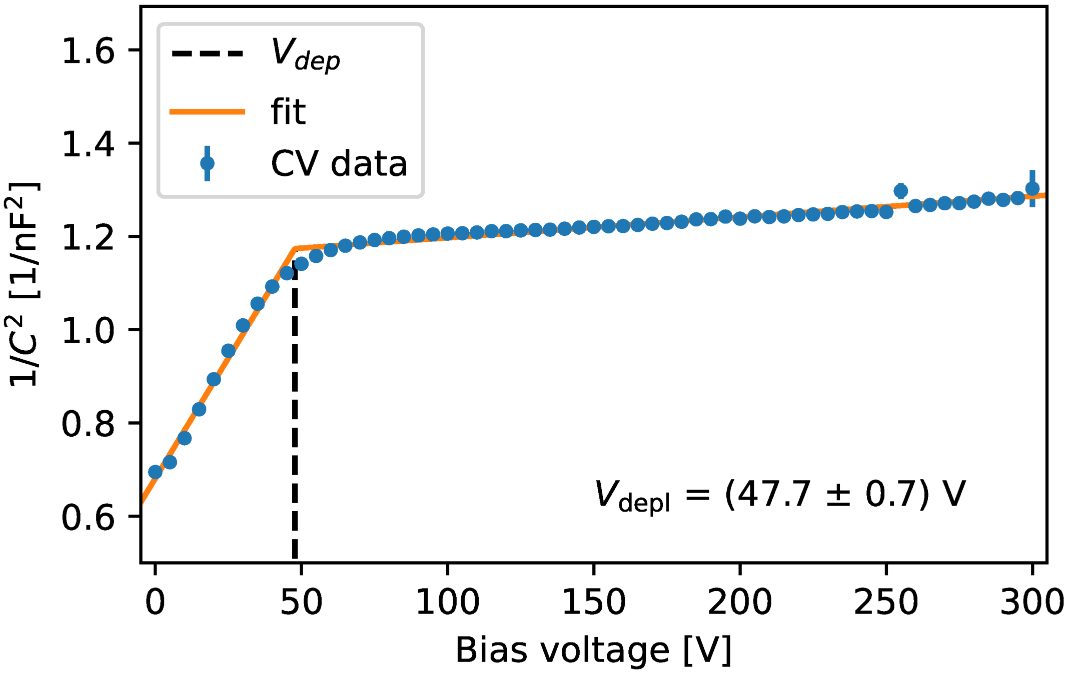

Figure 5.6: Capacitance of the Micron TS 0006 MSL A as a function of the applied bias voltage. Also shown are the fits according to Equation 5.3. The depletion voltage is defined by the intersection of the two linear slopes.

The depletion voltage of the HPK TS varies between 59 V and 63 V, with uncertainties of up to 1.2 V. A major contributor to these uncertainties is the limited number of data points used, particularly at higher bias voltages due to the presence of the second slope. The Micron MSL A structure exhibits a significantly higher depletion voltage than the other Micron TS, primarily due to its substantially higher received fluence of $5 \times 10^{15}\,\mathrm{n_{eq}/cm^2}$, compared to $2 \times 10^{15}\,\mathrm{n_{eq}/cm^2}$ for the MSL C structure. As described in Chapter 3.7, this behaviour is expected. With depletion voltages below 50 V, the structures require remarkably low bias voltages to reach full depletion, even after irradiation. However, the defined depletion voltage is determined solely by the transition of the fit function, which does not fully capture the depletion of the sensor volume, as the capacitance continues to increase slightly at higher bias voltages. This effect is known for irradiated silicon, where traps alter the expected depletion behaviour.

Table 5.5: Fit parameters of the CV data fit functions for the HPK and Micron TS. Values in brackets denote the standard deviation based on the last significant digit.

TS Substructure	x_0 **[V]**	**a [nF/V]**	**b [nF]**	**c [nF/V]**
HPK W1 TS1 $10 \times 5\,\mathrm{mm}^2$ (1. diode)	59.5(8)	15.0(3)	855(12)	
HPK W1 TS1 $5 \times 5\,\mathrm{mm}^2$ (2. diode)	60.6(11)	78.7(17)	4510(90)	
HPK W1 TS1 $5 \times 5\,\mathrm{mm}^2$ (3. diode)	60.7(12)	79.5(17)	4540(90)	
HPK W1 TS3 $10 \times 5\,\mathrm{mm}^2$ (1. diode)	60.3(9)	15.0(3)	869(13)	
HPK W1 TS3 $5 \times 5\,\mathrm{mm}^2$ (2. diode)	62.0(12)	79.0(17)	4610(90)	
HPK W1 TS3 $5 \times 5\,\mathrm{mm}^2$ (3. diode)	62.3(11)	78.4(16)	4620(80)	
HPK W1 TS4 $10 \times 5\,\mathrm{mm}^2$ (1. diode)	62.6(7)	14.1(2)	862(9)	
HPK W1 TS4 $5 \times 5\,\mathrm{mm}^2$ (2. diode)	67.8(8)	69.8(10)	4680(50)	
HPK W1 TS4 $5 \times 5\,\mathrm{mm}^2$ (3. diode)	68.7(10)	68.3(13)	4660(70)	
Micron W0006 MSL A	47.7(7)	-0.00494(1)	1.409(6)	0.0103(3)
Micron W0022 MSL C	37.2(5)	-0.00601(12)	1.385(5)	0.0125(3)

The saturation of the capacitance occurs through a smooth transition that the fit function does not accurately describe. Therefore, the uncertainty in the depletion voltage is non-negligible, despite the relatively small uncertainties in the measured capacitances. Since all investigated structures have a thickness of 150 µm and a depletion voltage well below 100 V, they pass the bulk capacitance measurement test.
Results from the same wafers, measured at the University of Göttingen, exhibit noticeable variations [65]. The higher depletion voltages observed at Göttingen are attributed to differences in sensor annealing.

5.4.2 IV Measurements

The leakage current per unit area for voltages up to 200 V is shown in Figure 5.7a. The first $5\,\mathrm{mm}^2$ diode of TS1 was omitted from the results due to significant surface damage. No breakdown voltage is reached for any structure, and all remain well below the maximum allowed leakage current of $750\,\mathrm{nA/cm}^2$ required to pass the test for unirradiated TS. The significant fluctuations in the leakage current around the nA range suggest additional influences on the IV characteristics, as the Keithley 2410 power supply should be capable of resolving these currents with sufficient precision. Noticeable surface damage, as shown in Figure 5.3b for the second $5 \times 5\,\mathrm{mm}^2$ diode of TS1, is likely to have a dominant impact on the leakage current at this scale. Despite the substantial fluctuations, the leakage currents of the HPK TS show consistent behaviour. The relative standard deviations, σ/μ, range from 2 to 20 % and show no significant dependence on either the structure or the applied bias voltage.

To investigate the bias voltage at which breakdown eventually occurs, the bias voltage was further increased for two diodes. As shown in Figure 5.7b, breakdown in the $5 \times 5\,\mathrm{mm}^2$ and $10 \times 5\,\mathrm{mm}^2$ diodes occurs at bias voltages exceeding 1 kV, far beyond the required $V_\mathrm{fd} + 70\,\mathrm{V}$.

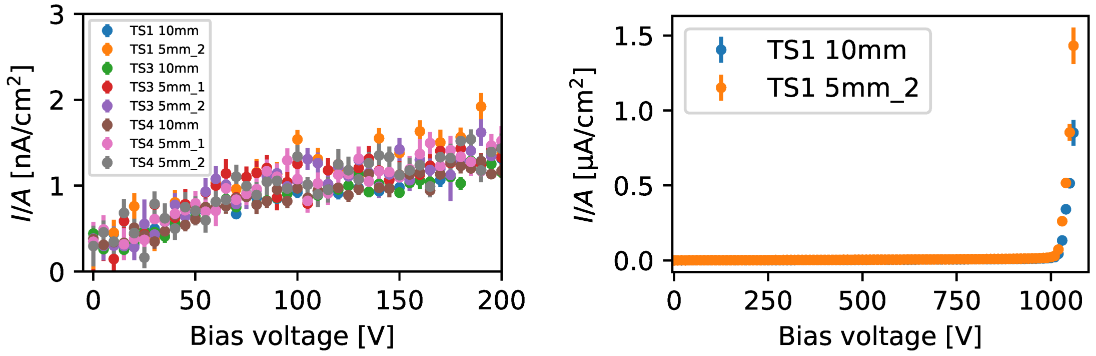

(a) **(b)**

Figure 5.7: a) Leakage current per area as a function of the applied bias voltage for all tested HPK TS diodes. b) Leakage current per area for increasing bias voltages until breakdown occurs for two HPK TS diodes.

The TS of wafer 0006 exhibit higher leakage currents due to their higher received fluences compared to wafer 0022 and the HPK wafer. All Micron TS meet the IV requirements, as they do not experience breakdown for bias voltages up to 600 V. The noticeably larger increase in leakage current for the MSL A structure at a bias voltage of 300 V is likely a consequence of increased radiation damage.

All measured leakage currents exhibit negligible fluctuations, with relative standard deviations of up to 0.2 %, highlighting the stability of the TS. As the leakage currents are much larger in comparison to the unirradiated HPK TS, small surface damages that might impair the signal-to-noise ratio only have minor influences. Results from different wafers of the same batch, measured at the University of Göttingen, show compatible results [65].

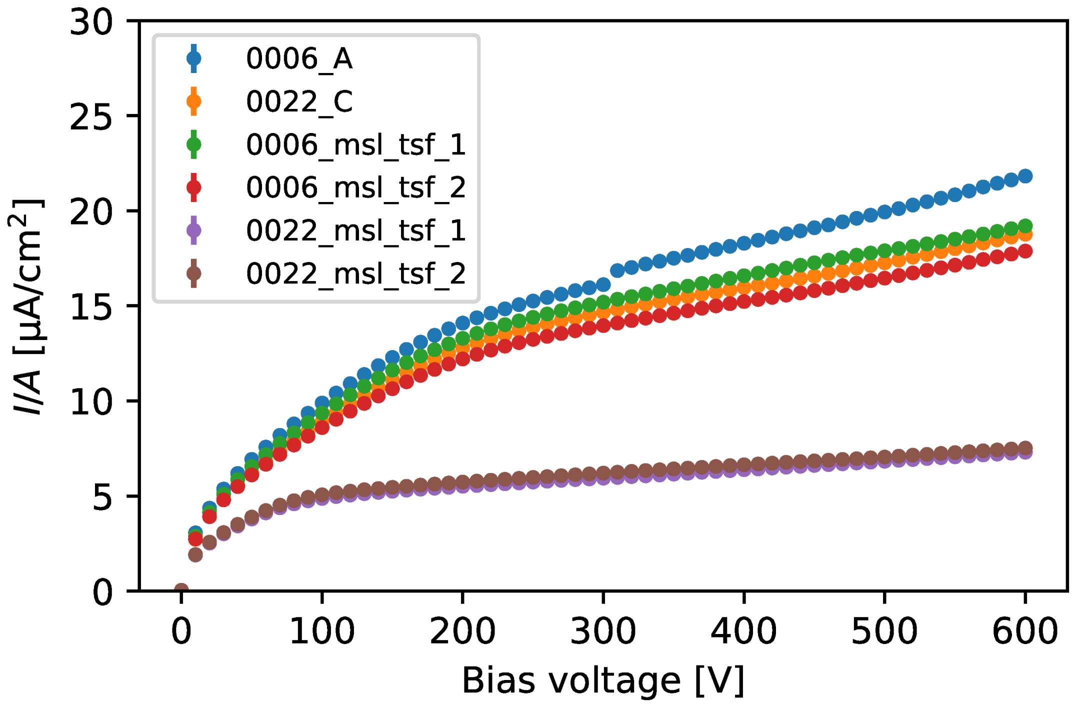

Figure 5.8: Leakage current per area as a function of the applied bias voltage for all investigated Micron TS diodes and quad structures.

5.4.3 It Measurements

The results of the 32 h to 48 h long It measurements at a bias voltage of 100 V are shown in Figure 5.9. These measurements primarily focus on the performance of the $10 \times 5\,\mathrm{mm}^2$ diodes. An It measurement of a single $5 \times 5\,\mathrm{mm}^2$ diode is also included, although temperature stability was lower, varying between 19.5 °C and 20.5 °C. In contrast, the temperatures during the measurements of $10 \times 5\,\mathrm{mm}^2$ diodes remained stable within (20.0 ± 0.1) °C. The measurement of the TS1 $10 \times 5\,\mathrm{mm}^2$ diode proved to be too unstable for extended periods, allowing only a 32 h measurement. However, these instabilities were unrelated to the TS itself.

Figure 5.10 shows that both investigated Micron TS exhibit very low fluctuations throughout the entire measurement period, for which stable temperatures of (-25.0 ± 0.1) °C were maintained. Due to their larger mean leakage current compared to the unirradiated structures, the fluctuations do not scale as significantly, making them more stable than the HPK TS. Table 5.6 lists the TS along with their maximum leakage current fluctuations I_{mf}, calculated according to Equation 5.1. The first 10 min of leakage current data is excluded from this calculation to prevent influences from unwanted effects of the bias voltage ramping. All investigated TS exhibit leakage current fluctuations below 25 %, thereby meeting the leakage current stability requirement. Comparable results were obtained from the QA measurements conducted at the University of Göttingen [65].

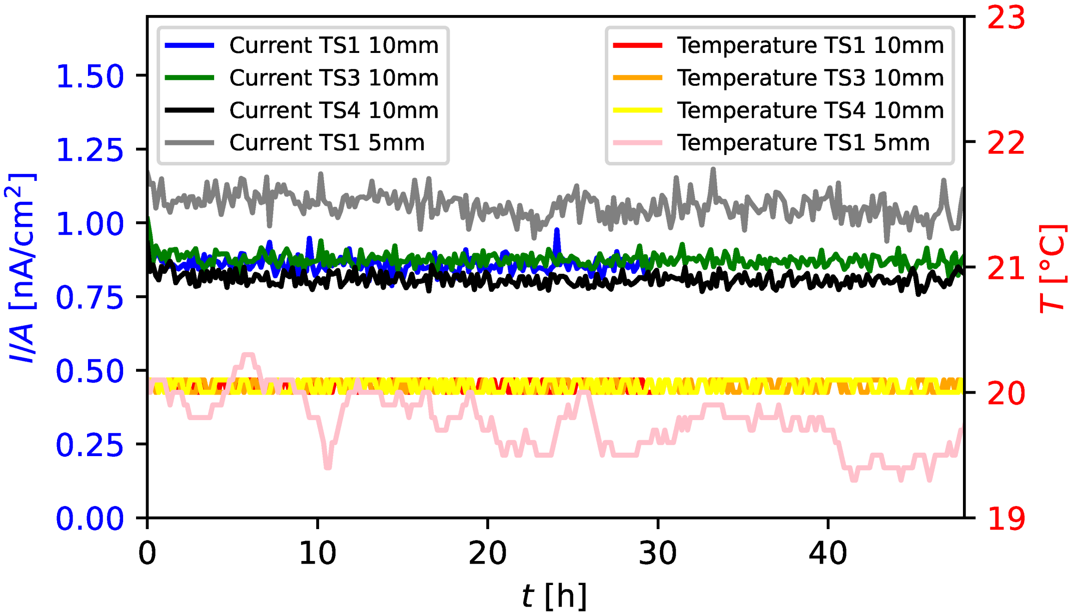

Figure 5.9: Leakage current per area as a function of time for a bias voltage of 100 V for HPK TS diodes.

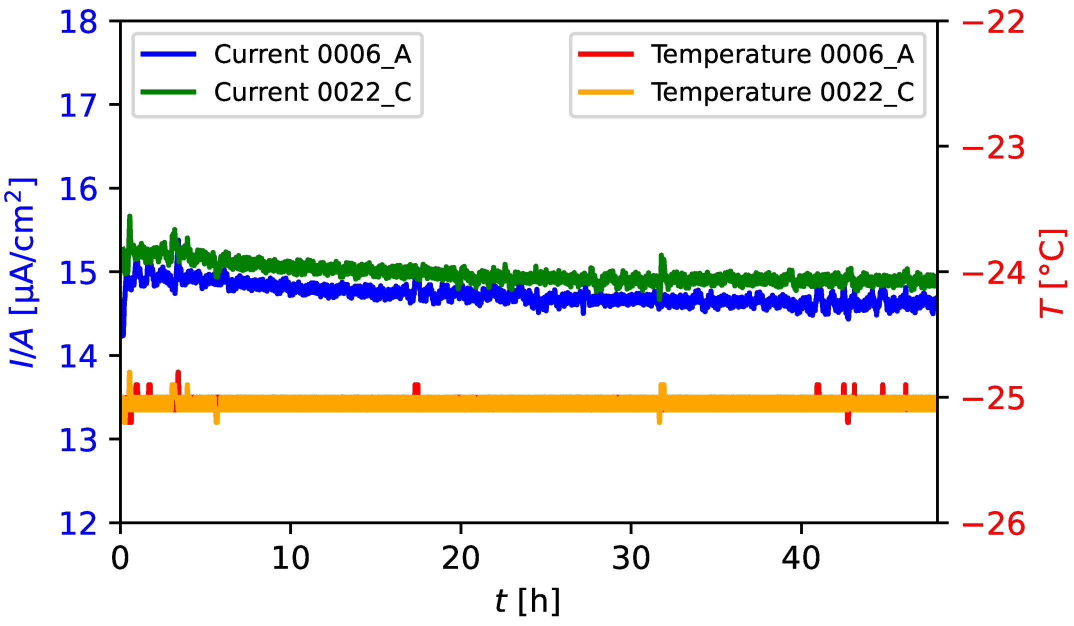

Figure 5.10: Leakage current per area as a function of time for a bias voltage of 100 V for Micron quad TS.

Table 5.6: Maximum fluctuations of the leakage current of the investigated TS.

TS Substructure	I_{mf}
HPK W1 TS1 $10 \times 5\,\mathrm{mm}^2$ (1. diode)	23.55 %
HPK W1 TS1 $5 \times 5\,\mathrm{mm}^2$ (3. diode)	23.02 %
HPK W1 TS3 $10 \times 5\,\mathrm{mm}^2$ (1. diode)	23.92 %
HPK W1 TS4 $10 \times 5\,\mathrm{mm}^2$ (1. diode)	21.49 %
Micron W0006 MSL A	7.74 %
Micron W0022 MSL C	6.65 %

The investigated HPK and Micron TS satisfy the requirements for the ITk Pixel Phase II upgrade, regarding their depletion voltage, leakage current stability and breakdown behaviour. This indicates that pixel sensors fabricated using these wafers are expected to operate reliably, without significant issues arising during sensor production. Further QA measurements will be conducted on TS from production batches in the future to ensure their electrical properties remain suitable for the operation of pixel modules in the ITk.

6 Track Reconstruction for High-Intensity Beam Tests

The performance of tracking detectors must be thoroughly evaluated before their installation in an LHC experiment. To assess these modules, beam tests are conducted, in which high-energy particle beams traverse a setup comprising the devices under test (DUTs) and the tracking sensors used for track reconstruction, commonly referred to as the beam telescope. While the physical setup is referred to as a hodoscope, this terminology is rarely used in the literature. Therefore, the term telescope is adopted throughout this thesis. The reconstructed tracks can be compared with the hit information from the DUTs to quantify the performance of the modules. Since accelerating particles to high energies is a complex endeavour, beam test facilities are located primarily near particle accelerators. Beam test data presented in this thesis were acquired at the beam test facility located at CERN.

This chapter provides an introduction to the beam test setups employed at CERN for data collection. Furthermore, it details the track reconstruction and beam test simulation software utilised. Subsequently, dedicated studies are presented to investigate the issue of fake track reconstruction. Different methods to identify fake tracks are compared in order to select an optimal strategy for mitigating fake tracks within the scope of this thesis and in future beam tests.

6.1 CERN Beam Tests

Several beam test areas at CERN are supplied with high-energy particles from either the PS or the SPS. For the studies presented in this thesis, all beam test data collected at CERN were acquired in the SPS North Area, specifically in the H6 beamline of the Experimental Hall North 1 (EHN1). The process of generating and delivering the particle beam to EHN1 is outlined in the following.

For data acquisition, particle beams with an energy of 120 GeV were utilised. These beams are produced by extracting and transporting the primary proton beam of the SPS, which has an energy of 400 GeV to 450 GeV [9], using a series of magnets and collimating elements. Typically, about 10^6–10^7 protons per spill are achievable [70].

The extracted beam is split into three beam channels, where it collides with beryllium or lead targets to generate secondary particle beams. To select particles with the desired momentum, so-called wobbling stations are employed. These stations consist of multiple sets of dipole magnets positioned upstream and downstream of the primary target, which are used to filter the secondary particles. The selected particles are then directed to the respective beam areas.

For the beam test, a variety of software and hardware components are essential for a successful data acquisition. The most prominent of these components is the beam telescope, which is used for track reconstruction of the particle trajectories. At CERN, this consists of six Mimosa26 sensors [71], two pairs of plastic scintillators used to trigger on the passing particles, a trigger logic unit responsible for distributing the trigger signal to the various sensors, and readout software for processing, transmitting, and storing the acquired data. Figure 6.1 illustrates the Aconite telescope [72], which was employed in the beam tests at CERN for the studies presented in this thesis. The different components of the beam test setup are explained in greater detail in the following sections.

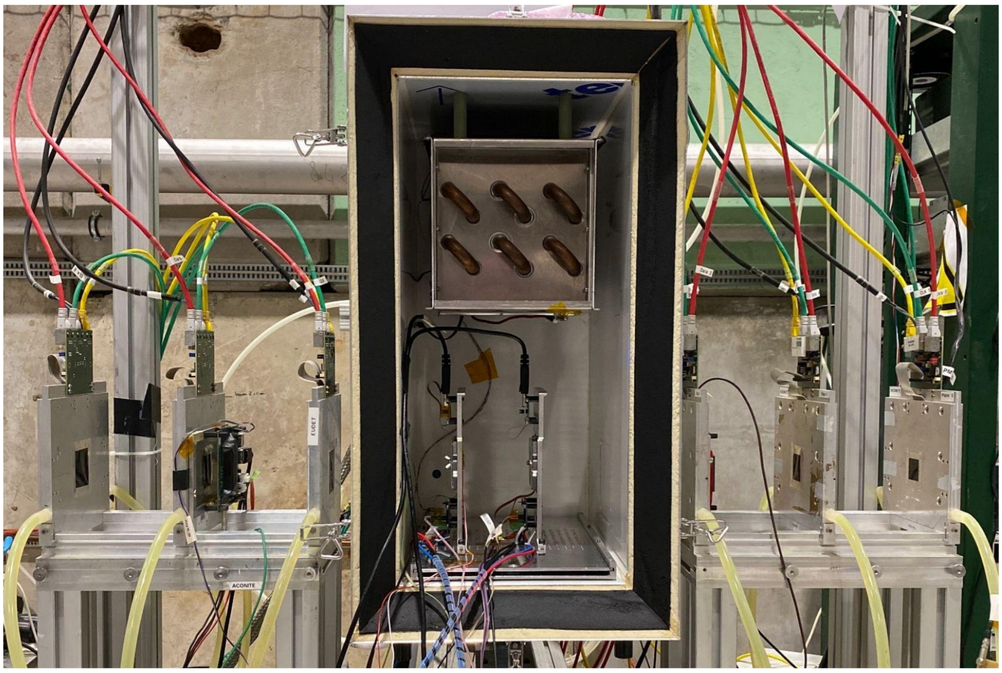

Figure 6.1: Image of the Aconite telescope at CERN, showing the six Mimosa26 sensors and two DUTs inside the cooling box. An FE-I4 module is mounted on the second Mimosa26 from the left [38].

The Beam Telescope and the Mimosa26 Sensor

The beam telescope consists of three Mimosa26 sensors in both the upstream and downstream arms, with the DUTs positioned in the cold box between them. This configuration ensures that a sufficient quality of the reconstructed tracks is achieved on both sides of the DUT, which is crucial for obtaining accurate track intercepts with the DUTs and, consequently, for a reliable performance evaluation.

The tracking sensors of a beam telescope must meet specific requirements. While the sensors do not need to be exceptionally radiation hard, they must provide excellent spatial resolution for effective track reconstruction. The Mimosa26 sensor is a monolithic active pixel sensor that has proven successful in charged particle tracking, due to its small pixel pitch of $18.4 \times 18.4\,\mu\text{m}^2$ and its thickness of only $50\,\mu\text{m}$. It has an active area of $21.1 \times 10.6\,\text{mm}^2$, with 1152 columns and 576 rows of pixels. The pixels are read out using a column-parallel rolling shutter, with an integration time of $115.2\,\mu\text{s}$. Since the DUTs have different integration times from the Mimosa26 sensors, an additional sensor is typically installed in the beam telescope to provide a time reference. In the case of the Aconite telescope, an FE-I4 module is used to filter out tracks that fall outside its $25\,\text{ns}$ integration time window. In addition, an ITkPixV1.1 module was usually installed as a second time reference, in case problems occurred with the FE-I4 module.

To ensure the DUTs are kept at temperatures around $-35\,^\circ\text{C}$ and to avoid significant leakage currents, they are housed in a cold box. This box is fully sealed to minimise light exposure to the sensors and is filled with cold nitrogen gas to prevent condensation of water. A cooling circuit connected to a chiller provided stable, low temperatures.

The Trigger System

After particles deposit energy in the sensors of the beam telescope and the DUTs, a trigger signal must be sent to all the sensors to ensure that the hit information from the same particle is read out. This approach ensures that the recorded events contain consistent information, which can be further analysed after data taking.

When particles traverse the telescope, signals of two pairs of scintillators positioned in front and behind the telescope are sent to the trigger logic unit (TLU) [72]. The TLU is a device specifically designed to process and respond to trigger conditions. It also provides a time stamp and trigger ID for the particles passing through the system. This guarantees that only particles that traverse the entire telescope are triggered. The time resolution of the scintillators is discussed in Chapter 8.2.

For the CERN beam tests involving the quad modules investigated in this thesis, the EUDET-type TLU [72] was used. For subsequent beam tests and the in-time efficiency measurements performed at CERN, as presented in Chapter 8, the newer AIDA TLU [73] was utilised. This system provides significantly improved timestamping accuracy, capable of measuring events with a precision of up to 780 ps in comparison to the 20.83 ns timing precision of the EUDET TLU [74]. Figure 8.1 in Section 8.1 shows one possible setup of a TLU in a beam test.

The EUDAQ Software

The measured data processed by the readout chip of the detectors must undergo further processing before being stored in raw data files. For the beam telescope, this is achieved using the data acquisition (DAQ) software EUDAQ [75], which was developed to provide versatility in the operation of beam telescopes and DUTs.

The core component of the system is the Run Control module, which connects to all other components of the DAQ system and the user interface. This module sends commands to the other modules and collects information from them.

All log messages generated by the DAQ system are collected and displayed by the LOG collector module, providing the user with information on the status of data acquisition and any potential issues.

The producer modules link the DAQ system to the hardware of the detectors, enabling access to the measured data via the EUDAQ library. New detectors require additional readout software that serves as an interface between the specific readout system's DAQ software and the EUDAQ library. For the ATLAS ITkPix readout chip, the YARR readout software [58] was used during the CERN beam tests.

The data received from all producers is then collected and synchronised online by the collector nodes, a process known as event building. A single event corresponds to one trigger signal from the TLU. All data processed by the data collector is stored and can be monitored online to detect any issues that may arise during data acquisition.

Figure 6.2 illustrates the different modules of the EUDAQ DAQ system and their relationships to one another schematically.

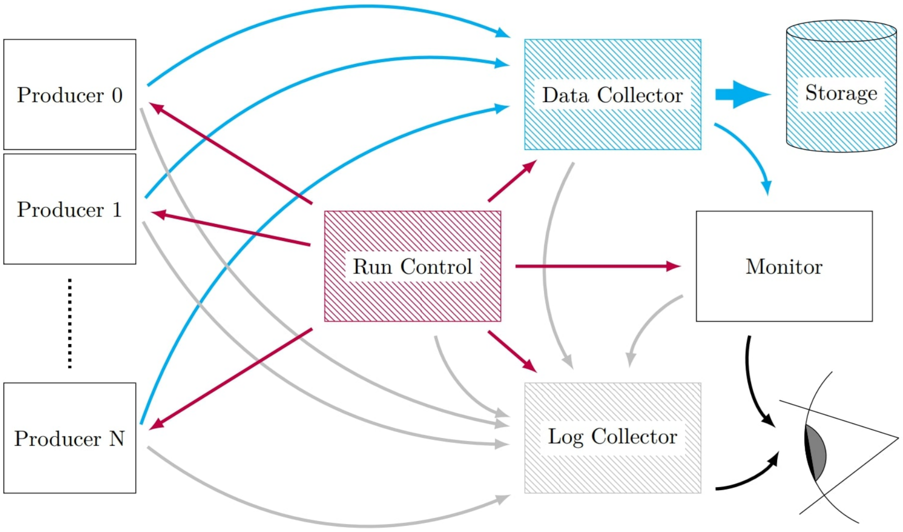

Figure 6.2: Schematic depiction of the DAQ system of EUDAQ. The red arrows represent the commands sent by the run control module, the blue arrows represent the flow of the data and the gray arrows represent the logs that are sent to the LOG collector. [76].

6.2 The Beam Test Simulation Software Allpix Squared

Allpix Squared [77] is a versatile simulation framework designed for simulating particle interactions in semiconductors. Originally developed at CERN for the simulation of beam tests, it has since been extended to broader applications in semiconductor simulation. Using beam test simulations, various aspects of the setup and track reconstruction of customisable particle beams can be investigated under controlled conditions.

Allpix Squared relies on the Geant4 [78] toolkit to simulate energy deposition, while the ROOT [79] framework is employed to store the data. The simulation process is divided into individual modules, making the software more user-friendly, while still allowing for the realisation of complex detector simulations.

The core of the framework manages the instantiation and processing of the modules, which are organised into four subsystems. All modules are executed through the module instantiation logic. The detector geometry subsystem provides information about all detector types, their position and orientation, and additional passive materials. Further properties, such as the pixel matrix, pixel size, and thickness, can be specified to override the default properties of the given detector type or to design a custom detector. Objects are tracked and moved in the simulation by the messaging subsystem, which interacts with all modules in the simulation chain. The fourth subsystem is the user interface, which enables users to interact with the framework. Figure 6.3 illustrates the structure of the Allpix Squared core and its connection to the modules.

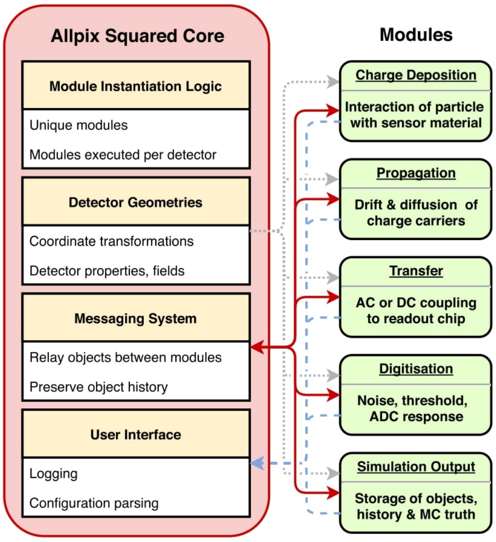

Figure 6.3: Allpix Squared subsystems and their connection to the modules [77]. The red, gray and blue lines depict the interaction of the modules with the messaging system, the detector geometry and the user interface, respectively.

The main modules that define the simulation chain are outlined below. All simulations begin with the main *Allpix* module, which defines global parameters such as random seeds, file paths, verbosity, and the number of simulated events. The surrounding material is then specified separately, either as vacuum or air, using the *GeometryBuilderGeant4* module.

Electric fields, including constant, linear, parabolic, and custom fields, can be simulated within the sensors using the *ElectricFieldReader* module. The electric field of each sensor can be customised individually, though only the linear model is used in the scope of this thesis. For linear electric fields, it is necessary to specify the depletion depth and bias voltage within the module, which together define the constant slope.

Next, the propagation of charge carriers is simulated. This is achieved through several modules that employ different approaches, each with its own advantages and limitations. Focusing on precision at the expense of computational speed, the *GenericPropagation* module is the preferred choice for beam test simulations. Propagation is modelled as a combination of diffusion and drift of grouped charge carriers. To determine the drift, the module uses the charge carrier mobility. Both types of charge carriers are considered during propagation. Customisable parameters include the mobility model, the number of charge carriers grouped together for propagation, temperature, integration time, and more advanced options such as impact ionisation, trapping, and detrapping models and the magnetic field. No magnetic field was applied in any beam tests related to the results presented in this thesis.

The individual sets of propagated charges are then combined into a set of charges on the corresponding sensor pixel by the *SimpleTransfer* module. This step prepares the charges for processing by the readout electronics. Charges located outside the pixel grid or those too far away from the implants will be discarded. The collected charges are subsequently digitised into a signal proportional to the input charge using the *DefaultDigitizer* module. A positive signal threshold can be defined, which is compared to the absolute value of the collected charge. If the charge does not exceed the threshold, all collected charge for a pixel in an event is discarded. Additionally, a Gaussian distribution representing the input noise of the preamplifier is added to the collected charge. A charge-to-digital converter can be simulated to obtain a digitised output in bits. Parameters for noise effects during the charge-to-digital conversion, as well as the threshold value and gain factor, can be specified to simulate more realistic FE electronics.

In addition to storing simulated data in the form of ROOT files, the *LCIOWriter* module allows the creation of files that are directly compatible with the track reconstruction software Corryvreckan, which is discussed in more detail in the following section.

6.3 The Track Reconstruction Software Corryvreckan

Measured and simulated data are reconstructed after the data taking to analyse the detector performance. The currently most developed track reconstruction software for beam test data is the Corryvreckan framework [80]. It was designed to be fast and lightweight, with a modular structure similar to Allpix Squared. The software aims to provide a user-friendly application while ensuring adequate track reconstruction in complex data-taking environments.

To initiate the reconstruction chain, the entire detector setup, including the detector type, position, orientation, pixel pitch, and material budget, must be specified in a geometry file. All other parameters related to the modules that define the reconstruction chain are specified in the main configuration. Global framework parameters are defined within the Corryvreckan module, including the maximum number of events and tracks to be processed, as well as the paths to the raw data and geometry files.

Information is temporarily stored and accessed via the so-called Clipboard. This infrastructure allows the metadata of the currently processed events to be stored and accessed by the various modules.

Figure 6.4 illustrates the track reconstruction chain of Corryvreckan. The main modules used for track reconstruction in the scope of this thesis are described below.

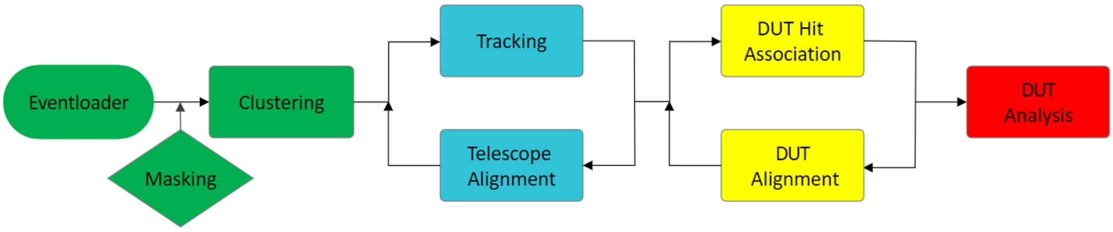

Figure 6.4: Track reconstruction chain of Corryvreckan with the commonly used modules. Additional modules are available for more specialised use cases.

Event Loading

Measured data are loaded via the EventLoader modules, which depend on the type of module under investigation and the format of the data. For ITk pixel test beams at CERN, the *EventLoaderEUDAQ* and *EventLoaderEUDAQ2* modules were used. Multiple EventLoader modules can be employed in a single reconstruction, with the first module defining the event on the clipboard through a time window or trigger numbers.
To load simulated data from Allpix Squared or data stored in ROOT format, the *FileReader* module is used instead. The loaded data contains information about the pixel hit coordinates in both space and time.

Masking

Noisy and dead pixels can be masked using the *MaskCreator* module, which provides various methods for defining the criteria that determine whether a pixel is considered noisy. The commonly used approach is to set a frequency cut factor, which is multiplied by the global average pixel hit rate to define a threshold. Any pixel with a hit count exceeding this threshold will be masked. However, the global average pixel hit rate of a sensor depends on the size of the beam spot relative to the sensor area, as pixels with zero hits are also included in the calculation. Therefore, an optimal frequency cut value cannot be universally defined and is dependent on the specific beam test setup. Masked pixels are excluded from any subsequent reconstruction steps.

Clustering

Charge carriers generated by a single particle can propagate to multiple electrodes, leading to hits being registered in several neighbouring pixels. Pixel hits are then combined into clusters based on their spatial and temporal information using the *Clustering4D* module. The cluster centre can either be calculated as the arithmetic mean of the pixel centres or determined using the centre-of-gravity algorithm, which takes into account the amount of charge deposited in the pixels. The latter method improves the spatial resolution of

the sensors, particularly for clusters containing more than one pixel.
Cuts can be applied to the spatial distance and the time window for clustering pixel hits together, though no cuts were applied for the beam test results presented in this thesis.

Tracking

Track reconstruction is performed by the *Tracking4D* module, which uses the cluster centre position and time information. Cluster centres from the tracking planes are included in the reconstruction of a track only if their positions are within a predefined distance of each other. These spatial cuts can either be defined by a distance in the x- and y-directions, or by a factor, which is multiplied by the spatial resolution of the individual tracking planes. Initially, large distance values are set to account for significant misalignments, as little to no tracks would be reconstructed otherwise.
Different track models can be used to fit the track. The two most commonly employed track models are the straight line and the General-Broken-Lines (GBL) algorithm [81]. In the straight line model, a track is fitted through the clusters of the participating planes, assuming no scattering effects. This model provides an adequate approximation of particle tracks when scattering is minimal. In contrast, the GBL algorithm fits a track with kinks at the sensor planes and it models their volume as thin scattering layers near the sensors.
The tracking module fits a track through all possible combinations of clusters within the defined spatial and temporal cuts. Regardless of the tracking model used, a straight line is used when trying to determine all possible track fits.

Telescope Alignment

For the reconstruction of high-quality tracks, the geometry file must accurately describe the physical setup, ideally down to the single-micrometre scale. Since the positions of the sensors are only measured approximately, the geometry file provides an approximation of the actual positions and orientations. As a result, directly connecting the cluster centres of the individual sensors does not precisely describe the particle tracks. To address this, the alignment of all planes participating in the track reconstruction is required, which is performed using the *AlignmentChi2* module. This module performs both translational and rotational alignment of the tracking planes to optimise the track fits. The quality of the track fit is determined by the χ^2 value:

$$\chi^2_{\mathrm{SL}} = \sum_i ((r_{x,i}/\sigma_{x,i})^2 + (r_{y,i}/\sigma_{y,i})^2) \tag{6.1}$$

$$\chi^2_{\mathrm{GBL}} = \sum_i ((r_{x,i}/\sigma_{x,i})^2 + (r_{y,i}/\sigma_{y,i})^2) + \sum_{j-1} ((\mathit{\Phi}^2_{x,j}/\sigma_{\mathit{\Phi}_x,j})^2 + (\mathit{\Phi}^2_{y,j}/\sigma_{\mathit{\Phi}_y,j})^2) \tag{6.2}$$

Here, i denotes the number of tracking planes, and j represents the number of scatterers at which the particle tracks can have an angle. The quantities $\varPhi$ correspond to the scattering angles, while the terms σ_i and $\sigma_{\varPhi,j}$ refer to the spatial resolution and the uncertainty of the scattering angle, respectively. The residuals r describe the distance between the reconstructed track intersection and the corresponding cluster centre of a tracking plane in the x- and y-directions. For a uniform distribution of particles traversing a sensor pixel, the residual distribution of one-pixel clusters ideally follows a uniform distribution with a standard deviation of $\sigma = \text{pixel pitch}/\sqrt{12}$. However, due to noise and finite spatial resolution, this uniform distribution is convoluted with a Gaussian distribution.

Successful alignment is assessed by analysing the shape and position of the residual and scattering angle distributions, particularly for the GBL algorithm. A common metric for evaluating the quality of reconstructed tracks, which is independent of the number of degrees of freedom (ndof) of individual track fits, is given by χ^2/ndof. Multiple alignment iterations are typically required until the geometry converges and the χ^2/ndof distribution exhibits a most probable value of one.

DUT Alignment and Analysis

To analyse the performance of the DUTs, the reconstructed tracks are associated with cluster centres on the DUTs within predefined spatial and temporal cuts. This task is performed by the *AlignmentDUTAssociation* module. Since the DUTs are initially misaligned, an additional iterative alignment procedure is required. During this process, the reconstructed tracks remain unchanged, and only the DUTs are shifted and rotated until their residual distributions are optimised. After successful alignment, optional analysis modules can be executed to extract key performance metrics. The *AnalysisEfficiency* module is used to determine the average efficiency ϵ of the DUTs, based on the number of tracks with an associated cluster n_{assoc} and the total number of tracks n_{tracks}:

$$\epsilon = \frac{n_{\text{assoc}}}{n_{\text{tracks}}} \tag{6.3}$$

The statistical uncertainty $\sigma_{\epsilon,\text{stat}}$ of the efficiency is estimated using the binomial uncertainty:

$$\sigma_{\epsilon,\text{stat}} = \sqrt{\frac{\epsilon(1-\epsilon)}{n_{\text{tracks}}}} \tag{6.4}$$

6.4 Simulation and Track Reconstruction of High-Density Beams

The accuracy of track reconstruction strongly depends on the beam's particle density. As discussed in Section 6.3, the track-finding algorithm attempts to fit tracks by combining clusters from different tracking sensors based on predefined spatial and temporal constraints, referred to as the matching radius. A larger spatial matching radius increases the number of successfully reconstructed tracks. However, if multiple clusters are registered in an event by the tracking planes, the algorithm may form tracks from clusters that do not originate from the same particle trajectory. For high particle densities, the number of reconstructed tracks per event can significantly exceed the actual number of particle hits recorded by the tracking planes. This effect can degrade the reconstruction quality and compromise the evaluation of the DUT performance. Therefore, it is crucial to assess the severity of this issue and to implement appropriate mitigation strategies.
The challenge of tracking high-density particle beams is not exclusive to high-energy particle physics but also arises in fields such as proton computed tomography [82, 83]. A study on the reconstruction of high-density proton beams using Corryvreckan in the context of proton computed tomography has already been conducted [84].

Since all beam test results presented in this thesis originate from the ACONITE telescope at CERN, the Allpix Squared simulations were designed to closely replicate this specific setup. The simulation includes six Mimosa26 sensors for tracking and two IBL planar sensors as DUTs, which also serve as potential scatterers. To match the real experimental conditions, two aluminium boxes surrounding the DUT were incorporated as passive material. No misalignments were introduced in the simulation, as the focus of this study is on track multiplicity in high-density beams. A linear electric field model is employed to describe the internal sensor fields, assuming full sensor depletion. Charge transport is simulated using the more accurate GenericPropagation module. A uniform threshold of 600 e is applied across all planes, ensuring the detection of traversing particles. Gaussian noise fluctuations with a standard deviation of 150 e are superimposed on the signals. The outer and inner aluminium boxes have thicknesses of 10 mm and 5 mm, respectively. The simulation environment is set with air as the surrounding material and a temperature of 293 K (room temperature).
A 120 GeV pion (π^+) beam is simulated with Gaussian-distributed beam profile width $\sigma_{\text{width}} = 3\,\text{mm}$, opening angle distribution $\sigma_{\text{angle}} = 0.1\,\text{mrad}$, and energy resolution $\sigma_{\text{Eres}} = 500\,\text{MeV}$. The opening angle distribution and energy resolution are chosen to be equal to or slightly higher than the expected values in the actual particle beam. This ensures additional variation in particle tracks, which is beneficial for subsequent training processes of machine learning algorithms, as discussed in Section 6.5. For the CERN SPS H6 beam line [85], a maximum relative momentum spread of $\Delta p/p = 1.5\,\%$

is achievable. Given that energy and momentum are approximately linearly proportional at high energies, this corresponds to an energy uncertainty of roughly 1.8 GeV. However, in practice, a lower relative momentum spread of approximately 0.5 % is typically used. The exact value was not known at the time of the simulation. Therefore, an estimation of 500 MeV was chosen for this study, which corresponds to a relative momentum uncertainty of approximately 0.42 %. The angular distribution of the particle beam has a standard deviation of approximately 100 µrad, which is adopted for the simulation. The beam profile is modelled as a Gaussian distribution with a standard deviation of 3 mm, a common value for collimated beams in beam test experiments, representing a standardised case.

To investigate a high beam density, a simulation comprising 5000 events, each containing 200 pions, is performed. Particle hits within a single event cannot be temporally resolved any further. The geometry of the experimental setup and the particle beam is illustrated in Figure 6.5. Given the small material budget of the setup, the probability of high-energy pions undergoing large-angle scattering in the telescope and passive material is low. The track reconstruction of the simulated pions is discussed in the following chapter.

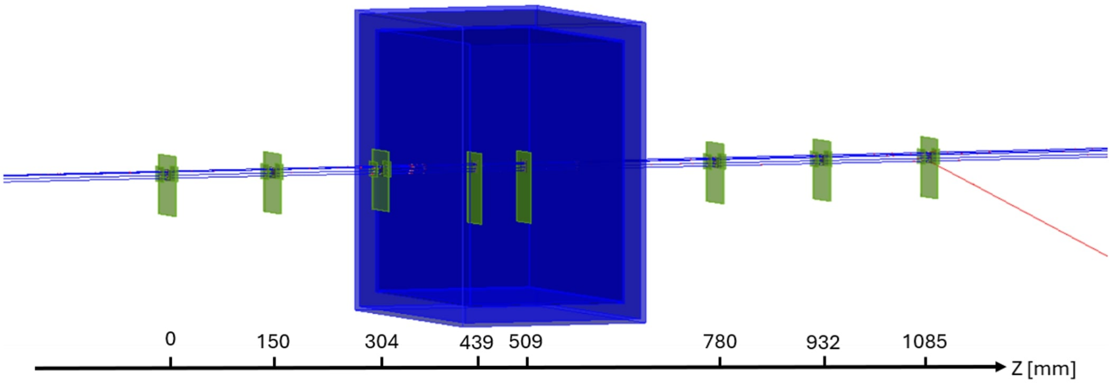

Figure 6.5: CERN beam test simulation using six Mimosa26 sensors as tracking planes and two IBL planar sensors as DUTs inside an aluminium box. The blue lines are traversing pions and the red lines are secondary electrons.

The track reconstruction of the simulated pions is highly dependent on the parameters chosen for the module, particularly the track fit model, the matching radius, and the number of participating tracking planes. In this study, a track is only fitted if there is a hit on all six tracking planes and the clusters are within a matching radius of ten times the spatial resolution of the tracking planes, where $\sigma_{\text{spatial}} = 18.4\,\mu\text{m}/\sqrt{12} \approx 5.31\,\mu\text{m}$. In most ITk pixel beam tests, a matching radius of 100 µm is typically selected as a good compromise between the number of reconstructed tracks and the exclusion of false tracks. A smaller matching radius is deliberately chosen here to emphasise the issue of tracking multiplicity, even for a conservative choice of spatial cuts. The GBL algorithm is employed as the track model to account for the scattering of particles, ensuring a more accurate representation of the particle tracks.

Figure 6.6a demonstrates that almost all pions traversed the entire telescope, as indicated by the nearly identical number of clusters on both the first and last planes. Ideally, with 200 particles per event, a track should be reconstructed for each particle. However, Figure 6.6b shows that a significant number of events result in the reconstruction of more tracks, with a track multiplicity reaching up to 400 tracks per event, culminating in a total of 1.54 million tracks.
Such a high track multiplicity is expected due to the high particle density per event, which is substantially greater than what is typically encountered in actual beam tests. In this thesis, a higher density was deliberately chosen to estimate and mitigate the reconstruction of fake tracks in real beam test setups involving high-density beams. If the reconstructed tracks contained even 1 % of fake tracks in an actual beam test, the determined average efficiency of the DUTs would be severely reduced. Therefore, it is essential to explore strategies in order to prevent the inclusion of fake tracks in the analysis of the DUT performance.
Several approaches can be applied to address this problem. In this thesis, results from one-dimensional cuts on the χ^2/ndof-values are compared with those from a machine learning approach and are discussed in Section 6.6. The following chapter provides an overview of the employed machine learning methods.

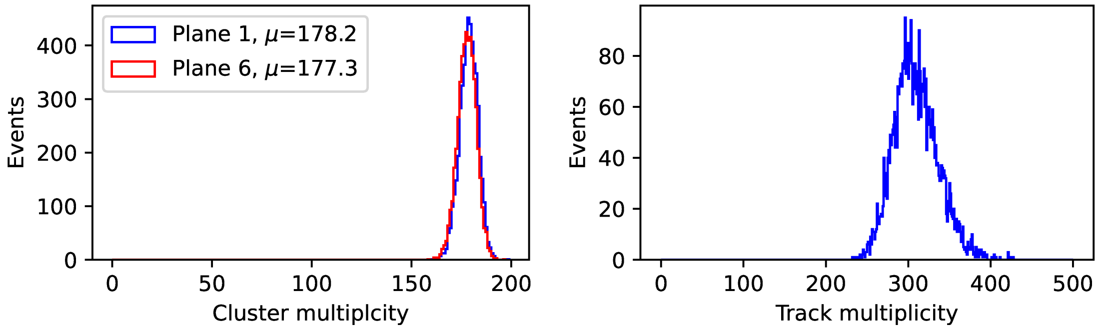

(a) **(b)**

Figure 6.6: Number of clusters (a) and reconstructed tracks (b) per event. A total of 5000 events, each containing 200 pions, were simulated. Here, μ denotes the mean of the distribution.

6.5 Introduction to Supervised Learning and Boosted Decision Trees

Solving a binary classification problem like the identification of real and fake tracks in track reconstruction can also be done with a machine learning approach. In order to minimise the risk of including fake tracks in the analysis, a classifier may be beneficial for taking correlations of multiple input features into account in comparison to one-dimensional cuts used in Corryvreckan. In this thesis, the XGBoost [86] library is used to train on and identify reconstructed tracks from simulated Allpix Squared data.
This is achieved by the implementation of boosted decision trees (BDTs) for a supervised learning problem. BDTs are highly efficient with optimised training on large datasets, while still being robust to feature scaling and outliers. The following subsections briefly explain the concepts of supervised learning and BDTs. A detailed introduction of XGBoost and the implementation of its BDTs is found at [86].

6.5.1 Supervised Learning

Supervised learning involves predicting a target variable y_i using training data x_i that consists of several features. The model defines a mathematical relationship that generates predictions from the input data. A typical example is a linear model, where predictions are made by computing a weighted sum of the input features:

$$\hat{y}_i = \sum_j \Theta_j x_{ij} \tag{6.5}$$

Here, the coefficients Θ_j are parameters that must be learned from the training data. The process of training the model involves finding the optimal values of these parameters to accurately predict the target variable y_i from the inputs x_i. This requires defining and optimising an objective function, which evaluates how well the model fits the training data. The objective function typically combines the training loss function $L(\Theta)$ and a regularisation term $\Omega(\Theta)$:

$$\mathrm{obj}(\Theta) = L(\Theta) + \Omega(\Theta) \tag{6.6}$$

The mean squared error (Equation 6.7) is commonly used as a training loss function for regression tasks, predicting continuous values, while logistic loss (Equation 6.8) is used for binary classification tasks, such as logistic regression.

$$L(\Theta) = \sum_i (y_i - \hat{y}_i)^2 \tag{6.7}$$

$$L(\Theta) = \sum_i \left[y_i \ln(1 + \mathrm{e}^{-\hat{y}_i}) + (1 - y_i) \ln(1 + \mathrm{e}^{\hat{y}_i}) \right] \tag{6.8}$$

Logistic regression is a statistical method that models binary dependent variables using logistic functions. Its advantage over the mean squared error model lies in its better penalisation of incorrect predictions due to the proper definition of a probability score associated with the output.

Regularisation helps to control the complexity of the model by increasing the loss depending on properties aimed to be pruned, thereby preventing overfitting. Overfitting occurs when the model becomes too tailored to the training data, capturing noise and random fluctuations rather than the underlying pattern. This negatively impacts the model's performance on new, unseen data, as it fails to generalise effectively.

6.5.2 Boosted Decision Trees

Decision trees are structured diagrams used to classify a target variable based on a series of decisions. These trees consist of internal nodes, which represent tests on attributes, branches that indicate the outcomes of these tests, and leaf nodes, which are the terminal points that do not split the data further.

The XGBoost library employs an ensemble of decision trees known as classification and regression trees (CARTs) [87]. Each CART assigns a prediction score to its leaves. Since the prediction from a single tree is typically not very accurate, the predictions from multiple trees are aggregated. The process of combining multiple weak learners into an individual strong learner is known as boosting. This can be expressed mathematically as:

$$\hat{y}_i = \sum_{k=1}^{K} f_k(x_i)\,,\ f_k \in \mathcal{F} \tag{6.9}$$

$$\mathrm{obj}(\Theta) = \sum_i l(y_i, \hat{y}_i) + \sum_{k=1}^{K} \Omega(f_k), \tag{6.10}$$

where K is the number of trees, $l(y_i, \hat{y}_i)$ is the loss function measuring the difference between the predictions and the target variable, $\mathcal{F}$ is the set of all possible CARTs, and f_k represents an individual decision function within the ensemble.

Unlike random forests [88], which create a multitude of independent decision trees and combine their results, gradient boosting methods like XGBoost build trees sequentially, combining them iteratively to improve performance [89].

Optimising the objective function for BDTs is done using additive training, where previously trained trees are kept fixed, and a new tree is added at each step t. This process is described by:

$$\hat{y}_i^{(t)} = \sum_{k=1}^{t} f_k(x_i) = \hat{y}_i^{(t-1)} + f_t(x_i) \tag{6.11}$$

Each newly added tree is optimised to improve the objective function, which at step t is given by:

$$\mathrm{obj}^{(t)} = \sum_{i=1} \left[g_i f_t(x_i) + \frac{1}{2} h_i f_t^2(x_i) \right] + \Omega(f_t) \tag{6.12}$$

$$g_i = \partial_{\hat{y}_i^{(t-1)}} l(y_i, \hat{y}_i^{(t-1)}) \tag{6.13}$$

$$h_i = \partial^2_{\hat{y}_i^{(t-1)}} l(y_i, \hat{y}_i^{(t-1)}) \tag{6.14}$$

Using the second-order Taylor expansion of the loss function provides a more accurate approximation compared to regular gradient boosting algorithms [90]. Additionally, the objective function's dependence on g_i and h_i allows XGBoost to employ custom loss functions, including logistic regression. However, a regularisation term must be defined. XGBoost uses the following definition:

$$\Omega(f) = \gamma T + \frac{1}{2} \lambda \sum_{j=1}^{T} \omega_j^2, \tag{6.15}$$

where ω is the vector of scores on leaves, γ is the minimum loss reduction required to partition a leaf, T is the number of leaves, and λ is the Ridge regularisation term [91] that penalises the ω_j to control the regularisation term. The first term of the regularisation discourages deep trees by adding a penalty for each additional leaf, while the second term shrinks large weight values to prevent extreme predictions, making the model more stable. With this definition, the objective function for a single tree simplifies to:

$$\mathrm{obj} = -\frac{1}{2} \sum_{j=1}^{T} \frac{G_j^2}{H_j + \lambda} + \gamma T, \tag{6.16}$$

where G_j and H_j are the sums of g_i and h_i over all data points, respectively. This equation evaluates the quality of a tree structure, with a lower score indicating a better structure. Since enumerating all possible trees is impractical, optimisation occurs one level at a time. For each potential split of a leaf into new left (L) and right (R) leaves, the gain in structure score is:

$$\mathrm{Gain} = \frac{1}{2} \left[\frac{G_\mathrm{L}^2}{H_\mathrm{L} + \lambda} + \frac{G_\mathrm{R}^2}{H_\mathrm{R} + \lambda} - \frac{(G_\mathrm{L} + G_\mathrm{R})^2}{H_\mathrm{L} + H_\mathrm{R} + \lambda} \right] - \gamma \tag{6.17}$$

This definition allows the classifier to determine an optimal split by calculating the gain of all possible splits. The classifier operates using predetermined hyperparameters that are not adjusted during training, like the parameters γ and λ. These parameters define the properties of the learning process and must be optimised based on the learner's performance.

6.6 Utilisation of BDTs for Fake Track Identification

In the context of track reconstruction, a track inherits several features that characterise it. The most notable are the χ^2/ndof value, the scattering angles at the tracking planes, and the cluster sizes of the particle hits. These features can be determined during the track reconstruction process. In an Allpix Squared simulation, the Monte Carlo truth information for each particle and its trajectory is accessible. This allows a machine learning model to be trained using the input features of reconstructed tracks, enabling it to distinguish between real and fake tracks based on these characteristics. As discussed in greater detail in Chapter 6.5.2, the chosen machine learning method for identifying real and fake tracks is based on boosted decision trees from the XGBoost library.

Three similar simulations were conducted to evaluate the performance of the machine learning model: the training, validation, and test datasets, each containing 200 π^+ per event. A total of 1 million π^+ were simulated in the training dataset to enable the machine learning model to optimise the weights of the splits in the boosted decision trees. The validation set consists of 250k π^+ and is used to determine the optimal number of boosting rounds. This is achieved by monitoring the predictive power of the model on the validation dataset until it ceases to improve for ten consecutive boosting rounds, preventing overfitting. Once the optimisation process is complete, a final, previously unseen test dataset consisting of 250k π^+ is used to independently assess the performance of the machine learning model.

Input features can be correlated with each other, which reduces their effectiveness in distinguishing between real and fake tracks. To assess these correlations, the Pearson correlation coefficient [92] is calculated for all feature pairs. This coefficient quantifies the linear relationship between two variables and ranges from 1 (maximum correlation) to -1 (maximum anticorrelation). Figure 6.7 presents the Pearson correlation coefficient for all input features. A notable correlation exists between the scattering angles and the χ^2 value, which is expected, as the χ^2 value depends on the scattering angle, as defined in equation 6.2.

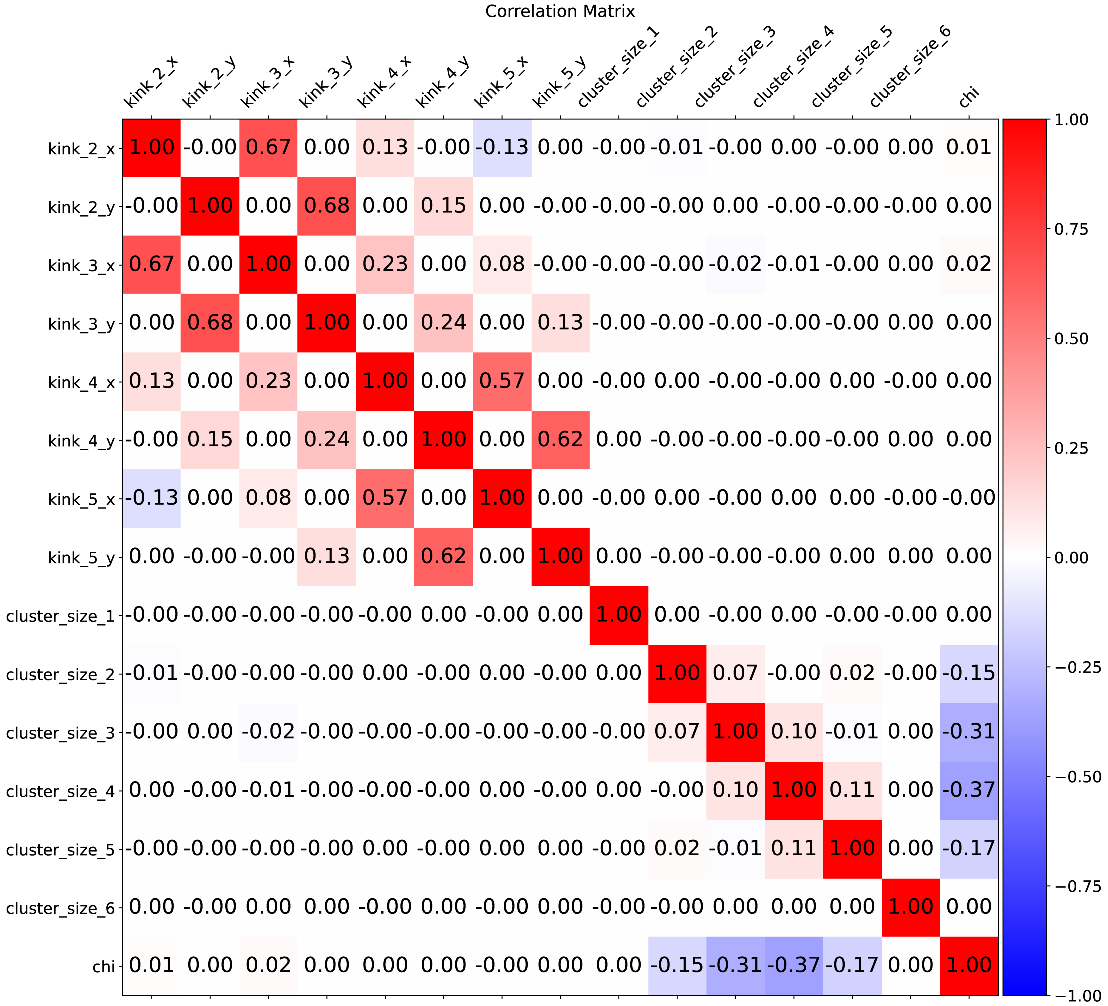

	kink_2_x	kink_2_y	kink_3_x	kink_3_y	kink_4_x	kink_4_y	kink_5_x	kink_5_y	cluster_size_1	cluster_size_2	cluster_size_3	cluster_size_4	cluster_size_5	cluster_size_6	chi
kink_2_x	1.00	-0.00	0.67	0.00	0.13	-0.00	-0.13	0.00	-0.00	-0.01	-0.00	0.00	-0.00	0.00	0.01
kink_2_y	-0.00	1.00	0.00	0.68	0.00	0.15	0.00	-0.00	-0.00	-0.00	0.00	-0.00	-0.00	-0.00	0.00
kink_3_x	0.67	0.00	1.00	0.00	0.23	0.00	0.08	-0.00	-0.00	-0.00	-0.02	-0.01	-0.00	0.00	0.02
kink_3_y	0.00	0.68	0.00	1.00	0.00	0.24	0.00	0.13	-0.00	-0.00	-0.00	-0.00	-0.00	0.00	0.00
kink_4_x	0.13	0.00	0.23	0.00	1.00	0.00	0.57	0.00	-0.00	0.00	-0.00	-0.00	0.00	-0.00	0.00
kink_4_y	-0.00	0.15	0.00	0.24	0.00	1.00	0.00	0.62	0.00	-0.00	-0.00	-0.00	-0.00	0.00	0.00
kink_5_x	-0.13	0.00	0.08	0.00	0.57	0.00	1.00	0.00	-0.00	0.00	-0.00	0.00	0.00	-0.00	-0.00
kink_5_y	0.00	-0.00	-0.00	0.13	0.00	0.62	0.00	1.00	0.00	-0.00	-0.00	-0.00	0.00	0.00	0.00
cluster_size_1	-0.00	-0.00	-0.00	-0.00	-0.00	0.00	-0.00	0.00	1.00	0.00	-0.00	0.00	-0.00	-0.00	0.00
cluster_size_2	-0.01	-0.00	-0.00	-0.00	0.00	-0.00	0.00	-0.00	0.00	1.00	0.07	-0.00	0.02	-0.00	-0.15
cluster_size_3	-0.00	0.00	-0.02	-0.00	-0.00	-0.00	-0.00	-0.00	-0.00	0.07	1.00	0.10	-0.01	0.00	-0.31
cluster_size_4	0.00	-0.00	-0.01	-0.00	-0.00	-0.00	0.00	-0.00	0.00	-0.00	0.10	1.00	0.11	0.00	-0.37
cluster_size_5	-0.00	-0.00	-0.00	-0.00	0.00	-0.00	0.00	0.00	-0.00	0.02	-0.01	0.11	1.00	0.00	-0.17
cluster_size_6	0.00	-0.00	0.00	0.00	-0.00	0.00	-0.00	0.00	-0.00	-0.00	0.00	0.00	0.00	1.00	0.00
chi	0.01	0.00	0.02	0.00	0.00	0.00	-0.00	0.00	0.00	-0.15	-0.31	-0.37	-0.17	0.00	1.00

Figure 6.7: Pearson correlation coefficients of all input features of the classifier. Scattering angles on the first and last tracking planes are ill-defined and were therefore excluded as input features.

Four hyperparameters are optimised in this study, as each additional optimised parameter increases both complexity and computational time significantly. The four hyperparameters are explained below:

- **Learning rate** (η): Scales the feature weights during training to balance the optimisation of the BDTs and the prevention of overfitting. A learning rate that is too high may lead to overfitting, while a lower rate allows for more gradual and stable convergence.

- **Maximum tree depth**: Defines the maximum depth of the trees in the BDT. Greater depth allows the model to capture more complex patterns but increases the risk of overfitting, whereas insufficient depth may prevent the model from capturing the complexity required for accurate track identification.
- **Minimum loss reduction** (γ): Represents the minimum decrease in the loss function required to make a further partition on a leaf node. Larger values make the model more conservative by avoiding splits that only offer marginal improvements, thus helping to control complexity.
- **Minimum sum of instance weights** (Θ): Specifies the minimum total weight needed in a child node for a split to occur. This parameter limits unnecessary splitting and contributes to regularisation by preventing the model from focusing too much on small, potentially noisy subsets of the data.

A grid search is performed to find the optimal configuration for these four hyperparameters using the Python [93] library Scikit-learn [94]. To limit computational time, four commonly used values were selected for each hyperparameter. All values considered in the grid search are listed in Table 6.1.

Table 6.1: List of hyperparameter values optimised in a grid search.

Tree depth	η	γ	Θ
3	0.05	0.5	1
4	0.1	1	25
5	0.3	2	50
6	0.7	5	

A 5-fold cross-validation is performed to quantify the performance of the classifier for each combination of hyperparameter values. This means that the training dataset is divided into five equally sized subsets, referred to as folds. Four of these folds are used for training, while the fifth is reserved for evaluation. Each of the five folds serves as the evaluation set once, resulting in five evaluations for each hyperparameter configuration. The scoring function used to assess the results is the area under the receiver operating characteristic (ROC) curve, known as the AUC. ROC curves are widely used graphical representations for evaluating binary classification models. It illustrates the trade-off between the true positive rate (TPR) and the false positive rate (FPR) at various threshold settings of the classifier. The TPR measures the proportion of actual positives correctly identified by the model (t_p), while the FPR quantifies the proportion of actual negatives that were incorrectly classified as positives (f_p). In the context of the track identification problem, the TPR and FPR represent the proportions of real and fake tracks that were classified as real, respectively:

$$\mathrm{TPR} = \frac{t_\mathrm{p}}{t_\mathrm{p} + f_\mathrm{n}} \tag{6.18}$$

$$\mathrm{FPR} = \frac{f_\mathrm{p}}{f_\mathrm{p} + t_\mathrm{n}} \tag{6.19}$$

The false negative f_n and true negative t_n represent the number of real and fake tracks that were classified as fake. Consequently, the area under the ROC curve provides a single metric that summarises the overall performance of the classification model across all possible thresholds. The AUC ranges from 0.5 to 1.0, where 0.5 corresponds to random guessing and 1.0 represents a perfect classifier.
For the grid search, the highest mean AUC of the evaluation fold, $\mathrm{AUC}_\mathrm{mean} = 0.9956(2)$, is achieved with the following hyperparameter configuration: tree depth $= 6$, $\eta = 0.3$, $\gamma = 5$, and $\mathit{\Theta} = 1$. These values will be used for training the classifier and for classifying the test dataset.

Results for the training and test datasets are presented in the following to evaluate the performance of the classifier and assess the effect of overtraining. The classifier outputs normalised PDFs of the reconstructed tracks for both the training and test datasets, as shown in Figure 6.8. Here, the PDF represents the assigned probability of each track being real. The PDF of the real tracks is noticeably broader than that of the fake tracks, with some real tracks assigned probabilities as low as approximately 90 %. This indicates that the classifier encounters slightly greater challenges in correctly classifying real tracks as real. Nevertheless, the majority of both real and fake tracks in the training and test datasets were classified with high confidence. Small differences, within the range of ± 0.1, between the output PDFs of the training and test datasets for real and fake track classification suggest that the classifier did not suffer from significant overtraining.

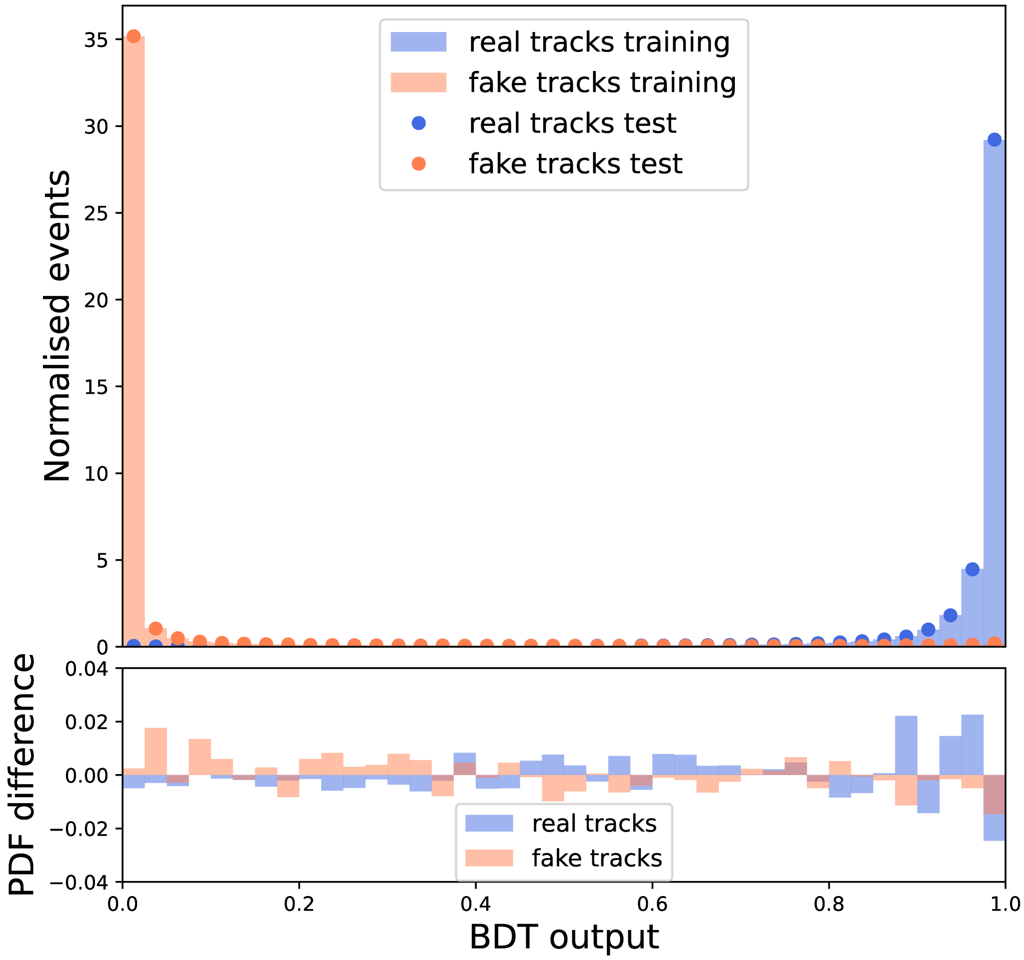

Figure 6.8: Track classification distribution of labelled real and fake tracks of the trained classifier. Results of the training and test datasets are shown, as well as their difference. The goal of the classifier is to assign high probabilities to real tracks and low probabilities to fake tracks.

The separation power of the input features can be quantified by their total number of splits, referred to as the feature importance (F Score) score. Figure 6.9 shows the F Score score for all input features. The χ^2/ndof is the most frequently used feature for splits by the classifier. Since χ^2/ndof quantifies the goodness of the track fit, it is expected to be highly sensitive to tracks with incorrect cluster combinations. Similarly, the scattering angles are used only slightly less often, as real high-energy particles are expected to exhibit small scattering angles. In contrast, all features related to the cluster size have a low impact on track separation.

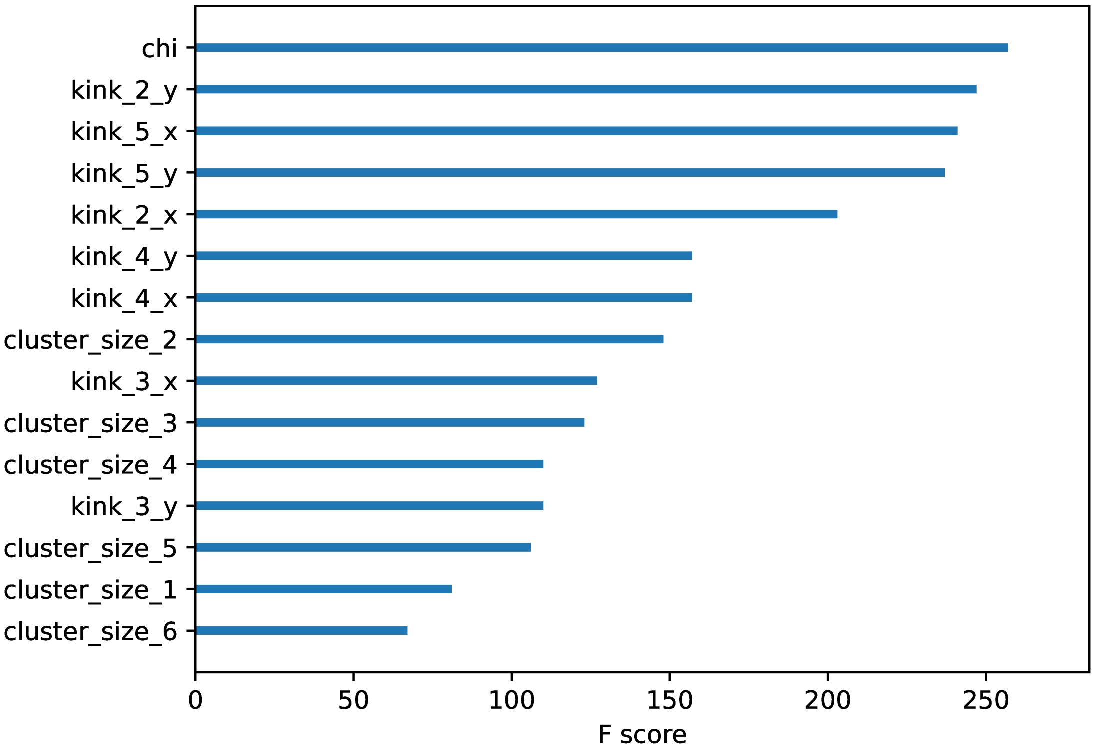

Figure 6.9: Feature importance scores of all features that are fed into the classifier.

The differences in the input features between real and fake tracks are highlighted in Figure 6.10. Here, the χ^2/ndof, the cluster sizes and the scattering angles in the x- and y-directions are shown for real and fake tracks as representative examples. While the cluster size distributions are similar for real and fake tracks, the χ^2/ndof and the scattering angles exhibit clear distinctions. Although small scattering angles are common for both types of tracks, scattering angles above $\phi = 0.5\,\mu\text{rad}$ are almost exclusively characteristic of fake tracks. The same applies to large χ^2/ndof values. The number of fake tracks with small χ^2/ndof values is significantly lower than for real tracks, which explains the strong separation power of this feature.
The predictive power of the classifier is evaluated using the ROC curve, shown in Figure 6.11a. Each working point on the ROC curve is determined by a threshold on the probability of a track being classified as real. All three datasets yield compatible results, with the TPR reaching values close to one even for small FPRs, and an AUC of 0.994 achieved for the test dataset.

To accurately estimate the efficiency of DUTs in a beam test, filtering out fake tracks is of high priority. Since the FPR depends on the number of true negatives, a low FPR can also result from the rejection of a large number of fake tracks. However, the efficiency of a pixel detector is not influenced by the number of rejected fake tracks, but rather by the number of accepted real and fake tracks. Therefore, a more appropriate metric for this analysis is the precision, which depends solely on the positive predictions:

$$\text{Precision} = \frac{t_\mathrm{p}}{t_\mathrm{p} + f_\mathrm{p}} \tag{6.20}$$

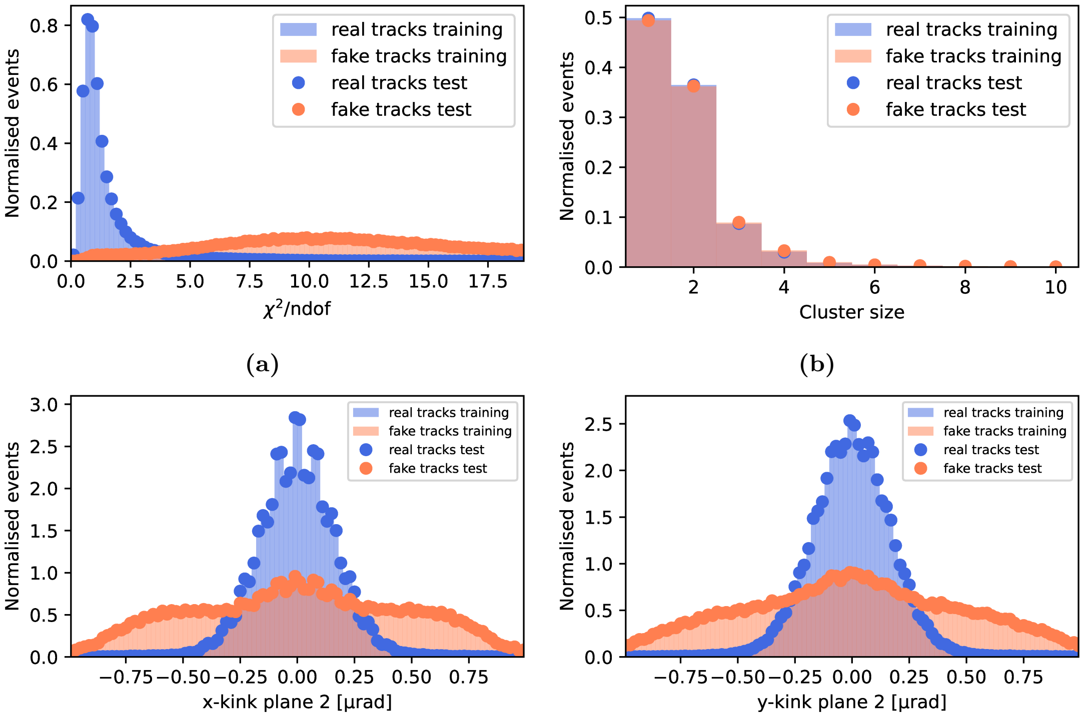

(a) **(b)** **(c)** **(d)**

Figure 6.10: Distributions of the χ^2/ndof (a), the cluster size (b) and the scattering angles in x- and y-directions (c and d) for real and fake tracks.

The precision quantifies the ability of the classifier to correctly identify real tracks while minimising the misclassification of fake tracks. It is commonly compared to the TPR, referred to as recall in this context. Figure 6.11b shows the precision-recall curve for the three datasets. Notably, high precision values are achieved while maintaining a high recall. This indicates that the classifier successfully identifies most real tracks while correctly classifying fake tracks across a range of probability thresholds.

These results demonstrate that the classifier is highly effective in addressing the track multiplicity challenge in high-density beams. However, alternative approaches may yield similar results with significantly less computational complexity. A simpler method would be to rely solely on the χ^2/ndof feature, which exhibited the strongest separation power among all investigated features. The Corryvreckan software provides two one-dimensional filtering strategies based on this feature: (1) removing all tracks with a χ^2/ndof value exceeding a predefined threshold, and (2) retaining only the track with the lowest χ^2/ndof value in each event. These two approaches are examined in the following sections and compared to the classifier to determine the most suitable method for future beam test analyses.

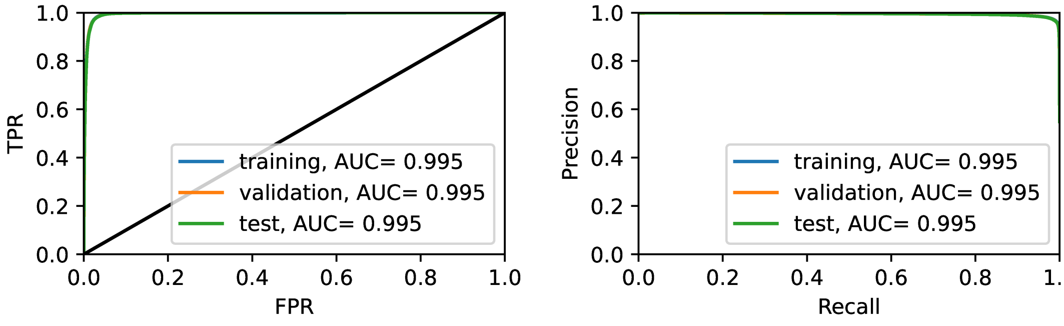

(a) (b)

Figure 6.11: a) ROC curve and AUC of the training, validation and test datasets. The black diagonal line represents the performance of a random guesser for comparison. b) Precision-recall curve and AUC of the three datasets.

6.7 Investigation of χ^2-based Cuts for Track Identification

Evaluating the separation power of the χ^2/ndof feature alone is performed in a similar manner to the BDT. The corresponding precision-recall curves, shown in Figure 6.12a, are now determined by applying arbitrary thresholds to the χ^2/ndof values. This allows for the selection of an optimal χ^2/ndof threshold for the identification of fake tracks.

The precision-recall curves exhibit similar behaviour across all three datasets, although their AUC is approximately 0.018 lower compared to the BDT results. A noticeable discrepancy between the two approaches emerges at high recall values, indicating that the BDT is more effective at identifying fake tracks while retaining a greater number of real tracks. However, up to recall values of approximately 0.8, the precision achieved using the χ^2/ndof feature alone is not significantly lower. This demonstrates that a one-dimensional cut on χ^2/ndof is a viable alternative for many track reconstruction applications in high-intensity beam tests.

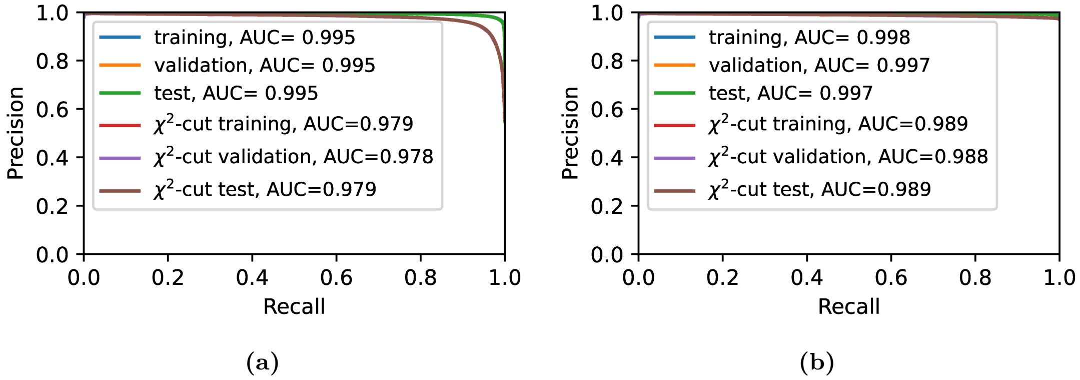

Figure 6.12: a) Precision-recall curve and AUC of the training, validation and test datasets for arbitrary thresholds of the χ^2/ndof value. b) Precision-recall curve and AUC of the same datasets when only the track with smallest χ^2/ndof value per event is retained. The results of the BDT are included as a comparison in both plots.

Another approach to optimising fake track identification is the strict rejection of all but one track per event, specifically the track with the smallest χ^2/ndof value. Corryvreckan directly supports this method within its Tracking4D module. The precision-recall curves comparing the machine learning approach with the χ^2/ndof-cut method are shown in Figure 6.12b. Significantly higher precision values are achieved for high recall values, particularly when using only the χ^2/ndof feature for track separation. Although the high recall indicates that most real tracks are retained, a substantial number of tracks are discarded with this approach. In the simulations, the track multiplicity was approximately 300 tracks per event, meaning that more than 99 % of real tracks are lost. While the rejection of fake tracks is a high priority for reliable beam test analysis, preserving a sufficient number of real tracks is essential for accurate results. Consequently, the unique track selection approach will not be used in the standard beam test analysis presented in this thesis.

6.8 Track Identification of Beam Test Data

The particle density in the CERN SPS beam test facility is typically significantly lower than 200 particles per recorded event, which corresponds to 230 µs in this setup. While the simulation with such a high-density beam was chosen as a benchmark for the general problem, beams with up to 150 particles are occasionally used at CERN SPS beam tests to assess detector performance.
To compare the results obtained from the simulated data with real beam test data, a high-intensity beam test from October 2021 is considered. This campaign was conducted to investigate single chip cards (SCCs) and quad modules equipped with the RD53a prototype readout chip. Several runs within this campaign featured particularly high particle rates, which were used for this analysis. The telescope setup consisted of the same number of tracking planes, comprising six Mimosa26 sensors. No time reference plane was utilised during reconstruction, as it removes a significant portion of reconstructed tracks. Since the focus of this study is to benchmark track reconstruction in high-density beams, no additional constraints on timing were applied.

Before tracks can be properly reconstructed, the detector geometry must be aligned with high precision to prevent a decrease in the quality of reconstructed tracks. The cluster and track multiplicities after successful alignment are shown in Figure 6.13 in comparison to the simulated training dataset.
For the beam test data, the cluster multiplicity exhibits a broader distribution with significantly fewer clusters per event. This suggests that the particle density of the beam during data taking was lower than in the simulation, which directly translates to a lower track multiplicity. Similar to the simulated data, there is no noticeable shift in the cluster multiplicity distribution between plane 1 and plane 6 for the beam test data, indicating that only a negligible number of particles partially traversed the telescope. The number of fake tracks is expected to be significantly lower than in the simulation, though they may still not be entirely negligible.
The χ^2/ndof and scattering angle distributions of the second tracking plane are shown in Figure 6.14. Discrepancies between these features and those from the simulated test dataset are evident. The long tail of large χ^2/ndof values is significantly reduced for tracks from the beam test data. This can be attributed to the substantially lower track multiplicity, which results in fewer fake tracks, as these contribute almost exclusively to the larger χ^2/ndof values. For similar reasons, the beam test data exhibits fewer scattering angles with $|\Phi| > 0.5\,\mu\text{rad}$. Additionally, no sub-peaks are present in the scattering angle distribution, which is attributed to the absence of misalignment in the simulation.

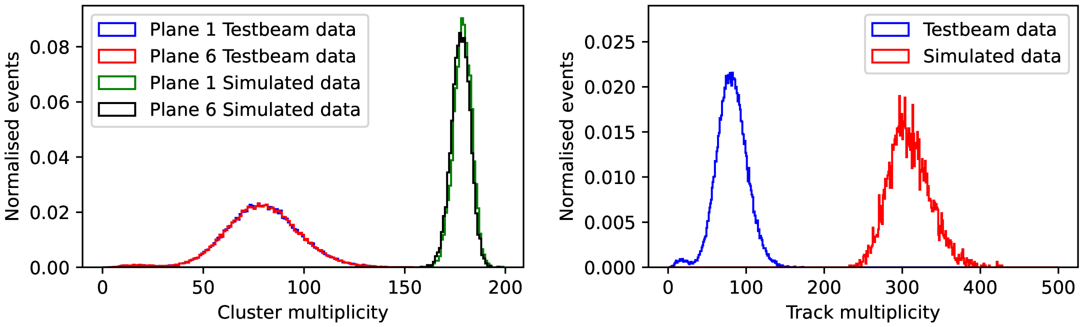

(a) (b)

Figure 6.13: Normalised cluster (a) and track (b) multiplicities for 50k events of the beam test data and 5k events of simulated data.

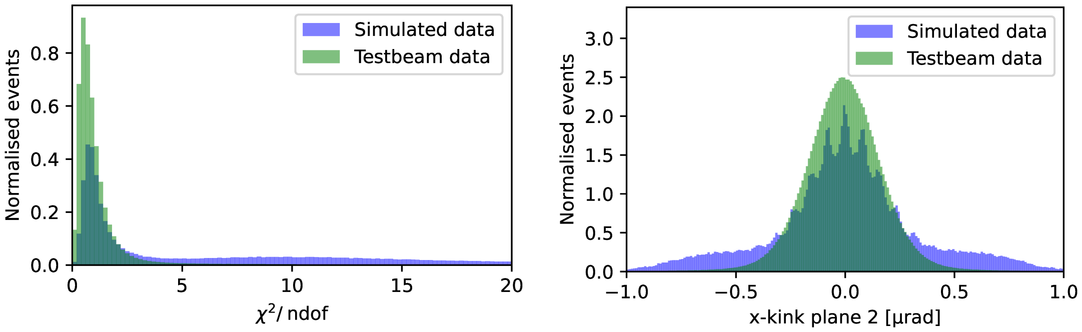

(a) (b)

Figure 6.14: The χ^2/ndof (a) and scattering angle (b) distributions of the reconstructed tracks from run 1771 of the October 2021 beam test. The same features from the simulated test dataset are shown for comparison.

The track classification probabilities provided by the trained BDT for the reconstructed tracks of the beam test data are shown in Figure 6.15. Fewer than 12.4 % of all tracks have a probability of less than 50 % of being classified as real. The distribution of high probabilities for real tracks in the beam test data follows a similar pattern to that observed in the simulation data. However, due to the absence of a large number of fake tracks, the probability distributions of the beam test data generally exhibit a higher number of normalised events at high probabilities of tracks being real. In comparison, applying a χ^2/ndof<3 cut results in 6.1 % of all tracks being discarded. While this method likely filters out more real tracks than the BDT classifier, it is effective in filtering out most fake tracks, due to the tail towards higher χ^2/ndof values.

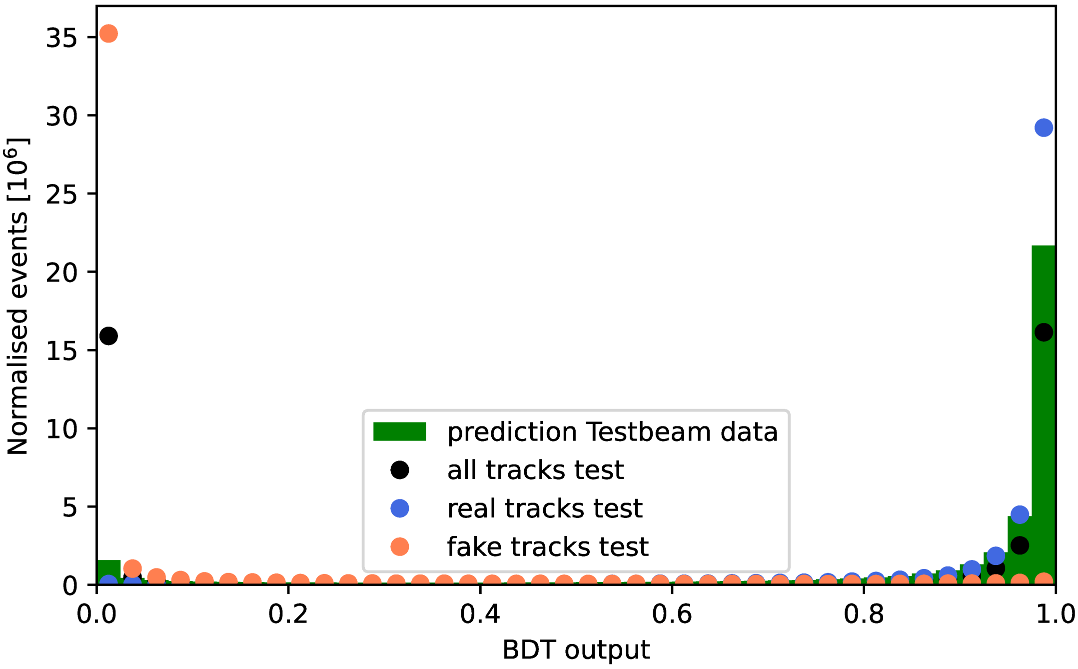

Figure 6.15: Track classification distribution of the reconstructed tracks of the beam test data. The labelled real and fake tracks of the simulated test dataset are shown for comparison.

High-intensity beam tests and beam test simulations were conducted to investigate the influence and identification of fake tracks that could impair the DUT performance. The separation of real and fake tracks in high-intensity beam tests proves to be a straightforward task. Simulations have demonstrated that classification remains effective even at densities exceeding those currently observed in ITk beam tests. If a classifier is required, both the machine learning approach and a simple cut on the χ^2/ndof have proven to be highly effective. This also indicates that increasing beam density is a viable option for enhancing data-taking rates in beam tests without compromising the quality of reconstructed tracks.

For the analysis of beam test data in the following chapters, a cut on the χ^2/ndof was chosen due to its simplicity and the better comparability of different analyses.

7 Investigation of the ATLAS ITk Quad Module Performance in Beam Tests

Numerous ITk pixel test beam campaigns have been conducted to thoroughly evaluate the performance of planar and 3D ITk pixel modules. The key quantities of interest include the average efficiency of the detector module, in-pixel efficiency, spatial resolution, cluster size distribution, and the ratio of masked pixels to the total number of pixels. Each of these quantities and their significance will be discussed in this chapter for several planar quad modules. Additionally, the interchip region of the quad modules will be analysed separately to assess its efficiency.
Recent ITk pixel test beam results for 3D sensors are presented in [95]. The data underlying the results in this chapter were collected between 2022 and 2024 and include the first-ever beam test measurements of quad modules with the ITkPixV2 readout chip.

7.1 Beam Test Setup

All results presented in this chapter are based on data collected using the ACONITE telescope, which is described in more detail in Section 6.1. In addition to the FE-I4 time reference plane, which is mounted directly behind the second Mimosa26 plane, an ITkPixV1.1 SCC plane is installed inside the cold box for the same purpose. Since either of the time reference planes occasionally experienced operational issues, having two ensured more stable data-taking conditions.
Powering quad modules increases their temperature by several tens of kelvin, which the air-cooled cold box alone cannot sufficiently counteract. To address this, additional cooling circuits using oil and alcohol were developed over multiple test beam campaigns. As a result, the quad modules were operated and studied under a wide range of temperatures. While the target operating temperature was around −35 °C, temperatures often stabilised between −30 °C and 0 °C.

7.2 Investigated Planar Quad Modules

The performance of nine quad modules was investigated in the scope of this thesis. All modules have an active thickness of 150 µm, and their properties are listed in Table 7.1. Most of the modules utilise the ITkPixV1.1, as the newer ITkPixV2 has only been available for ITk beam tests since 2024.
Two different irradiation levels were studied: $2 \cdot 10^{15}\,\mathrm{n_{eq}/cm^2}$ and $4.3 \cdot 10^{15}\,\mathrm{n_{eq}/cm^2}$. These fluences correspond to the expected radiation levels in the second and third layers of the ITk over its operational lifetime [34]. The modules did not undergo significant annealing after being irradiated.

The modules named KEK and ADV were hybridised by KEK [96] and Advafab [97], respectively, with sensors manufactured by HPK. All modules utilising Micron sensors were hybridised by Advafab and Fraunhofer IZM [98].
The bias structure of the Micron modules operates via a bias dot, whereas the HPK modules utilise a polysilicon layer, as described in Section 4.2.
Several other modules, for which stable operation could not be achieved, are excluded from this analysis. All modules were tuned to a threshold of 1 ke to balance detection efficiency and noise suppression. In earlier beam tests, significant operational issues with planar quads led to an increase in the threshold to 1.5 ke and 2 ke, at which the modules were stable enough for data taking. This applies to the KEKQ9 and KEKQ16 modules in this study. Bias voltages in the range of $0 - 120\,\mathrm{V}$ and $100 - 600\,\mathrm{V}$ were applied to unirradiated and irradiated modules, respectively. Since the depletion voltage of the modules during operation depends on the received fluence, investigating module performance across a wide range of voltages is crucial.

Table 7.1: List of the investigated ITk quad modules including their names, vendors, FE version and received fluences.

Name	**Vendor**	**Front-End**	**Irradiation**
KEKQ9	HPK	ITkPixV1.1	0
KEKQ16	HPK	ITkPixV1.1	$4.3 \cdot 10^{15}\,\mathrm{n_{eq}/cm^2}$
HPKQV2	HPK	ITkPixV2	0
ADVQV2	HPK	ITkPixV2	0
Q18	Micron	ITkPixV1.1	0
Q19	Micron	ITkPixV1.1	0
Q8	Micron	ITkPixV1.1	$2 \cdot 10^{15}\,\mathrm{n_{eq}/cm^2}$
Q12	Micron	ITkPixV1.1	$2 \cdot 10^{15}\,\mathrm{n_{eq}/cm^2}$

7.3 Masking of Quad Modules

To ensure that individual pixels are not malfunctioning, either by being too noisy or unresponsive after tuning, several mask scans are performed. These scans send multiple trigger signals and determine how often each pixel responds while not being exposed to the particle beam. If a pixel fires too often, it is masked to prevent issues during data taking and to avoid impairing the module's efficiency. Unresponsive pixels are identified by inducing a charge into each pixel via a capacitor. A new tuning and masking procedure is carried out for each bias voltage configuration to ensure that the modules are configured for optimal performance. During data taking, the goal was to collect one million events per tuning to minimise statistical fluctuations while still completing multiple batches of DUTs within a single beam test.
Since the track reconstruction framework, Corryvreckan, does not receive the masking information from the tuning, it cannot distinguish between pixels that were intentionally masked and those that did not register a hit. To prevent a misrepresentation of the module's performance, Corryvreckan applies a separate masking process, where all pixels that did not receive a hit are masked. No additional masking for noisy pixels is performed by the software.

Figure 7.1 shows a typical cluster map and the corresponding mask map of the ADVQV2 quad module. In the cluster map, the centres of clusters of multiple pixels determine the corresponding pixel bin entry. The cutoff of the beam spot marks the edge of the sensitive scintillator area. Due to the larger area, pixels in the interchip region register more hits statistically, which highlights their position in the cluster map.
Only a few pixels within the beam spot are masked, which is expected since the mask map labels all pixels without hits as masked. Many pixels outside the sensitive scintillator area still register a few hits, as multiple particles per event may traverse the telescope, and a single interaction with the scintillator material is sufficient for all hits to be read out.
The mask map can vary significantly depending on the received fluence of the module and its tuning. To accurately assess a module's performance, the number of masked pixels must be considered. While a module's efficiency may appear high, a significant number of masked pixels could simply conceal suboptimal performance.
Figure 7.2 shows the ratio of masked pixels to the total number of pixels for unirradiated and irradiated quad modules at different applied bias voltages. Systematically disabled areas or entire faulty readout chips are excluded from this analysis, as they typically indicate operational issues during the beam test or physical damage rather than the actual module performance. The ratio includes only the pixels masked during tuning, excluding those additionally masked by Corryvreckan due to the absence of registered hits. For unirradiated modules, the percentage of masked pixels remains below 1 % across all bias voltages. This is expected, as unirradiated modules do not suffer from radiation

damage and therefore exhibit greater stability. Fluctuations in the number of masked pixels, such as the one observed for Q18 at a bias voltage of 40 V, arise from suboptimal tuning of one of the four chips but do not significantly impact the overall performance of the module at this order of magnitude.

For irradiated modules, the percentage of masked pixels ranges from 0 to 4 %, with a general trend of increasing masked pixels at higher bias voltages. The relatively low number of masked pixels demonstrates that most pixels remain functional after irradiation, allowing for a reliable evaluation of both average and in-pixel efficiency. While the KEKQ16 module exhibits the lowest percentage of masked pixels, only one chip was enabled during data taking due to operational issues. Additionally, the tuned threshold influences the masking ratio significantly, as seen in the lower number of masked pixels for the KEKQ9 and KEKQ16 modules in comparison to the other modules.

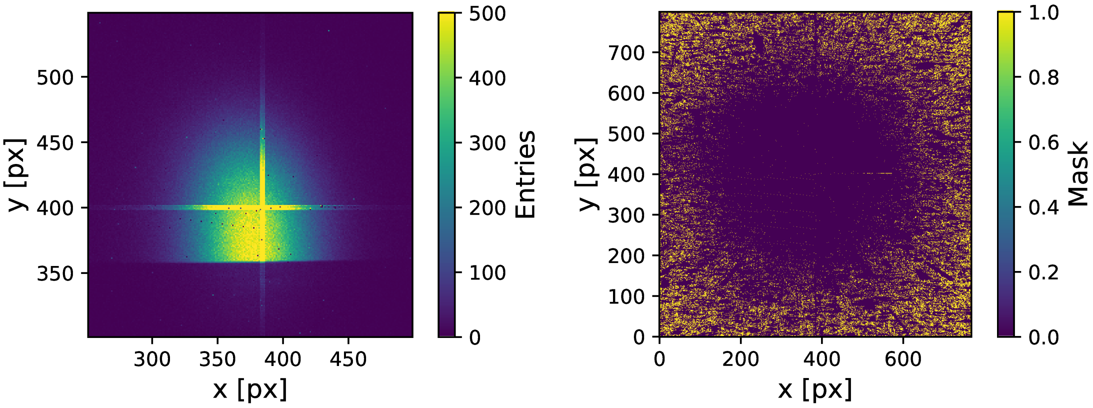

(a) **(b)**

Figure 7.1: a) Cluster map of the ADVQV2 quad module at a bias voltage of 80 V, zoomed in to emphasise the beam spot and the interchip region. b) Mask map of the ADVQV2 quad module from the same run. Masked pixels are labelled as 1 and include all pixels that did not register a hit.

Another key quantity in the analysis is the cluster size distribution of pixel hits. The cluster sizes provide insight into the spread of charge in the sensor, which depends on the tuned pixel threshold, the module's orientation relative to the beam, and the received fluence of the module. A particle beam is more likely to hit multiple pixels in tilted modules, as the effective sensor area in relation to the beam incidence is reduced. This is the typical scenario for ATLAS ITk pixel modules, where non-perpendicular particle incidence is expected. Additionally, the presence of a magnetic field in the ATLAS detector bends particle trajectories, increasing the likelihood of a non-straight traversal through the sensor volume.

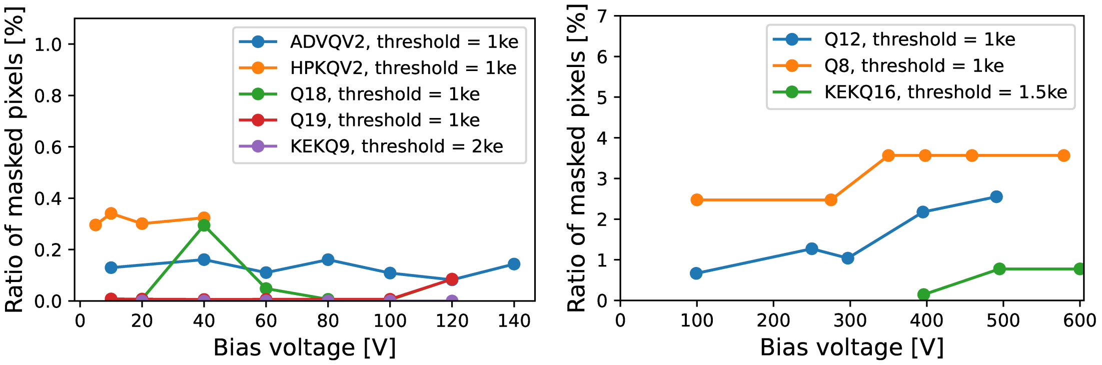

(a) **(b)**

Figure 7.2: Ratio of masked pixels to the total number of pixels for unirradiated (a) and irradiated (b) quad modules at different bias voltages.

Figure 7.3a shows the normalised cluster size distribution for unirradiated and irradiated HPK and Micron modules. Further measurements were conducted with a 15° tilt with respect to the beamline for two quad modules, and their results are presented in Figure 7.3b. Irradiated modules tend to exhibit a slightly lower number of clusters with sizes of two or more pixels. This can be attributed to radiation damage in the silicon, which introduces charge carrier traps that impair charge propagation. This effect is more pronounced in tilted modules, where the unirradiated ADVQV2 module shows a significantly higher average number of pixels per cluster compared to the irradiated Q8 module. The increased pixel threshold of 1.5 ke in the KEKQ16 module does not significantly affect the cluster size distribution. Since approximately 7.5 ke are generated on average by a 120 GeV particle in 150 µm thick silicon, a difference of 0.5 ke in the threshold has a minor impact on the cluster size.

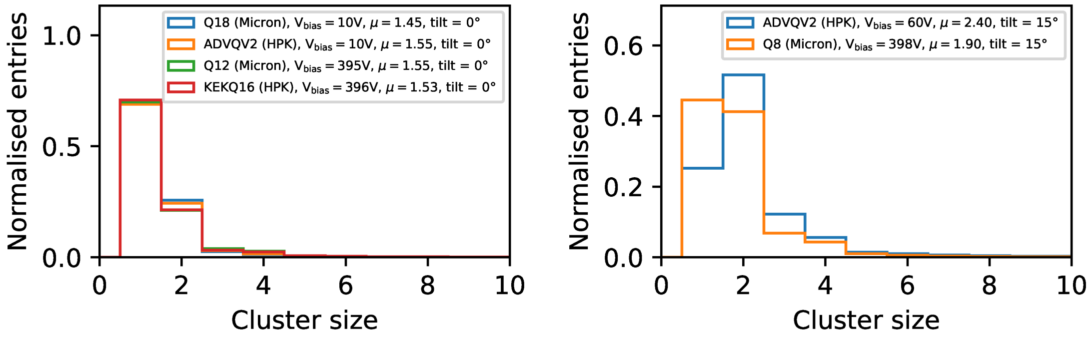

(a) **(b)**

Figure 7.3: Cluster size distribution of HPK and Micron quad modules for perpendicular (a) and tilted (b) beam incidence. Here, μ denotes the mean of the distribution.

7.4 Spatial Resolution of Quad Modules

To accurately evaluate the performance of the DUTs using reconstructed tracks, the sensor geometry in the software must be aligned with high precision. Misalignment can result in missed cluster associations with tracks or cause in-pixel patterns to shift and distort. The quality of the DUT alignment can be assessed by examining the corresponding residual distributions. The shape of these distributions provides a measure of alignment precision and also serves as an indicator of the spatial resolution of the pixels, as discussed in Chapter 6.3.

For track reconstruction, the GBL algorithm was used to provide an accurate approximation of the actual particle trajectory. The corresponding χ^2/ndof distribution after successful alignment is shown in Appendix A.1. A radius of 100 µm is defined for associating reconstructed tracks with cluster centres on the DUT. This distance corresponds to twice the pixel pitch of the DUTs, ensuring that nearly straight particle tracks are correctly linked to cluster centres while keeping the likelihood of false associations between tracks and clusters low.
Figure 7.4 shows the normalised residual distribution in the x-direction for unirradiated and irradiated HPK and Micron modules with similar applied bias voltages. Only clusters with a size of 1 are considered, so the standard deviation of the distributions is expected to follow $\sigma = \text{pixel pitch}/\sqrt{12} \approx 14.43\,\mu\text{m}$. The measured standard deviations for the DUTs range from 13 to 17 µm, which gives a discrepancy of approximately $-1.5\,\mu\text{m}$ and $+2.5\,\mu\text{m}$. The track resolution of the ACONITE telescope is usually in the range of $2-3\,\mu\text{m}$ [72], depending on the exact geometry of the tracking planes. Consequently, the measured standard deviations are consistent with expectations after successful alignment.

For proper alignment, the mean of the distribution should be close to 0 µm. This condition is met for all modules except KEKQ16, which exhibits a noticeable deviation of 5.53 µm. This discrepancy is attributed to the limited active area of the module during data taking, as only a single chip was partially enabled, despite a comparable number of a few 100k associated clusters for all investigated DUTs. This poses a greater challenge for the alignment algorithm to converge to the accurate geometry. The corresponding standard deviation of the KEKQ16 module is noticeably larger in comparison to the other modules for the same reason. For further performance evaluation, such as assessing module efficiency, this deviation causes no major issue, since the matching radius is significantly larger than the translational shift. Overall, these distributions confirm that the alignment process was successful and that the pixels exhibit the expected spatial resolution.

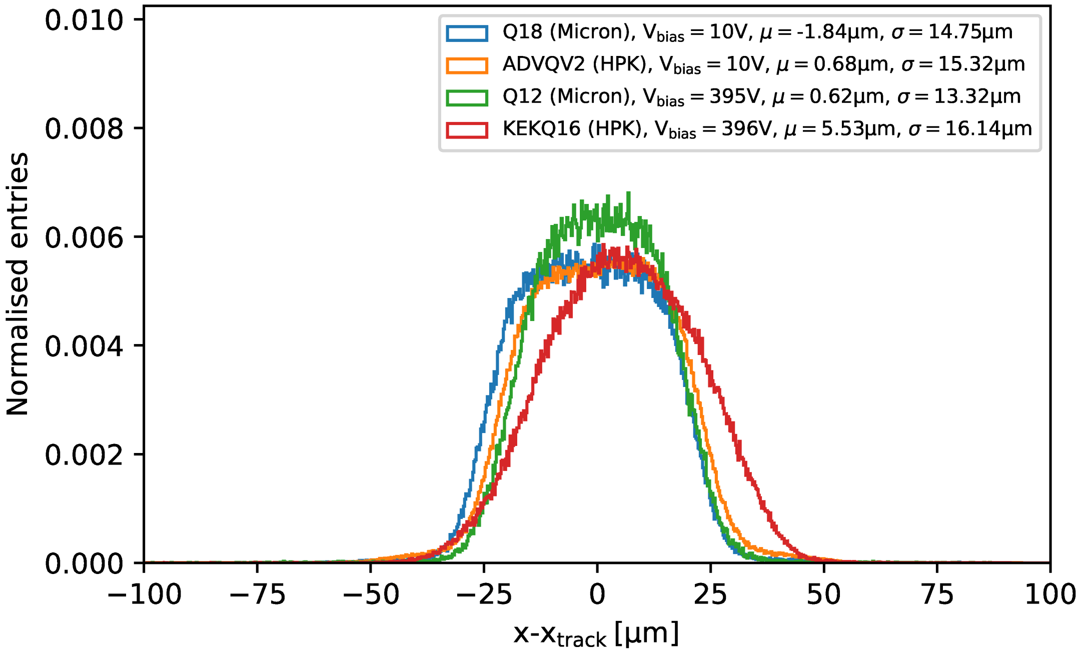

Figure 7.4: Residual distribution of 1-pixel clusters for unirradiated and irradiated HPK and Micron quad modules.

The four middle rows and columns of each quad consist of special long pixels that make up the interchip region as described in Section 2.4.2 and illustrated in Figure 7.5. The performance of these pixels has to be investigated particularly to ensure that particle hits are properly detected in that region. Normalised interchip pixel residuals for an unirradiated HPK and an irradiated Micron sensor are shown in Figure 7.6.

In these plots, the horizontal, vertical, and centre pixels are shown, which have long pixel pitches in both directions. As the interchip region consists of only four rows or columns and a centre of 16 pixels in total, the number of associated tracks is significantly lower compared to the total number of associated tracks of the pixel modules. Depending on the interchip region and the sensor for which the data was taken, this number ranges from 800 to 30k. This is more clearly seen for the residual of the centre pixels of the Q8 module, which fluctuates significantly. The bin width has been increased to compensate for even larger fluctuations. The bottom and left interchip regions are shown, as they cover a larger portion of the beam spot and therefore exhibit lower statistical uncertainties.
The standard deviation of $\sigma = \text{long pixel pitch}/\sqrt{12} \approx 28.87\,\mu\text{m}$ is achieved with good precision, as seen from the box-shaped distribution with a width of approximately 100 µm. Thus, the long pixels achieve the expected spatial resolution. Due to the very limited sensitive area of the irradiated KEKQ16 module, no data from the interchip region could be presented for an irradiated HPK sensor.

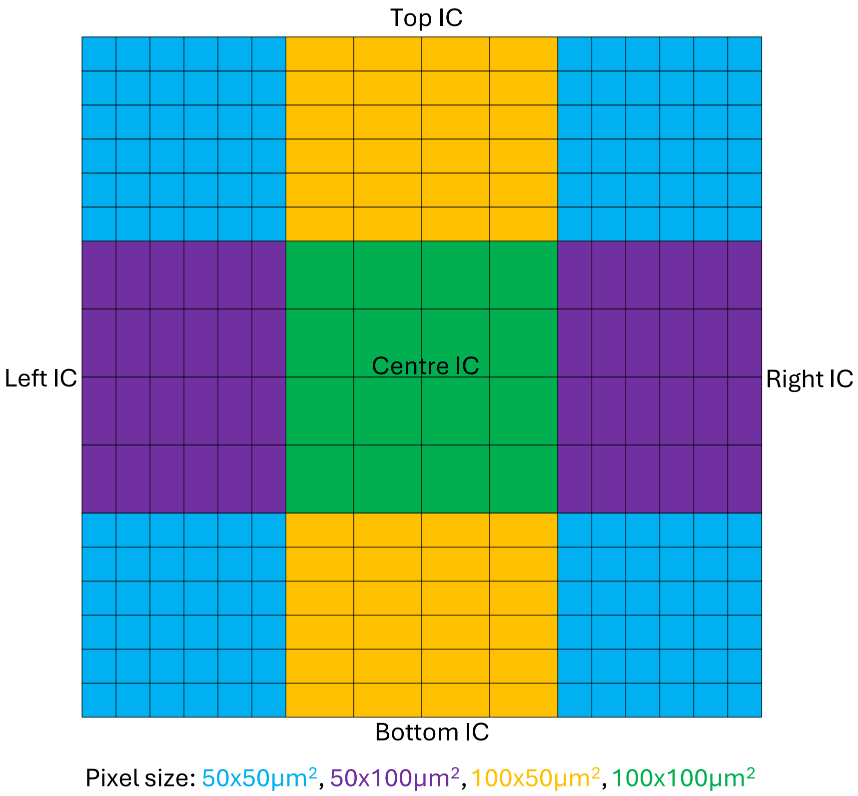

Figure 7.5: Pixel sizes of the different interchip (IC) regions of a planar quad module.

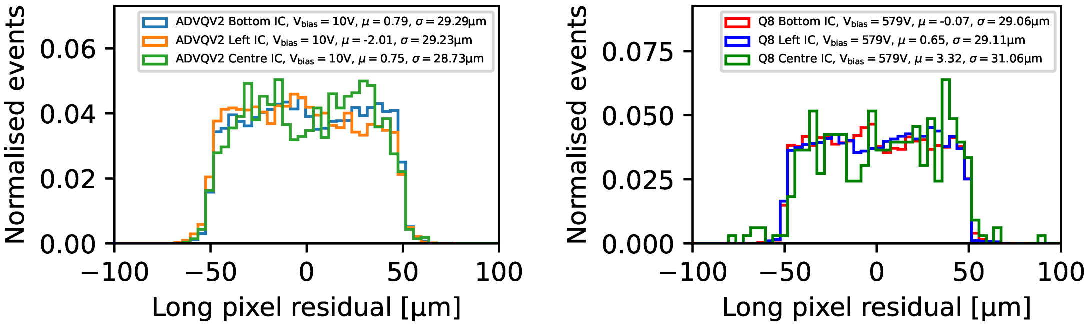

(a) **(b)**

Figure 7.6: Interchip residuals of the long pixel direction for a vertical, horizontal and the centre region of an HPK (a) and a Micron (b) quad module.

7.5 Efficiency of Quad Modules

The efficiency of the individual pixels has to be investigated to ensure that no large-scale issues with the readout chip or hardware-related damage impair the performance of the module. Figure 7.7 shows the pixel efficiency map of an unirradiated and irradiated HPK and Micron quad module. The depicted shapes and sizes of the regions strongly depend on the beam spot size of the respective beam test, which varied in different campaigns. The efficiency map of the ADVQV2 and the Q12 were taken in the same beam test campaign. Therefore, they exhibit very similar shapes. Both unirradiated modules show no signs of large-scale inefficiencies across all four operated readout chips. The irradiated KEKQ16 module had only one enabled chip, which was partially operational. This is evident from the sudden drop in efficiency for columns exceeding pixel 490. Furthermore, the constrained trigger window defined by the scintillators restricted the efficiency investigation to a limited area of the sensor.

The efficiency map of the irradiated Q12 in Figure 7.7d also shows various large-scale issues. The lower right readout chip had operational problems, which caused a significant drop in efficiency across the entire readout chip region. Alongside the interchip regions, the efficiency decreases due to partial delamination of bumps caused by improper bump bonding. Additionally, many pixels in the interchip region were completely unresponsive due to the masking procedure, which was not adjusted to the increased noise of the larger pixels in that region. As only a finite amount of time can be spent on the module tuning during a beam test, the optimisation of the pixel thresholds and masking sometimes proves to be more challenging, and non-optimal tunings are still considered to be good enough.

The issues with the tuning process were addressed during beam tests in 2024 and have been improved for upcoming beam tests in 2025 and beyond to treat the interchip pixels separately. Determining a proper average efficiency of the entire pixel matrix is done by selecting a region of interest around all areas of inefficiency that do not reflect the actual performance of the quad module.

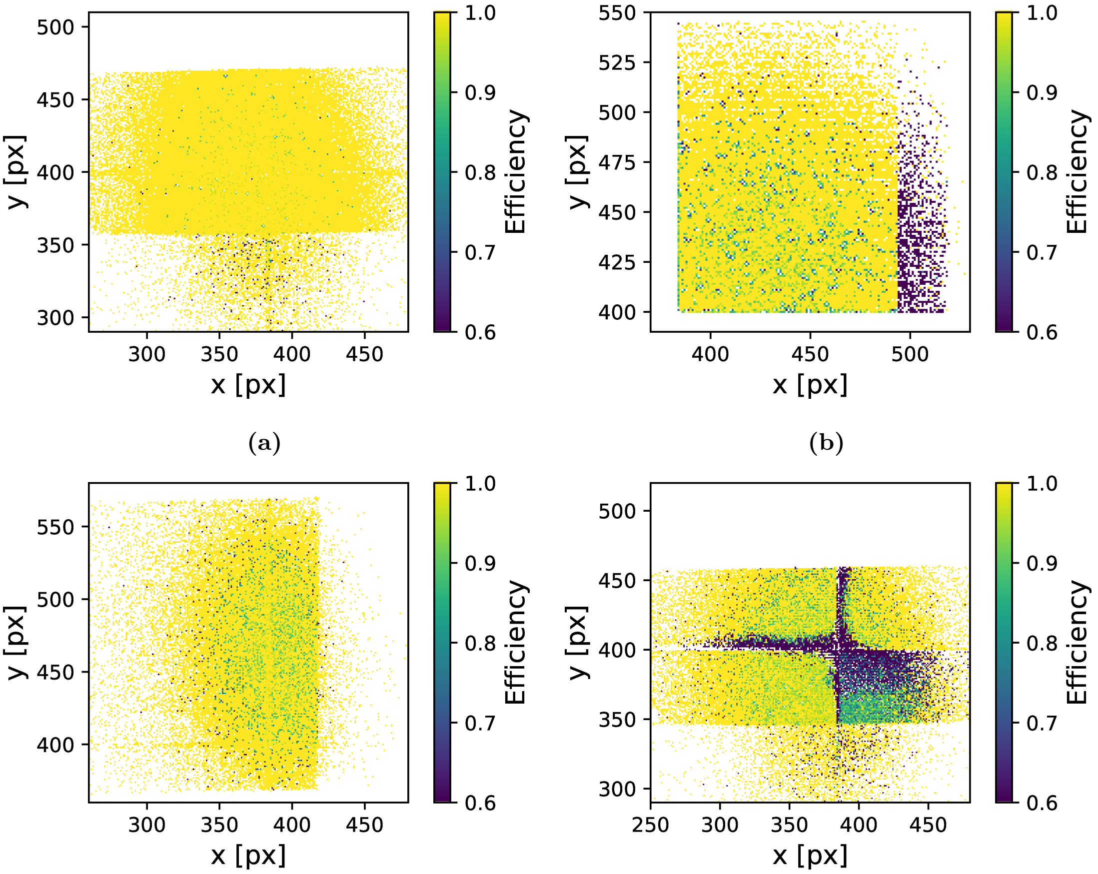

(a) (b)

(c) (d)

Figure 7.7: Efficiency of the pixel matrix for the unirradiated ADVQV2 (a) at 80 V bias, the irradiated KEKQ16 (b) at 495 V bias, the unirradiated Q18 (c) at 80 V bias and the irradiated Q12 (d) at 491 V bias.

The average efficiency of the quad modules is calculated with Equation 6.3. All tracks that intersect non-masked pixels are taken into account. The statistical uncertainty of the efficiency, as defined by Equation 6.4, depends inversely on the number of tracks. Since many 100k tracks are reconstructed for each tuning of the quad modules, the statistical uncertainties become negligible.

However, systematic uncertainties remain relevant. To estimate their magnitude, the data from each tuning is divided into smaller subsets from which the mean and standard deviation of the efficiency are calculated. This way, variations in the performance of the DUTs during data taking are accounted for. While minor effects, such as temperature changes or shifts in the position of the DUT, are not uncommon, they typically have only a small impact. Temporary issues with the operation of the FE, the data acquisition chain or the decorrelation of the trigger system with the DUT can significantly affect performance, but can be filtered out if they only impact a subset of the data. The subsets of the runs contain 200k events, which translates for most tunings to approximately 60k tracks with associated clusters on the DUTs.

The efficiency of the quad modules is required to be 98.5 % for unirradiated and 97.0 % for irradiated modules to be considered performant enough for installation in the ATLAS ITk. Figure 7.8 shows the average efficiency of the quad modules for different tunings and the required efficiency threshold. For the unirradiated modules, the efficiency is high for all applied bias voltages from 5 to 120 V. Fluctuations of the efficiencies are mostly between 99 and 100 %, which is likely caused by the non-optimal tuning. The larger uncertainties of the Q18 module are likely due to temporary problems in the data acquisition chain.

For the irradiated quad modules shown in Figure 7.8b, a noticeable decrease in efficiency becomes visible for a bias voltage of 100 V. However, for the given fluences, the modules are not expected to be operated at these voltages anyway and only serve to benchmark the performance of the modules. At more realistic bias voltages of above 250 V, all modules achieve the required efficiency. Additionally, no significant performance fluctuations arose during data taking, resulting in small systematic errors. The higher thresholds of the KEKQ9 and the irradiated KEKQ16 did not reduce the efficiency in any significant way, pointing to the possibility of using higher thresholds to suppress noise.

The noticeably higher efficiency of approximately 2.5 % of the Q8 module in comparison to the equally irradiated Q12 module comes from the tilted position of the Q8 module, which counteracts inefficiency areas of the bias structure.

Besides the average efficiency of the module, it is also important to investigate the performance of the sub-pixel structure to check whether any unexpected systematic inefficiencies arise. This so-called in-pixel efficiency is determined by the intersection of the reconstructed tracks and the sensor. As a single pixel would not deliver nearly enough statistics, all enabled pixels are folded into a 2x2 pixel matrix. These dimensions are chosen since four pixels are supplied by a single bias dot for the Micron quad modules. Figure 7.9 shows the in-pixel efficiency of unirradiated and irradiated HPK and Micron quad modules. Both HPK modules show no systematic pattern of inefficiency, which is to be expected from their polysilicon bias structure. The Micron quad modules show an area of inefficiency in the middle of every 2x2 pixel matrix. This results from the bias structure utilising a bias dot.

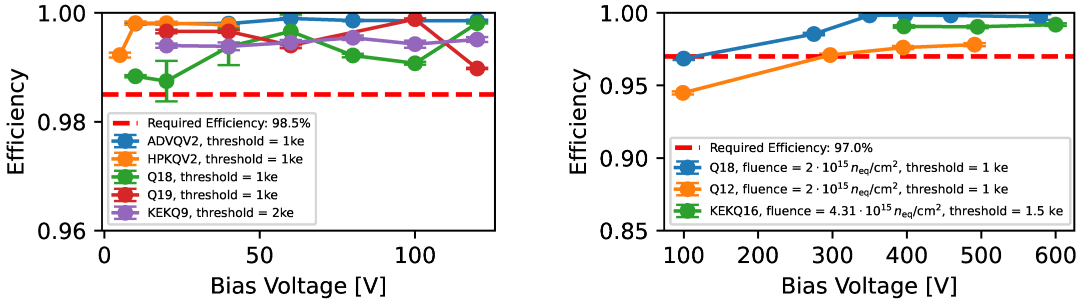

(a) **(b)**

Figure 7.8: Average efficiency of unirradiated (a) and irradiated (b) HPK and Micron quad modules.

In this area, free charge carriers are less likely to drift towards an electrode due to the distorted electric field close to the bias dot. The distortion of the inefficiency area in the in-pixel efficiency map of the Q18 module is caused by slight misalignments. As each bin here represents 1 µm, even minor misalignments have a significant impact. A drop in inefficiency is also present at the edges, left and right of the bias dot. This is likely due to a combination of the charge sharing effect and the bias rail that stretches over the sensor in the horizontal direction and overlays the bias dot. Charge sharing refers to the drift of deposited charges to multiple electrodes, increasing the likelihood that the smaller individual charge signals will not cross the detection threshold. The bias rail influences the electric field of the sensor, hindering the drift of charge carriers towards the electrodes. Both effects cause fewer charges to be registered in each individual pixel and make it more likely that not a single pixel registers a particle hit.

The area of inefficiency is so prevalent in the in-pixel efficiencies since the particles follow a straight path through these areas. As mentioned in Section 7.3, particles in the ATLAS experiment traverse the sensors at different angles. This effect is mimicked by tilting the sensor, thus preventing a perpendicular beam incidence. From the investigated Micron sensors, only the irradiated Q8 sensor was used for measurements with a tilt of 15°. The in-pixel efficiency of the Q8 is shown in Figure 7.9e. The area of inefficiency decreased significantly and is stretched along the y-axis. The stretched area arises from the projection of the tilted module into a 2D map. The drop in efficiency to the side of the bias dot also stretches accordingly in the projection.

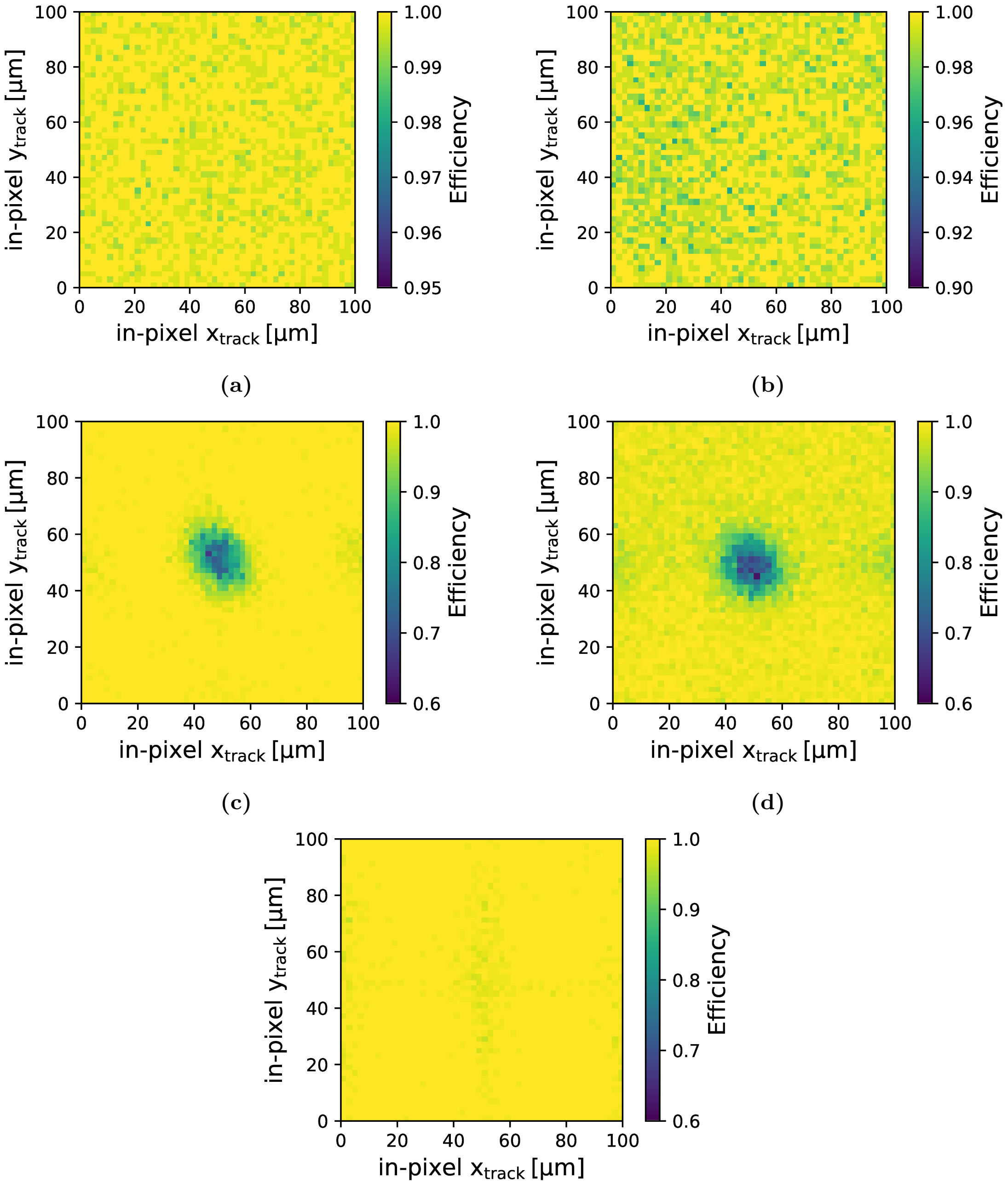

(a)

(b)

(c)

(d)

(e)

Figure 7.9: In-pixel efficiency of the unirradiated ADVQV2 at 80 V bias (a), the irradiated KEKQ16 at 495 V bias (b), the unirradiated Q18 at 80 V bias (c), the irradiated Q12 at 491 V bias (d) and the irradiated and tilted Q8 at 398 V bias (e).

The average efficiency of the interchip region is a key measure of its performance, especially since the number of tracks available for in-pixel efficiency analysis is often insufficient. To calculate the average interchip efficiency, the bottom, top, right, left, and centre regions for each quad module are evaluated separately, as shown in Figure 7.10. The associated uncertainties are calculated using the binomial uncertainty formula, as outlined in equation 6.4. Unlike the overall module efficiency, no data subsets were created to estimate systematic errors due to the limited number of tracks, which varied from 800 to 30k, depending on the module and interchip region. The efficiencies presented here are derived from runs with the highest track counts to minimise statistical errors, resulting in different bias voltages across the modules, as illustrated. No interchip efficiency could be determined for the KEKQ16 due to its small region of interest, which is mostly outside the interchip regions.

The centre interchip region generally exhibits the highest uncertainties, as expected, due to its smaller area. The unusually low efficiency in the centre region for the unirradiated KEKQ9 module is considered an outlier, likely caused by a single non-optimally working pixel that was not masked, leading to a noticeable drop in efficiency.

The irradiated Q12 module also shows lower efficiency across most regions compared to the Q8 module, despite both being irradiated to the same fluence. This discrepancy is likely due to the lower bias voltage applied to the Q12. Higher bias voltage runs could not be used for the Q12 because the module's interchip region tuning was suboptimal.

Aside from these outliers, all modules, including the irradiated ones, achieve efficiencies above 98 % across all interchip regions, demonstrating that the interchip region can be effectively utilised for track reconstruction in the ATLAS ITk.

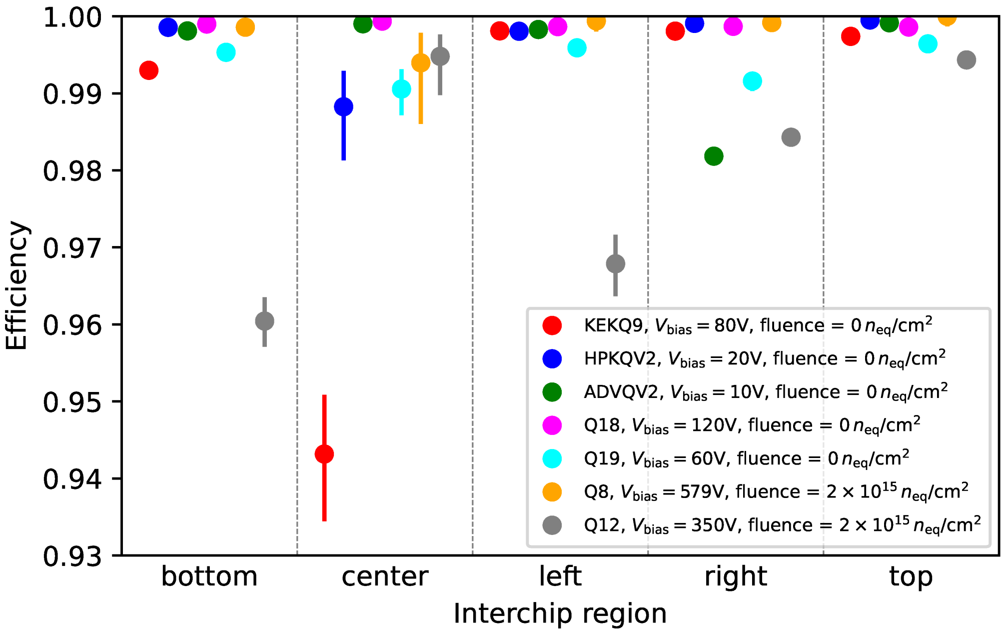

Figure 7.10: Average efficiency of the pixels in the interchip regions of the investigated quad modules.

The results in this chapter demonstrate that all investigated planar quad modules from the vendors HPK and Micron meet the ITk efficiency requirements. The clustering, masking, and in-pixel behaviour of the modules show no systematic issues that impair their performance. Despite suboptimal conditions for studying the interchip region of the quad modules, such as limited statistics and unoptimised tuning and masking, the efficiency in this region, for both unirradiated and irradiated modules, remains comparable to that of the entire pixel matrix. The production of ITk modules is set to begin in 2025, using sensors similar to those investigated in this thesis.

8 Investigation of In-Time Efficiency of the ATLAS ITkPixV1.1 Readout Chip

The LHC and its four large experiments operate with a 40 MHz clock, corresponding to the bunch crossing frequency. This clock is synchronised with the 40 MHz clock of the ITk pixel module FEs, ensuring that only hits occurring within a 25 ns time window are read out. An L1 trigger signal is sent to the FE of a pixel module to read out the respective data of a single bunch crossing. While it is possible for a module to read out multiple bunch crossings from a single trigger, defined by the trigger multiplier, this feature is not supported for the pixel modules in the ATLAS experiment, as the bandwidth is not sufficient for the higher data rates.

During beam tests, a trigger multiplier is defined, allowing data to be read out over multiple consecutive clock cycles, typically ranging from 16 to 20 cycles. The clock cycle in which a hit is recorded is determined by the trigger identifier (TID), which simply counts the number of clock cycles up to the configured trigger multiplier starting at the time the trigger occurred. This ensures that hits are always read out during beam tests, regardless of exact timing conditions. As the induced charge signals cross the threshold with a delay dependent on both the signal amplitude and the configuration of the beam test telescope and FE settings, as explained in Section 4.4, the timestamp of the registered data may fluctuate and shift to a later TID. Additionally, the module may exhibit a lower efficiency at the start of a cycle, as the clock edge does not transition to a high state instantaneously. To assess the performance of ITk pixel modules in relation to the FE 40 MHz clock, efficiency must be investigated on time scales smaller than the 25 ns window.
An unirradiated ITkPixV1.1 SCC module with a SINTEF [99] 3D sensor was used to conduct a beam test study, focusing on data acquisition with a high-precision time resolution setup. The methodology of this study is detailed in the following section.

8.1 Beam Test Setup

The ACONITE telescope, as described in Chapter 6.1, was utilised for this beam test study. Six Mimosa26 planes were used for particle tracking, while an FE-I4 plane served as a time reference.

Two pairs of scintillators, positioned at the front and back of the telescope, provided fast signals to the AIDA TLU, which distributed trigger signals to the various detector modules. Additionally, the TLU timestamped events based on the scintillator inputs using a 1280 MHz clock, corresponding to a time resolution of approximately 780 ps.
The ITk pixel module was interfaced via a BDAQ board using the BDAQ53 readout system [57]. This framework facilitates the characterisation and testing of RD53 chips and was employed in this beam test due to its precise determination of the TID.
Since both the AIDA TLU and the BDAQ board operate with independent 40 MHz clocks, the TLU timestamps and trigger IDs can only be correctly correlated if the clocks are synchronised. Otherwise, inevitable jitter would change the phase between the clocks over time. To synchronise the clocks, the TLU clock is fed into the BDAQ board. Figure 8.1 schematically illustrates the beam test setup, including the AIDA TLU, the BDAQ board, the telescope, the DUT and scintillators. A photograph of the setup, showing the DUT and tracking planes, is provided in Appendix B.1.

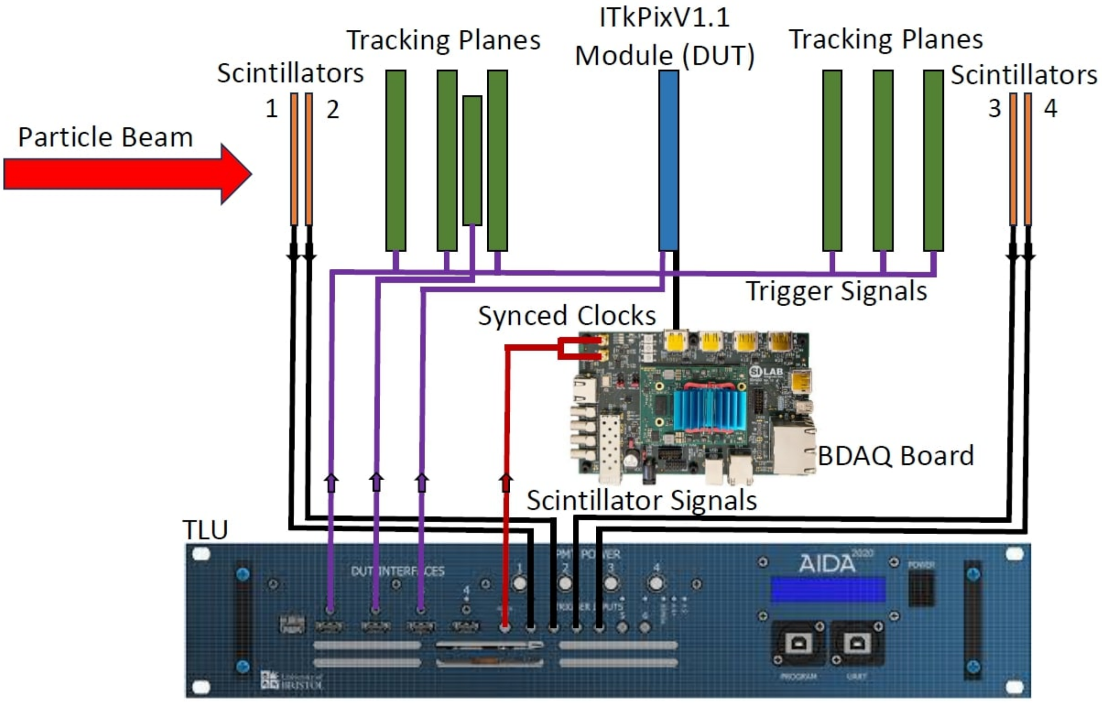

Figure 8.1: Beam test setup including the AIDA TLU and the BDAQ board with synchronised clocks. The telescope consists of six Mimosa26 tracking planes and one FE-I4 module for time reference [57, 73].

For a particle traversing the telescope, the timing of the TLU and the BDAQ board is illustrated qualitatively in Figure 8.2 to enhance understanding of the correlation between the TID and the TLU timestamps. Delays caused by cable lengths and communication between the TLU, BDAQ board, and the module are omitted for clarity. Once the TLU sends out a trigger signal, the BDAQ board processes it and verifies whether the module's data can be read out. It takes several clock cycles for the BDAQ board to issue the command to retrieve the stored data from the module. Consequently, a latency parameter is used to define the time elapsed since the data was stored in the module. As the setup remains unchanged during operation, this latency only needs to be set once for the beam test.
Each recorded hit is assigned a TID, which starts counting in 25 ns increments from a time preceding the hit registration, as determined by the configured latency. Ideally, all recorded hits should correspond to a single TID, given that the time difference between the scintillator and DUT hits remains largely constant for high-energy particles. However, some hits may migrate to the next higher TID due to the discrepancy between the transmitted trigger signal from the TLU and the actual threshold crossing of the induced voltage signal in the FE. Within a specific range of the 25 ns time frame, this TID migration occurs when the timewalk effect is substantial enough to shift the registered signal into the subsequent clock cycle of the module. For synchronised clocks with a phase shift of 0°, migration to the next TID is expected to occur at the end of the 25 ns window of the TLU. However, the synchronised clocks of the TLU and BDAQ maintain a constant phase shift, which is not necessarily 0°. Due to the BDAQ board requiring a 160 MHz input clock, this phase shift can assume four discrete values, changing each time the TLU is reconfigured. Consequently, TID migration is expected to occur at different positions within the TLU timestamp range but remains stable throughout a single run.

In the ATLAS detector, only a single TID can be read out, meaning any hits that have migrated to the next TID are lost, reducing the efficiency of the pixel module. However, unlike in beam tests, where the particles traverse the telescope at random times, the LHC beam is precisely bunched at a 40 MHz frequency. As a result, hits only migrate to an incorrect TID if the threshold crossing of the hit is delayed by more than 25 ns. Such delays are primarily caused by significant timewalk effects for small charge signals below approximately 1500 e [100].

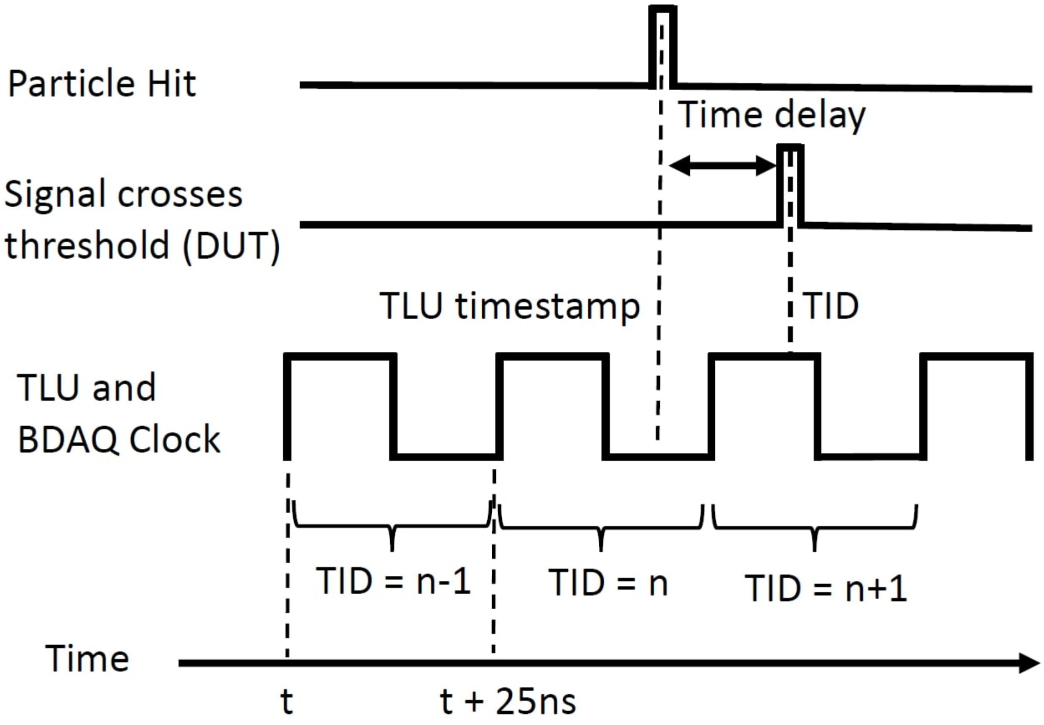

Figure 8.2: Simplified representation of how the TLU timestamp and the TID are correlated with a particle hit. In this example, the TID migrates into the n+1 bin due to the time delay. The delay shown in the image is exaggerated for better visualisation.

8.2 Timing Precision of the Beam Test Setup

The likelihood of TID migration depends on the magnitude of the timewalk effect and the timing precision of the setup, specifically the scintillators and the AIDA TLU. This section provides a detailed analysis of the time resolution of the setup.
The TLU's 1280 MHz clock assigns timestamps based on the average timing of all scintillator inputs. Each scintillator signal is associated with an 8-bit fine timestamp word, corresponding to a time resolution of 780 ps. As this timestamp is highly dependent on the stability of the scintillators, their precision must be ensured. While particle arrivals occur at random times, leading to random individual fine timestamps as shown in Figure B.2, their differences are correlated. The extracted particle beam consists of 120 GeV pions, which travel nearly at the speed of light in a straight path through the telescope. Consequently, similar time differences are expected between the scintillators.

Figure 8.3 presents the differences in fine timestamps among the four scintillators. The scintillators were numbered as shown in Figure 8.1. Three of the four scintillators exhibit similar behaviour, with their differences following a Gaussian distribution centred slightly above zero. The shift in the mean timestamp difference between scintillators 0 and 3 arises from the finite time required for light to traverse the telescope, which is approximately 3 ns. A complete 25 ns clock cycle comprises 32 fine timestamp values, meaning the fine timestamps span a total of eight TLU clock cycles. Since the timing process and data acquisition are identical across these eight cycles, the fine timestamp values are mapped into a single representative clock cycle. Scintillator 2 exhibits significantly deviating timestamp information, attributed to different cabling and generally less stable performance. The configurations of the scintillators were optimised individually to achieve comparable performance. This was accomplished by adjusting the supply voltage, which ranged from 1.00 to 1.05 V, and setting the discriminator threshold for incoming signals at the TLU to −0.11 V. Despite these optimisations, the instability of scintillator 2 could not be resolved. As a result, scintillator 2 is excluded from the determination of the average fine timestamp, with only the remaining three scintillators being utilised. The timestamp differences of these scintillators exhibit standard deviations between 1.80 and 2.26 ns, introducing significant fluctuations that impair the timing precision of the setup. Due to time constraints during the beam test, it was not possible to implement a setup with a more precise time resolution.

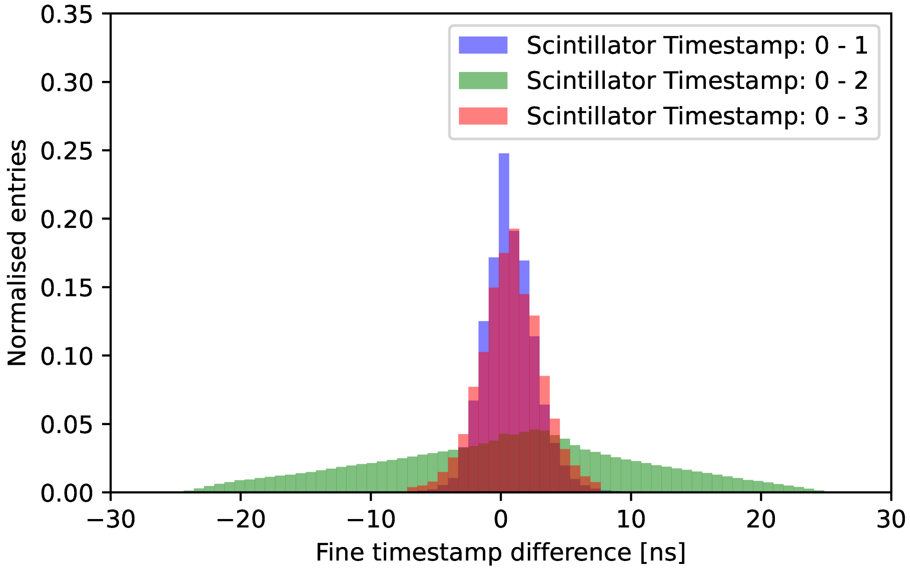

Figure 8.3: Fine timestamp differences of the four utilised scintillators. Scintillator 0 was used as the reference, from which the fine timestamp values of the other scintillators were subtracted.

8.3 In-Time Measurement Results

The data collected from the beam test is reconstructed under conditions similar to those described in Chapter 7. All pixels that did not register a hit are masked. However, no additional masking was applied in Corryvreckan, as the module tuning already accounts for noisy pixels. The noise scan utilised 10^7 trigger signals per pixel, considering a pixel as noisy if it recorded more than 10 hits. These values were selected based on prior experience with operating unirradiated ITk pixel modules. A matching radius of 100 µm was used to associate cluster centres with reconstructed tracks.
Several different configurations of the DUT were tested to analyse the potential influence of various factors. These configurations included adjustments to the module's bias voltage and threshold, both of which can affect the timing of particle registration. Moving the module to focus the beam spot on different regions of the pixel matrix allowed for an investigation into the uniformity of clock distribution across the FE. Modifying the bias current of the differential preamplifier influenced the amplifier's response time, gain, and noise level. Higher bias currents reduce noise and timewalk, but increase power consumption. Table 8.1 summarises the different module configurations investigated. Due to limited data-taking time, not all possible combinations were explored. The module's default configuration included a threshold of 1 ke, a bias voltage of −10 V, a bias current DAC setting of 895 for the differential preamplifier, and a beam spot positioned at the centre of the pixel matrix. Only one of these properties was varied at a time, except for the beam spot position, which was measured for thresholds of 1 ke and 1.5 ke.

Table 8.1: List of the different module configurations used for data taking. Lower DAC values for the preamplifier correspond to lower bias currents.

Beam spot position	Bias voltage	Threshold	Diff. preamp. DAC
Centre	−5 V	1 ke	450
Top left	−10 V	1.5 ke	550
Top right	−15 V		730
Bottom left	−20 V		895
Bottom right			

The correlation between the TID of the hits and the event timestamps of the TLU is depicted in Figure 8.4a for a threshold of 1.5 ke. This configuration is presented due to the largest number of reconstructed tracks recorded in this run. In this setup, the default TID is 11, with a narrow time range in which the TID migrates to the next value. The timestamp at which these migrations occur can vary significantly depending on the delay in registering the hit and the phase shift between the synchronised TLU and FE clocks. However, the duration of the time window in which TID migrations occur is primarily influenced by the timewalk effect and the limited time resolution of the scintillators.

The standard deviation of the timestamp distribution associated with TID = 12 is 3.07 ns, which is slightly larger than the standard deviations of the scintillator signal distributions. These variations in time delays are predominantly due to the timewalk effect, which is influenced by the tested parameters.

The efficiency and corresponding uncertainty, as defined in Equations 6.3 and 6.4, are used to calculate the module's efficiency in this configuration. To account for the effect of TID migrations, all associated hits that migrated are excluded, thereby reducing the module's efficiency. As these migrations depend on the timestamp, the average efficiency of the module is shown in Figure 8.4b as a function of the 25 ns clock cycle. The resulting dip, caused by the exclusion of clusters with migrated trigger IDs, nearly reaches zero efficiency at its minimum.

To estimate the width of the dip, the full width at half maximum (FWHM) criterion is applied due to its standardised definition and its suitability for asymmetric peaks. The width of the dip is defined as the difference between the two points where the efficiency reaches half of its minimum value. The positions at which this occurs are determined by linear interpolation between the two relevant values on each side of the dip. For the discussed configuration, the FWHM is 7.03 ns. Table 8.2 lists all FWHM values of the efficiency dips and the standard deviations of the timestamp distributions for TID= 12 across different configurations. Since the efficiency dip extends over a significant portion of the total clock cycle, the overall average efficiency is notably reduced. The resulting average efficiencies across all clock cycles are also listed in the table, with statistical uncertainties determined using Equation 6.4. The influences of the different module parameters are discussed in the following:

- **Discriminator threshold:** The highest FWHM of the efficiency dip, approximately 6–7 ns, and consequently the lowest efficiency, is associated with the higher discriminator threshold of 1.5 ke. A higher threshold increases the time delay caused by the timewalk effect, as also demonstrated in [100].
- **Differential preamplifier bias current:** The influence of lower differential preamplifier bias currents on timewalk was observable. This behaviour is expected, as the bias current affects the speed and response of the preamplifier. However, a significant reduction in the FWHM of the efficiency dip was only observed for the lowest bias current setting.
- **Bias voltage:** Lowering the module's bias voltage reduces the strength of the electric field, resulting in slower drift of charge carriers and an increased delay before the charge signal crosses the threshold. An exception was found for the default configuration at −10 V, which exhibited similar FWHM values in the lower corners as a configuration with −15 V bias and a centred beam spot.

- **Beam spot position:** Adjusting the module position to shift the beam spot into different corners of the pixel matrix noticeably affected the FWHM of the efficiency dip. For both threshold tunings, more pronounced TID migration occurred when the beam spot was focused in the lower and central regions, indicating a non-uniform clock distribution across the module. While this is not ideal for uniform performance, it increased the FWHM by less than 1 ns across the matrix. Notably, no significant deviations in TID migration were observed in the lower and central parts of the module.

Table 8.2: FWHM of the efficiency dips for different module configurations. Only the modified parameters are listed. The default values for each parameter are: Beam spot position = centre, threshold = 1 ke, diff. preamp. bias current := 895, $V_{\text{bias}} = -10\,\text{V}$. The corresponding average efficiencies and their statistical errors are also listed.

Module configuration	**FWHM of eff. dip [ns]**	**Average eff.**
Upper Right	3.91(3)	0.771(3)
Upper Left	3.91(4)	0.752(2)
Lower Right	4.69(3)	0.748(3)
Lower Left	4.69(4)	0.730(3)
1.5 ke	7.03(3)	0.6664(7)
1.5 ke, Upper Right	6.25(3)	0.681(3)
1.5 ke, Upper Left	6.25(4)	0.739(3)
1.5 ke, Lower Right	7.03(3)	0.648(2)
1.5 ke, Lower Left	7.03(4)	0.625(3)
Diff. Preamp. = 730	4.69(3)	0.757(2)
Diff. Preamp. = 550	4.69(4)	0.665(3)
Diff. Preamp. = 450	5.47(3)	0.739(3)
V_{bias}=−5 V	5.47(4)	0.74(2)
V_{bias}=−15 V	4.69(3)	0.762(3)
V_{bias}=−20 V	3.91(5)	0.779(3)

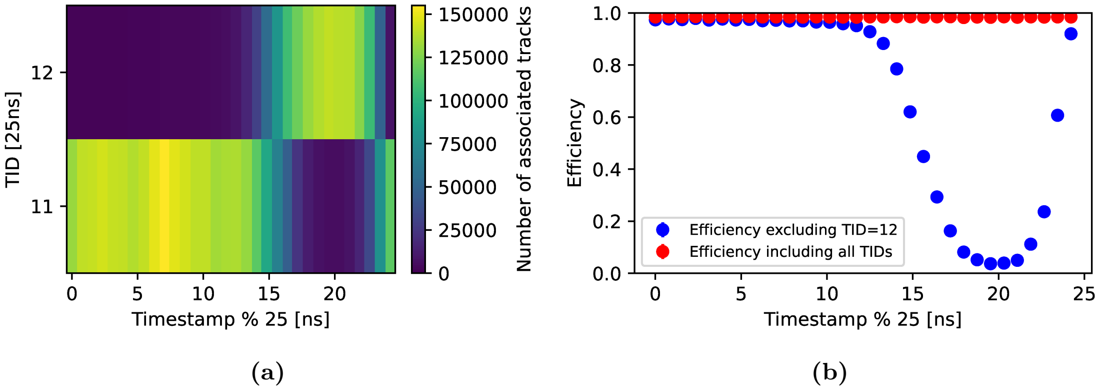

Figure 8.4: a) TID of the clusters as a function of the event timestamp. The clock cycle repeats every 25 ns. Therefore, the timestamp modulo 25 is plotted. b) Average efficiency of the SCC as a function of the TLU timestamp for all TIDs and with TID=12 excluded. Approximately five million events were recorded in this run, with a threshold of 1.5 ke.

The average module efficiency, without excluding clusters with a TID migration, remains consistently high, exceeding 98 % across the entire clock cycle. The decrease in the average efficiency is attributed to the doping structure of the 3D module. The presence of doped pillars reduces the sensitive silicon volume in those regions, resulting in undetected hits. When particles traverse these areas, charge carriers are less likely to drift towards an electrode, due to the non-optimal electric field. This efficiency reduction is noticeable in this beam test, as the SCC was positioned perpendicular to the particle beam incidence. To assess the impact of this effect, the in-pixel efficiency was analysed, following the definition in Chapter 7.5. The results are shown in Figure 8.5, where all pixels are folded into a single one to reflect the repeating doping structure across the pixel matrix. The in-pixel efficiency follows the expected pattern, with a decrease to approximately 60–90 % at the p^+-doped pillars located at the pixel corners. These findings align with previous beam test analyses of the SINTEF 3D sensor [101].

A decline in efficiency due to a non-instantaneous rising clock edge is not observed. While uncertainties in the scintillator trigger signal could blur a sharp efficiency drop, a dip would still be expected if the effect occurred on timescales of 780 ps or longer. This suggests that any efficiency loss due to timing effects occurs on even smaller timescales, making it negligible for the module's overall performance and further emphasising its detection capabilities.

For measurements with improved time resolution, the next-generation picosecond TLU, which is intended to replace the AIDA TLU, would be more suitable, as it is designed to provide $\mathcal{O}(100\ \mathrm{ps})$ timing precision. However, since the timing resolution of the TLU is fundamentally limited by the baseline timing references, scintillators in this case, the performance of these references must be significantly enhanced. The most promising alternatives include microchannel plate proportional photomultiplier tubes [102] and low gain avalanche diodes [103], both of which can achieve timing resolutions of $\mathcal{O}(100\ \mathrm{ps})$.

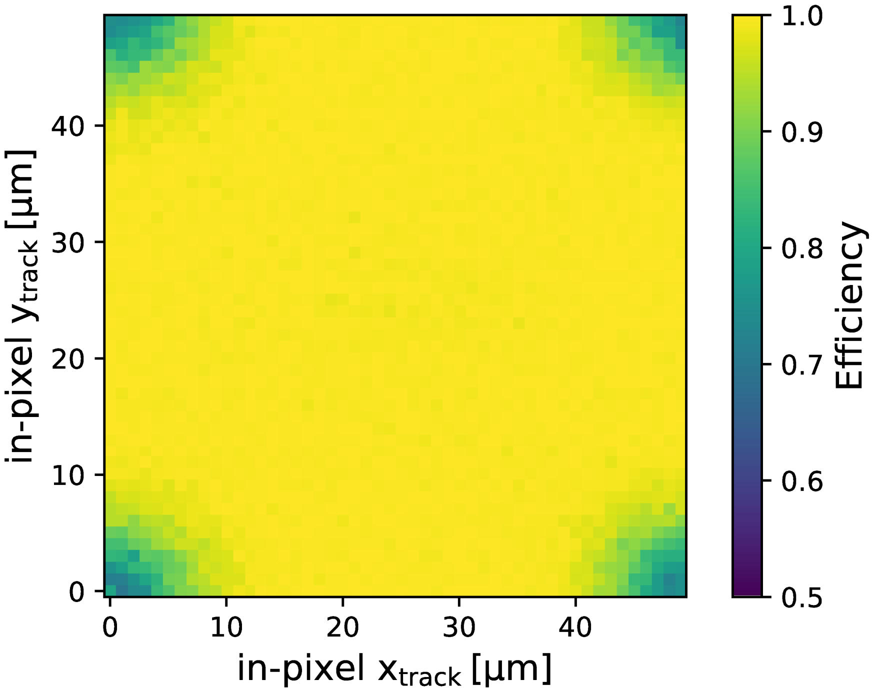

Figure 8.5: In-pixel efficiency of the 3D SCC for perpendicular beam incidence and a threshold of 1.5 ke.

In summary, TID migration of detected hits can impair the module's performance, particularly for small charges, where the timewalk effect is more pronounced. To mitigate TID migration, a higher bias voltage is recommended to minimise delays in charge collection. Lowering the detection threshold to around 1 ke and maintaining a higher current in the differential preamplifier help counteract migration by reducing the timewalk effect. Addressing the impact of non-uniform clocks is more challenging and cannot be easily counteracted by tuning. However, this effect contributes only marginally to TID migration. Optimising the investigated parameters influences the time delay at which a hit is registered by the FE, with variations on the order of 1 ns.

9 Summary and Outlook

The investigation of ITk pixel modules is of paramount importance to ensure the optimal operation of the future ATLAS ITk. To this end, several ITk pixel modules featuring the ITkPixV1.1 and the final design ITkPixV2 readout ASICs were studied in beam tests. Additionally, QA measurements were conducted on pre-production test structures that mimic the sensor properties of the modules. The pre-production test structures from HPK and Micron meet all requirements tested within the scope of this thesis. The leakage current was found to be stable, remaining within 25 % of its mean value under stable temperature conditions of ±0.1 °C. For all investigated TS, the leakage current remained below 2 nA/cm^2 and 30 µA/cm^2 for unirradiated and irradiated modules at bias voltages of up to 200 V and 600 V, respectively. Breakdown in HPK structures was only observed at bias voltages exceeding 1 kV. The relative uncertainties in leakage current measurements were higher for unirradiated sensors due to the limited resolution of the utilised Keithley 2410, which was on the order of 100 pA. The determined depletion voltages of up to 50 V from CV measurements were significantly lower than expected for the irradiated Micron TS, likely due to annealing effects and the gradual saturation of $1/C^2$ with increasing bias voltage.

Planar quad modules from HPK and Micron satisfy the ITk efficiency requirements in both unirradiated and irradiated states. While the operation of multiple readout chips posed challenges during beam tests, no chip exhibited systematic issues related to its performance. Fewer than 4 % of pixels in the investigated irradiated modules were classified as noisy or dead. No unexpected in-pixel structures were observed in any module. The inefficiency areas in Micron sensors will not impact module performance in the ITk, as particles are unlikely to follow straight trajectories through the bias dot while traversing in a magnetic field. The interchip region exhibited high efficiencies across all investigated modules. The more noticeable fluctuations in efficiency were attributed to limited statistics, as the interchip region constitutes only a small area. Efficiencies below 97 % were likely due to suboptimal tuning of the interchip pixels, as the standard tuning procedure was not specifically adjusted for the large pixels in this region. This issue will be addressed in future beam tests.

Investigating the in-time efficiency of the ITkPixV1.1 FE proved feasible but challenging with the current beam test setup at CERN. Achieving a time resolution of 780 ps using the AIDA TLU to probe the FE clock was hindered by the lower time resolution of approximately $2-3$ ns of the scintillators. Nevertheless, the measurement principle was successfully demonstrated, as the expected TID migration due to the timewalk effect was observed. Various module configuration parameters were adjusted to study their impact on TID migration. Increasing the threshold from 1 ke to 1.5 ke led to the most significant increase, with the FWHM of the efficiency dip for a single TID increasing by approximately 2.5 ns. Higher bias voltages for the sensor and higher bias currents for the differential preamplifier were shown to counteract TID migration. Consequently, reducing the differential preamplifier bias current to lower power consumption is generally not advisable if TID effects are a concern. While increasing the bias voltage mitigates TID migration, factors such as leakage current and power consumption must be considered, and decisions cannot be based solely on TID mitigation, though it is recommended for that purpose. Applying bias voltages from -5 V to -20 V reduced the FWHM of the efficiency dip by approximately 1.5 ns. The non-uniformity of the FE clock distribution across the pixel matrix had only a minor effect on TID migration. No measurable efficiency loss was attributed to the finite rise time of the FE clock with the current timing setup, implying that any impact occurs on even shorter time scales and is insignificant for overall ITk pixel module performance. The established measurement principle can be applied to the final design FE, where TOT information is recorded for a more precise determination of in-time efficiency. Moreover, examining the in-time efficiency of irradiated modules is essential to assess whether radiation damage significantly degrades the in-time efficiency. Enhancing the time resolution of scintillators by employing more advanced timing detectors, such as low-gain avalanche diodes or microchannel plate photomultiplier tubes, is highly recommended. Future timing setups using the forthcoming picosecond TLU are expected to achieve time resolutions on the order of 100 ps.

The investigation of ITk pixel modules confirms that the module production is expected to deliver high-quality planar pixel detectors for installation into the ATLAS ITk. Further beam tests in 2025 will be conducted to validate the performance of the final design modules in production batches.

To ensure optimal beam test conditions regarding the quality of reconstructed tracks, a simulation study utilising high-intensity beams was conducted. The study demonstrated that track reconstruction remains feasible without significant degradation in track quality. Due to the predominantly straight trajectories of particles, a machine learning approach to identify fake tracks provided only a marginal improvement over simple one-dimensional cuts on the χ^2/ndof value of tracks. This finding supports the feasibility of increasing beam intensity to enhance data collection rates for future ITk beam tests at the CERN SPS North Area.

Appendices

A Track Fit Quality in a Beam Test

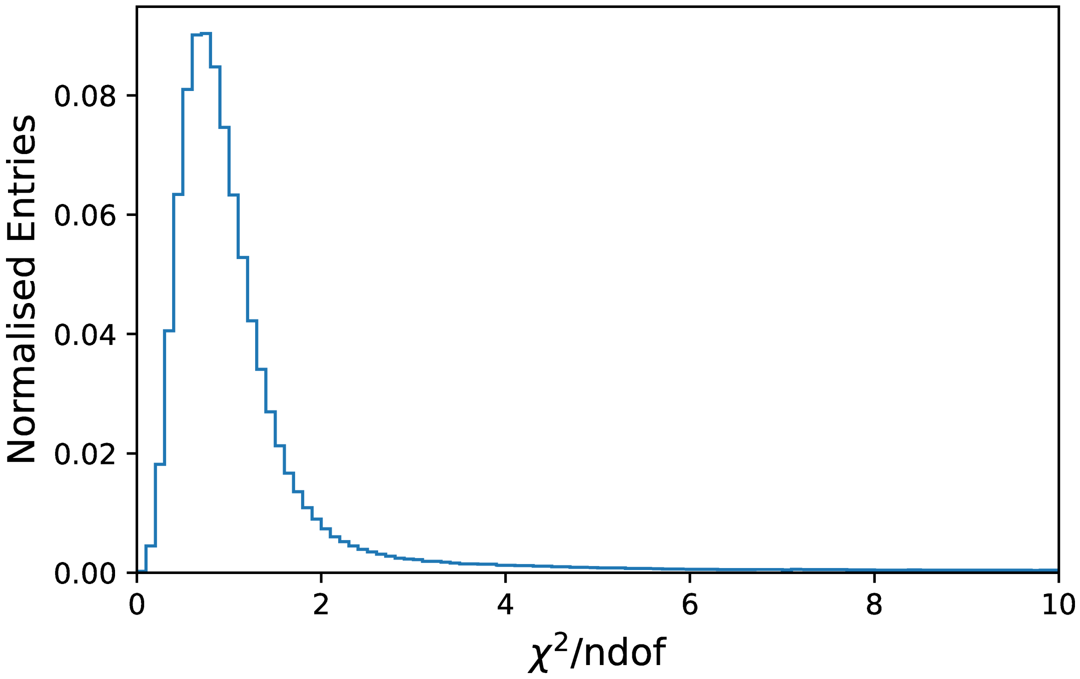

Figure A.1: Normalised χ^2/ndof distribution of reconstructed tracks using the GBL algorithm. All six Mimosa26 planes and a time reference plane using the ITkPixV1.1 were utilised to reconstruct the tracks. A most probable value close to 1 suggests successful alignment and high-quality track fits.

B In-Time Efficiency Measurement

B.1 Beam Telescope of the In-Time Efficiency Measurement Setup

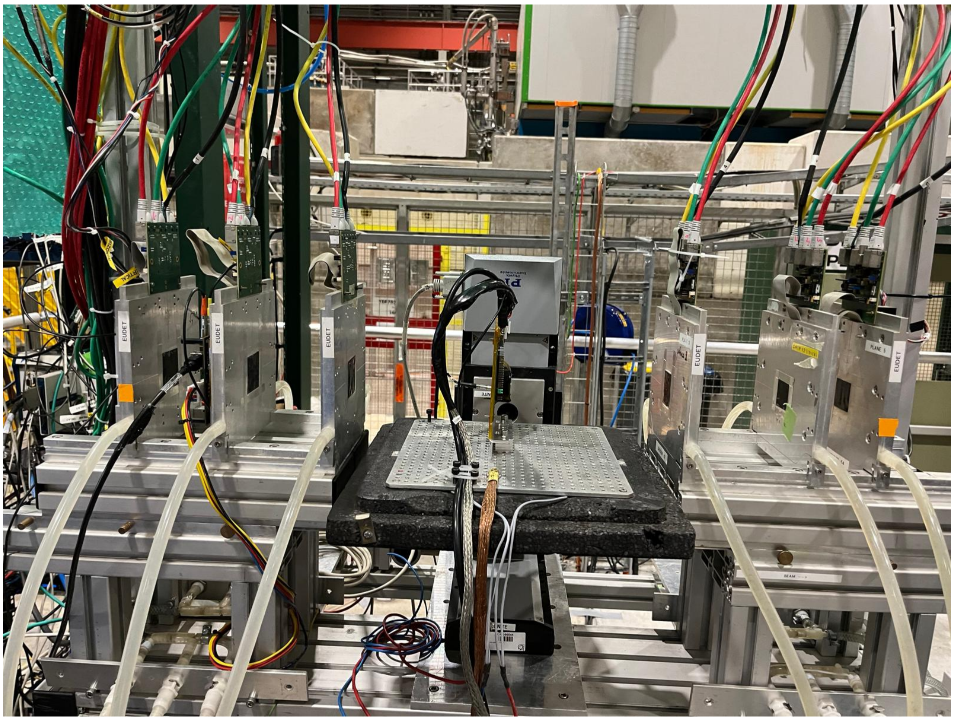

Figure B.1: Photo of the beam test setup including the tracking planes and the SINTEF 3D module as DUT.

B.2 TLU Timestamp distribution

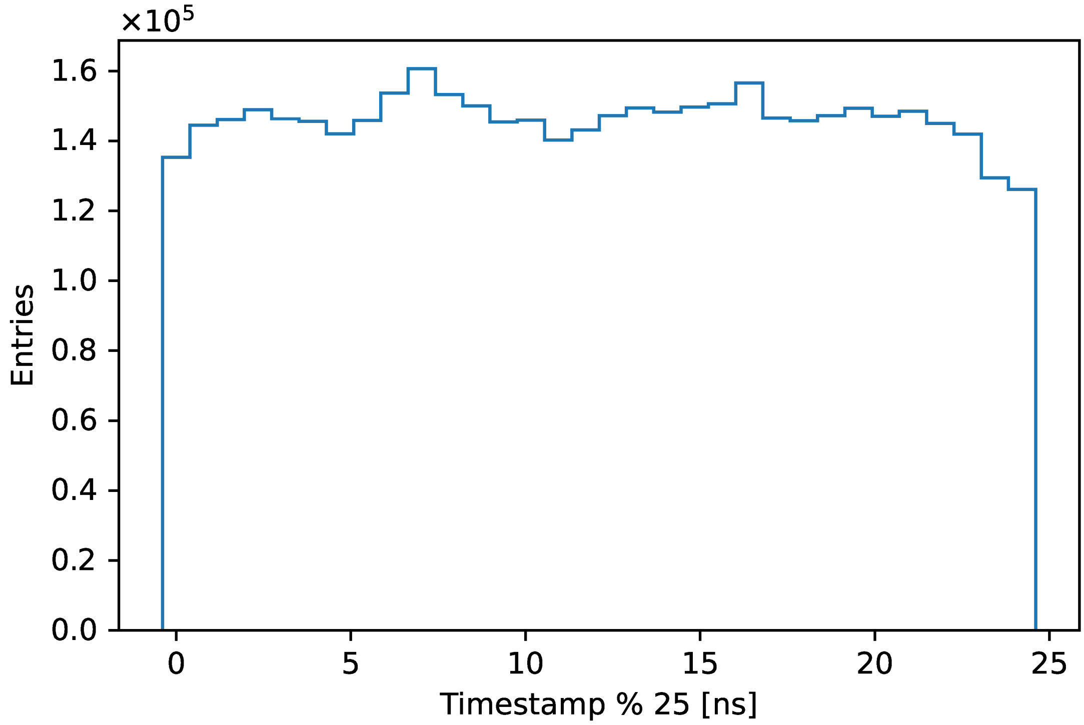

Figure B.2: TLU timestamp modulo 25 distribution for approximately 5 million events. As the particles from the beam traverse the telescope at random times, the distribution is nearly uniform.

Bibliography

[1] L. Evans and P. Bryant, *LHC Machine*, Journal of Instrumentation **3** (2008) S08001.

[2] ATLAS Collaboration, *Observation of a new particle in the search for the Standard Model Higgs boson with the ATLAS detector at the LHC*, Physics Letters B **716** (2012) 1, ISSN: 0370-2693.

[3] J. Silk et al., *Particle Dark Matter: Observations, Models and Searches*, ed. by Gianfranco Bertone, 2010, URL: `https://doi.org/10.1017/CBO9780511770739.002`.

[4] ATLAS Collaboration, *The ATLAS Experiment at the CERN Large Hadron Collider*, Journal of Instrumentation **3** (2008) S08003.

[5] CERN, *Run 3 of the Large Hadron Collider*, 2024, URL: `https://home.cern/press/2022/run-3`.

[6] G. Roland, K. Šafařík, and P. Steinberg, *Heavy-ion collisions at the LHC*, Progress in Particle and Nuclear Physics **77** (2014) 70, ISSN: 0146-6410.

[7] X. Cid-Vidal and R. Cid, *LHC: the emptiest space in the solar system*, Physics Education **46** (2011) 45.

[8] L. Arnaudon et al., *Linac4 Technical Design Report*, revised version submitted on 2006-12-14 09:00:40, 2006, URL: `https://cds.cern.ch/record/1004186`.

[9] H. Damerau et al., *LHC Injectors Upgrade, Technical Design Report*, 2014, URL: `https://cds.cern.ch/record/1976692`.

[10] E. Lopienska, *The CERN accelerator complex, layout in 2022. Complexe des accélérateurs du CERN en janvier 2022*, General Photo, 2022, URL: `https://cds.cern.ch/record/2800984`.

[11] L. Evans, *The Large Hadron Collider*, New Journal of Physics **9** (2007) 335.

[12] ALICE Collaboration, *The ALICE experiment at the CERN LHC*, Journal of Instrumentation **3** (2008) S08002.

[13] LHCb Collaboration, *The LHCb Detector at the LHC*, JINST **3** (2008) S08005.

[14] CMS Collaboration, *The CMS experiment at the CERN LHC. The Compact Muon Solenoid experiment*, JINST **3** (2008) S08004.

[15] ATLAS Collaboration, *The ATLAS Experiment at the CERN Large Hadron Collider*, Journal of Instrumentation **3** (2008) S08003.

[16] J. Pequenao, *Computer generated image of the whole ATLAS detector*, 2008, URL: `https://cds.cern.ch/record/1095924`.

[17] ATLAS Collaboration, *ATLAS inner detector: Technical Design Report, 1*, Technical design report. ATLAS, Geneva: CERN, 1997, URL: `https://cds.cern.ch/record/331063`.

[18] J. Pequenao and P. Schaffner, *How ATLAS detects particles: diagram of particle paths in the detector*, 2013, URL: `https://cds.cern.ch/record/1505342`.

[19] ATLAS Collaboration, *ATLAS muon spectrometer: Technical Design Report*, 1997, URL: `https://cds.cern.ch/record/331068`.

[20] ATLAS Collaboration, *ATLAS tile calorimeter: Technical Design Report*, Technical design report. ATLAS (1996).

[21] ATLAS Collaboration, *ATLAS inner detector: Technical Design Report, 1*, 1997, URL: `http://cds.cern.ch/record/331063`.

[22] ATLAS Collaboration, *ATLAS magnet system: Technical Design Report, 1*, Technical design report. ATLAS (1997).

[23] ATLAS Collaboration, *Track Reconstruction Performance of the ATLAS Inner Detector at $\sqrt{s} = 13$ TeV*, tech. rep., CERN, 2015, URL: `http://cds.cern.ch/record/2037683`.

[24] ATLAS TRT collaboration, *The ATLAS TRT Barrel Detector*, Journal of Instrumentation **3** (2008) P02014.

[25] ATLAS TRT collaboration, *The ATLAS TRT end-cap detectors*, Journal of Instrumentation **3** (2008) P10003.

[26] A. Abdesselam et al., *The barrel modules of the ATLAS semiconductor tracker*, Nuclear Instruments and Methods in Physics Research Section A: Accelerators, Spectrometers, Detectors and Associated Equipment **568** (2006) 642, ISSN: 0168-9002.

[27] A. Abdesselam et al., *The ATLAS semiconductor tracker end-cap module*, Nuclear Instruments and Methods in Physics Research Section A: Accelerators, Spectrometers, Detectors and Associated Equipment **575** (2007) 353, ISSN: 0168-9002.

[28] N. Wermes and G. Hallewel, *ATLAS pixel detector: Technical Design Report*, 1998, URL: `https://cds.cern.ch/record/381263`.

[29] Alessandro Polini et al., *Design of the ATLAS IBL Readout System*, Physics Procedia **37** (2012) 1948, ISSN: 1875-3892.

[30] ATLAS Collaboration, *Operational Experience and Performance with the ATLAS Pixel detector at the LHC*, URL: https://indico.in2p3.fr/event/32425/contributions/142725/attachments/88901/134486/PixelStatus_Pixel2024.pdf.

[31] O. Aberle et al., *High-Luminosity Large Hadron Collider (HL-LHC): Technical design report*, CERN Yellow Reports: Monographs (2020).

[32] DESY, *The HL-LHC project*, 2022, URL: https://hilumilhc.web.cern.ch/content/hl-lhc-project (visited on 10/01/2023).

[33] ATLAS Collaboration, *Expected tracking and related performance with the updated ATLAS Inner Tracker layout at the High-Luminosity LHC*, 2021, URL: http://cds.cern.ch/record/2776651.

[34] ATLAS Collaboration, *Technical Design Report for the ATLAS Inner Tracker Pixel Detector*, 2017, URL: https://cds.cern.ch/record/2285585.

[35] ATLAS Collaboration, *Technical Design Report for the ATLAS Inner Tracker Strip Detector*, tech. rep., CERN, 2017, URL: https://cds.cern.ch/record/2257755.

[36] S. Kühn, *Results of Larger Structures Prototyping for the Phase-II Upgrade of the Pixel Detector of the ATLAS Experiment*, 2018, URL: https://indico.cern.ch/event/669866/contributions/3235377.

[37] ATLAS Collaboration, *Expected Tracking Performance of the ATLAS Inner Tracker at the HL-LHC*, 2019, URL: https://cds.cern.ch/record/2669540.

[38] S. Hadzic, *ATLAS ITk Pixel quad module test-beam measurements*, 2022, URL: https://cds.cern.ch/record/2813300.

[39] T. Heim, *First test results from the ITkPixV1 pixel readout chip*, Accessed: 2024-07-25, 2020, URL: https://indico.cern.ch/event/895924/contributions/3968862.

[40] RD53 Collaboration, *RD-53 Collaboration Home*, [Accessed: 2024-07-16], 2024, URL: https://rd53.web.cern.ch/.

[41] M. Standke, *Guide to the RD53A- Differential Front End*, Checked on: 23.07.2024, 2019, URL: https://twiki.cern.ch/twiki/pub/RD53/RD53ATesting/Diff_userguide.pdf.

[42] N. W. Ashcroft et al., *Solid State Physics*, American Journal of Physics **46** (1978) 116, ISSN: 0002-9505.

[43] H. Kolanoski and N. Wermes, *Particle Detectors: Fundamentals and Applications*, Oxford University Press, 2020, ISBN: 9780198858362, URL: https://doi.org/10.1093/oso/9780198858362.001.0001.

[44] P. Sigmund, *Particle Penetration and Radiation Effects: General Aspects and Stopping of Swift Point Charges*, Particle Penetration and Radiation Effects: General Aspects and Stopping of Swift Point Charges (2006).

[45] M. H. DeGroot and M. J. Schervish, *Probability and Statistics*, Addison-Wesley, 2012, ISBN: 9780321500465, URL: `https://books.google.de/books?id=4TlEPgAACAAJ`.

[46] L. D. Landau, *On the energy loss of fast particles by ionization*, 1965, URL: `https://www.sciencedirect.com/science/article/pii/B9780080105864500614`.

[47] G. Lindström, M. Moll, and E. Fretwurst, *Radiation hardness of silicon detectors – a challenge from high-energy physics*, Nuclear Instruments and Methods in Physics Research Section A: Accelerators, Spectrometers, Detectors and Associated Equipment **426** (1999) 1, ISSN: 0168-9002.

[48] G. Aad et al., *ATLAS pixel detector electronics and sensors*, Journal of Instrumentation **3** (2008) P07007.

[49] S. Chatrchyan et al., *Description and performance of the CMS pixel detector*, Journal of Instrumentation **3** (2008) P10007.

[50] D. Bortoletto, *How and why silicon sensors are becoming more and more intelligent?* Journal of Instrumentation **10** (2015) C08016.

[51] Y. Unno et al., *Development of novel n+-in-p Silicon Planar Pixel Sensors for HL-LHC*, Nuclear Instruments and Methods in Physics Research Section A: Accelerators, Spectrometers, Detectors and Associated Equipment **699** (2013) 72, ISSN: 0168-9002.

[52] T. Wittig, *Slim edge studies, design and quality control of planar ATLAS IBL pixel sensors*, 2013, URL: `https://cds.cern.ch/record/2305498`.

[53] M. Meschini et al., *Pixel Detector Developments for Tracker Upgrades of the High Luminosity LHC: Volume 2*, 2018, URL: `https://doi.org/10.1007/978-981-13-1316-5_65`.

[54] I. Perić et al., *The FEI3 readout chip for the ATLAS pixel detector*, Nucl. Instrum. Meth. A **565** (2006) 178, ed. by J. Grosse-Knetter, H. Krueger, and N. Wermes.

[55] M. Barbero et al., *The FE-I4 Pixel Readout Chip and the IBL Module*, 2011, URL: `https://cds.cern.ch/record/1405045`.

[56] M. Backhaus et al., *Development of a versatile and modular test system for ATLAS hybrid pixel detectors*, Nuclear Instruments and Methods in Physics Research Section A: Accelerators, Spectrometers, Detectors and Associated Equipment **650** (2011) 37.

[57] M. Daas et al., *BDAQ53, a versatile pixel detector readout and test system for the ATLAS and CMS HL-LHC upgrades*, Nuclear Instruments and Methods in Physics Research Section A: Accelerators, Spectrometers, Detectors and Associated Equipment **986** (2021) 164721, ISSN: 0168-9002.

[58] T. Heim, *YARR - A PCIe based Readout Concept for Current and Future ATLAS Pixel Modules*, Journal of Physics: Conference Series **898** (2017) 032053.

[59] J. Anderson et al., *FELIX: The new approach for interfacing to front-end electronics for the ATLAS experiment*, 2016, URL: `https://doi.org/10.1109/RTC.2016.7543142`.

[60] Hamamatsu Photonics K.K, *Hamamatsu Photonics Product Catalog*, Accessed: Feb. 13, 2025, 2024, URL: `https://www.hamamatsu.com`.

[61] Fondazione Bruno Kessler, *FBK Semiconductor Laboratory*, Accessed: Feb. 13, 2025, 2024, URL: `https://www.fbk.eu`.

[62] Micron Semiconductor Ltd., *Micron Semiconductor*, Accessed: Feb. 13, 2025, 2024, URL: `https://www.micronsemiconductor.co.uk`.

[63] S. Möbius and on behalf of the ATLAS ITk Group, *Module development for the ATLAS ITk pixel detector*, Journal of Instrumentation **17** (2022) C03042.

[64] Koji Nakamura, *ATLAS ITk Pixel Detector Overview*, (2023), `https://cds.cern.ch/record/2870235`.

[65] Y. Tian et al., *ATLAS ITk Pixel Pre-production Planar Sensor Characterisation for the HL-LHC Upgrade*, PoS **Pixel2022** (2023) 067.

[66] S. Hadzic, *Production and Performance of Silicon Pixel Modules with Planar Sensors for the ATLAS ITk Upgrade*, Dissertation, 2023, URL: `https://publications.mppmu.mpg.de/2023/MPP-2023-131/FullText.pdf`.

[67] Inc. Keithley Instruments, *Model 2410 1100V SourceMeter® Service Manual*, 2017, URL: `https://www.tek.com/en/manual/source-measure-units/keithley-smu-2400-series-sourcemeter-manual-3-2400-graphical-series-sourcemeter5`.

[68] S. Dungs et al., *E4control*, Accessed: 2024-10-22, 2020, URL: `https://github.com/sdungs/E4control`.

[69] Agilent Technologies, *Agilent 4284A Precision LCR Meter*, 2000, URL: `https://www.keysight.com/de/de/assets/9018-01389/user-manuals/9018-01389.pdf`.

[70] D. Banerjee et al., *The North Experimental Area at the Cern Super Proton Synchrotron*, 2021, URL: `https://cds.cern.ch/record/2774716`.

[71] J. Baudot et al., *First test results Of MIMOSA-26, a fast CMOS sensor with integrated zero suppression and digitized output*, IEEE Nuclear Science Symposium Conference Record (NSS/MIC) (2009) 1169.

[72] H. Jansen et al., *Performance of the EUDET-type beam telescopes*, EPJ Techniques and Instrumentation **3** (2016), ISSN: 2195-7045.

[73] P. Baesso, D. Cussans, and J. Goldstein, *The AIDA-2020 TLU: a flexible trigger logic unit for test beam facilities*, Journal of Instrumentation **14** (2019) P09019.

[74] D. Cussans, *A Trigger/Timing Logic Unit for ILC Test-beams*, 2008, URL: `https://cds.cern.ch/record/1091502`.

[75] P. Ahlburg et al., *EUDAQ-a data acquisition software framework for common beam telescopes*, JINST **15** (2020) P01038.

[76] S. Spannagel, *Test Beam Measurements for the Upgrade of the CMS Pixel Detector and Measurement of the Top Quark Mass from Differential Cross Sections*, DESY-THESIS (2016) 275, Dissertation, Universität Hamburg, 2016, ISSN: 1435-8085.

[77] S. Spannagel et al., *Allpix2: A modular simulation framework for silicon detectors*, Nuclear Instruments and Methods in Physics Research Section A: Accelerators, Spectrometers, Detectors and Associated Equipment **901** (2018) 164, ISSN: 0168-9002.

[78] S. Agostinelli et al., *Geant4—a simulation toolkit*, Nuclear Instruments and Methods in Physics Research Section A: Accelerators, Spectrometers, Detectors and Associated Equipment **506** (2003) 250, ISSN: 0168-9002.

[79] R. Brun and F. Rademakers, *ROOT — An object oriented data analysis framework*, Nuclear Instruments and Methods in Physics Research Section A: Accelerators, Spectrometers, Detectors and Associated Equipment **389** (1997) 81, ISSN: 0168-9002.

[80] D. Dannheim et al., *Corryvreckan: a modular 4D track reconstruction and analysis software for test beam data*, Journal of Instrumentation **16** (2021) P03008.

[81] C. Kleinwort, *General broken lines as advanced track fitting method*, Nuclear Instruments and Methods in Physics Research Section A: Accelerators, Spectrometers, Detectors and Associated Equipment **673** (2012) 107, ISSN: 0168-9002.

[82] A. M. Cormack, *Representation of a Function by Its Line Integrals, with Some Radiological Applications*, Journal of Applied Physics **34** (1963) 2722, ISSN: 0021-8979.

[83] K. M. Hanson, *Proton Computed Tomography*, IEEE Transactions on Nuclear Science **26** (1979) 1635.

[84] C. Krause, *Track reconstruction for low energy protons using Corryvreckan*, (2021), Master's Thesis.

[85] CERN, *H6 Beam Line Information*, Accessed: 18 Feb. 2025, 2017, URL: https://sba.web.cern.ch/sba/BeamsAndAreas/H6/H6_presentation.html.

[86] Tianqi Chen and Carlos Guestrin, *XGBoost: A Scalable Tree Boosting System*, KDD '16 (2016) 785.

[87] L. Breiman et al., *Classification And Regression Trees*, Chapman and Hall/CRC (1984) 1.

[88] Tin Kam Ho, *Random decision forests*, Proceedings of the 3rd International Conference on Document Analysis and Recognition (ICDAR) **1** (1995) 278.

[89] J. H. Friedman, *Greedy function approximation: A gradient boosting machine.*, The Annals of Statistics **29** (2001) 1189.

[90] F. Sigrist, *Gradient and Newton boosting for classification and regression*, Expert Systems with Applications **167** (2021) 114080, ISSN: 0957-4174.

[91] T. Hastie, *Ridge Regularization: An Essential Concept in Data Science*, Technometrics **62** (2020) 426.

[92] D. Freedman, R. Pisani, and R. Purves, *Statistics*, 2007, URL: https://wwnorton.com/books/Statistics.

[93] G. Van Rossum and F. L. Drake, *Python 3 Reference Manual*, Scotts Valley, CA: CreateSpace, 2009, ISBN: 1441412697, URL: https://dl.acm.org/doi/book/10.5555/1593511.

[94] F. Pedregosa et al., *Scikit-learn: Machine Learning in Python*, Journal of Machine Learning Research **12** (2011) 2825, ISSN: 1532-4435.

[95] M. A. A. Samy et al., *Recent test beam results of ATLAS ITk pixel 2 modules*, tech. rep., CERN, 2025, URL: https://cds.cern.ch/record/2923303.

[96] High Energy Accelerator Research Organization (KEK), https://www.kek.jp/en, Accessed: 01.2025.

[97] Advafab: Semiconductor solutions, https://advafab.com, Accessed: 01.2025.

[98] Fraunhofer IZM, Accessed: Apr. 10, 2025, 2024, URL: https://www.izm.fraunhofer.de/en.html.

[99] SINTEF, Accessed: Feb. 24, 2025, 2024, URL: https://www.sintef.no/en.

[100] D. Antrim et al., *Recent RD53B Test Results*, 2020, URL: https://indico.physics.lbl.gov/event/1378/contributions/5240/attachments/2527/3323/2020_11_20_lbl_instrumentation_weekly_RD53bStatusPDF.pdf.

[101] S. Hellesund et al., *Test Beam Results of SINTEF 3D Pixel Silicon Sensors*, PoS **VERTEX2023** (2024) 076.

[102] J. L. Wiza, *Microchannel plate detectors*, Nuclear Instruments and Methods **162** (1979) 587, ISSN: 0029-554X.

[103] G. Pellegrini et al., *Technology developments and first measurements of Low Gain Avalanche Detectors (LGAD) for high energy physics applications*, Nuclear Instruments and Methods in Physics Research Section A: Accelerators, Spectrometers, Detectors and Associated Equipment **765** (2014) 12, ISSN: 0168-9002.

Danksagung

Zunächst möchte ich Andrea Teichmann für die unermüdliche Unterstützung danken, insbesondere dafür, jegliche noch so ärgerliche Bürokratie für mich bewältigt zu haben. Ein besonderer Dank gebührt Herrn Prof. Dr. Kröninger und Dr. Dominik Mitzel für die Begutachtung meiner Arbeit. Das Arbeitsumfeld der AG Kröninger hat mich von der Bachelorarbeit bis zur Promotion stets bereichert, und ich habe unglaublich gern in dieser Arbeitsgruppe gearbeitet. Danke, Jens, für die Betreuung, dafür, immer ein offenes Ohr für meine Probleme gehabt zu haben, sowie für deine guten Ideen, die stets den Weg nach vorn geebnet haben. In diesem Zusammenhang danke ich auch Tobias, ohne dessen Expertise der CERN-Testbeam und die In-Time-Effizienzanalyse niemals so erfolgreich verlaufen wären.

Zusätzlich bedanke ich mich bei der ATLAS ITk Pixel Collaboration für die Möglichkeit, über viele Jahre hinweg an zahlreichen Testbeams teilzunehmen. Nur durch die gesamte Gruppe war das Messen zahlreicher Pixelmodule überhaupt erst möglich. Auch wenn sich einige Kampagnen als nicht erfolgreich erwiesen, wurde stets daraus gelernt, um es beim nächsten Mal besser zu machen. Marta und Carsten danke ich für das eifrige Korrekturlesen so vieler Seiten meiner Arbeit.

Ich danke Valerie für die Einarbeitung in die Laborarbeit, die mir als angehendem PhD-Studenten noch weitgehend fremd war. Ganz besonders möchte ich Mikes Engagement hervorheben. Er hat mir bei unzähligen Labor- und IT-Problemen geholfen und das ohne Wenn und Aber. Vielen Dank dafür! Bei Björn, Kevin und Matthias möchte ich mich für die Einführung in die IT-Arbeit bedanken, ebenso bei Nils, Lucas und Janna, die die Arbeit mit mir teilten und mich ungemein unterstützt haben. So manche IT-Krise schien ohne eure Hilfe nahezu ausweglos.

Natürlich geht mein Dank auch an alle anderen Kolleginnen und Kollegen in der Arbeitsgruppe, von denen viele zu guten Freunden wurden. Die Spiele und der Sport mit euch haben mir Kraft gegeben, sodass ich mich jeden Tag aufs Neue gefreut habe, in die Uni zu gehen. Insbesondere möchte ich Hendrik, Michael, Lucas, Salvatore, Alina, Jennifer, Marco, Janina, Benedikt, Donna, Cornelius, Chris und Tobias diesbezüglich danken.

Zuletzt möchte ich mich bei meiner Familie, meinen Freunden und Jan Lukas zutiefst bedanken, dass sie immer für mich da sind. Ihr gebt mir den Halt, meiner Zukunft mit Mut und Zuversicht entgegenzutreten.